

UNIVERSITY OF
BIRMINGHAM

Non-equilibrium quantum thermodynamics in ultracold atomic mixtures

by

Jorge Mellado Muñoz

A thesis submitted to

The University of Birmingham

for the degree of

Doctor of Philosophy

School of Physics and Astronomy

College of Engineering and Physical Sciences

The University of Birmingham

December 2020

UNIVERSITY OF
BIRMINGHAM

University of Birmingham Research Archive

e-theses repository

This unpublished thesis/dissertation is copyright of the author and/or third parties. The intellectual property rights of the author or third parties in respect of this work are as defined by The Copyright Designs and Patents Act 1988 or as modified by any successor legislation.

Any use made of information contained in this thesis/dissertation must be in accordance with that legislation and must be properly acknowledged. Further distribution or reproduction in any format is prohibited without the permission of the copyright holder.

Abstract

This thesis is devoted to the experimental study of non-equilibrium quantum thermodynamics. In it, I describe the design and development of a system that allowed our team to perform pioneering experiment on non-equilibrium quantum gases close to the absolute zero. Using such a system, we achieved the realization of long-lived non-equilibrium Bose-Einstein condensates with condensed fractions exceeding those of equilibrium samples with the same parameters. We achieved this by immersing an ultracold Bose gas of ^{87}Rb in a cloud of ^{39}K with a temperature difference of four orders of magnitude, providing a controlled source of dissipation. Then, I report the state of the current project: the implementation of a single-atom quantum engine using a single ^{41}K atom as the working fluid and an ultracold cloud of ^{87}Rb as the thermal bath. Lastly, I show that it is possible to realize the Frenkel-Kontorova model using a system of interacting Rydberg-dressed atoms placed in an optical lattice. To do so, I studied the properties of the ground states of the system and its phonon spectra for different sets of parameters by simulating the cited system.

A Adolfo, don Luis y mis padres.

Acknowledgements

As a curtain-raiser to this thesis, I would like to thank all the people who have helped me along the way. The order here does not follow any logic. For starters, I would like to thank Giovanni as he has been my supervisor all these years regardless of the countless headaches I caused him. Thanks to you, I went from my initial state in which I barely knew the basics of cold atoms to a point in which I managed to build and maintain a huge experiment. You also contributed to my transition from experiment builder to scientist, and you have been always very supportive. I wish you all the best.

Now, I will proceed with the second in command, also known as Ania. I'd like to thank you for your constant support in and out of the lab. I apologize for all the suffering caused by either me or my labmate. I wish you the best of luck with your scientific projects and making life decisions.

Indeed, my labmate Eric, I haven't met any other person able to wake up in me such contradictory feelings. Now that I am leaving, I don't know if I should feel sad or relieved. Well, I am just joking, I will miss you for sure. Without your effort, this would not have been possible. I'd like to thank Jixun as well, as you were the one showing me the basics of the experiment.

Continuing with the lab, I would like to thank Tom for his initial contribution to my first publication and for being so eager to learn the basics of the experiment. Now, you have inherited the experiment I put part of my soul in, sometimes it will be frustrating, but I promise that the effort is very rewarding. And don't doubt of yourself, I can not think of anyone better to take

over this experiment, you will learn to tame the *Beast*. Don't forget that in few hours the Sun will rise. Special thanks to Rahul, as his hard work and dedication managed to push our research in and out of the lab. You set a very good example of how to be a postdoc, and you proved to be resourceful when we had problems. I hope you manage to get the single atom soon.

Moving to the other team, thanks to Aaron, it was fun to live with you, and you help me to keep my mind in place during the long quarantine. Keep working hard with the help of your Tom, and I am sure you will get the results you deserve. I wish you every success.

Luckily, I also have friends outside of the lab in this city. To David, I wish you all the best in your new career. It was great to hang out with you. To my friends from CERU, thank you for all the fun. In particular, thanks to Claudia and Simon, you are some of the kindest people I know. I wish you all the best. I have to thank Юля as well, as I found a friend in you in these strange times. Thank you for helping me in my way to master the art of bicycle maintenance.

To Daniel, thank you, you have been helping me even before I arrived in Birmingham. I learned a lot from you in the lab. After that, you have always been there when I needed help or I have doubts about what to do with my life. I wish you, Thaïs and Abril all the best.

I want to thank my friend Jaime who also enjoyed the pleasures of the lab and together with the other Jaime and Tomás helped me to go through the PhD. I wish you enjoy your PhDs. To *el Juanan* and *el Bene*, thank you for helping with my mood every time I needed it. I really miss you guys. You really managed to remind me of where I come from and why I should never give up. Thank you for everything. I should thank Noemi for the same reason, as you have been very supportive during these years. Someone else I met in my city is Emma. I met you even before we started to study physics, you have

always believed in me, and you have always been comprehensive and caring with me regardless of the circumstances. That is something I will never forget, and trust me: I expect you to become a great scientist, so don't give up, keep pushing!

Now, moving into my mentors. First, I met *Don Luis*, you taught me together with sport how one has to fight for his dreams, how we should never give up but most important you made me realize that the motivation behind is not to win over others but to enjoy and improve, thank you for everything. Later, I met Adolfo. I have to tell you that I don't know if I admire more the scientist you are or your person with your incredible sense of justice. I think I can not separate the man from the scientist. I have to thank you for everything, all your help and guidance in the good and bad moments.

Finally, I have to thank my parents, as they have been my main support. I have to thank you for the way you educated me, for the dedication and time you put in me, and for still being completely willing to help me in case of need. I know I have chosen a path that will keep me away from home but trust me, I miss you every day with all my heart, and the same goes for my sister Ana as well. I want to thank as well the rest of my family and all their support.

Table of Contents

1 Introduction **1**

1.1 Thesis outline 4

2 Background theory **7**

2.1 Non-equilibrium BEC 8

2.1.1 Equilibrium ideal BEC transition 8

2.1.1.1 Corrections to the equilibrium BEC transition 12

2.1.2 Cooling techniques 14

2.1.2.1 Laser cooling 15

2.1.2.2 Evaporative cooling 16

2.1.3 Ultracold and cold atoms collisions 18

2.1.4 Condensate growth 20

2.2 Single atom quantum engine 22

2.2.1 From classical to quantum thermodynamics 22

2.2.2 Thermodynamic transformations in the quantum level 23

2.2.3 Feshbach resonances and tunable interactions 27

2.2.4 Quantum engines 29

2.2.4.1 Quantum Carnot engine 30

2.2.4.2 Quantum Otto engine 32

2.2.4.3 Quantum Diesel engine 34

2.3 The Frenkel-Kontorova model 36

3 Experimental setup **38**

3.1 Vacuum system 39

3.2 Laser system 42

3.2.1 Laser cooling system 43

3.2.1.1 Laser cooling layout 45

3.2.2 Dipole trap system 49

3.3 Optical tweezer 51

3.4 Imaging system 53

3.4.1 Imaging techniques 54

3.4.2 Acquisition software 57

3.5 Control system 58

4 NEQT in a ^{87}Rb-^{39}K mixture **61**

4.1 Realizing an all-optical ^{87}Rb BEC in our setup 62

4.1.1 Experimental sequence 62

4.1.2 Loading Rb atoms into the 3D MOT 64

4.1.3 Rb dark MOT 65

4.1.4 Evaporative cooling 65

4.1.5 ^{87}Rb BEC characterization 66

4.2 Cooling and trapping of K 70

4.2.1 K MOT and dark MOT 71

4.2.2 K Sub-Doppler cooling with D_2 molasses 71

4.2.3 Loading K atoms in the dipole trap 72

4.3 Study of NEQT in a dissipative environment 74

4.3.1 Supercritical BEC 75

4.3.2 Relaxation towards equilibrium state 77

4.3.3 Modeling the system 79

4.4 Inducing dissipation in the Rb BEC 85

4.4.1 Measuring the interspecies scattering rate 85

4.4.2 Why non-equilibrium quantum thermodynamics? 88

5 Single atom quantum engine **90**

5.1 Components of the single-atom quantum engine 90

5.2 Developing a species-selective optical tweezer 91

5.2.1 Heating rate 92

5.2.2 Collisional blockade 93

5.2.3 Tweezer loading 94

5.2.4 Fluorescence imaging of a single atom 94

5.3 Future steps 96

6 FKM with Rydberg-dressed atoms **98**

6.1 The system 99

6.2 Rydberg-dressed states 103

6.3 The phase diagrams 105

6.3.1 The springlike case 107

6.3.2 The repulsive case 109

6.4 Incommensurate configurations 110

6.4.1 Incommensurate ground states 111

6.4.2 Phonon spectrum 112

6.5 Experimental implementation 116

7 Conclusions and Further Remarks **118**

Appendices **135**

Appendix A Calibration of the trapping frequencies **136**

Appendix B Chemical potential calculation **138**

Appendix C Rydberg-dressed atoms **139**

List of Figures

2.1 BEC transition. 12

2.2 Depiction of the quantum adiabatic transformation. 24

2.3 Depiction of the quantum isothermal transformation. 25

2.4 Depiction of the quantum isochoric transformation. 25

2.5 Depiction of the quantum isobaric transformation. 27

2.6 The the two channel model used to describe the physics behind the Feshbach resonances. 27

2.7 Scatering length of the interaction between $^{87}\mathrm{Rb}|1,1\rangle$ and $^{41}\mathrm{K}|1,1\rangle$. 28

2.8 Depiction of the Quantum Carnot engine. 30

2.9 Evolution of the trapping frequencies of the bath and the tweezer for the Quantum Carnot engine. 31

2.10 Ratio of real efficiencies and the maximum theoretical efficiency as a function of different parameters. 32

2.11 Depiction of the Quantum Otto engine. 33

2.12 Evolution of the trapping frequencies of the bath and the tweezer for the Quantum Otto engine. 34

2.13 Depiction of the Quantum Diesel engine. 34

2.14 Evolution of the trapping frequencies of the bath and the tweezer for the Quantum Diesel engine. 35

2.15 Depiction of the Frenkel-Kontorova model. 36

3.1 Schematics of the vacuum system. 41

3.2 Top view of the experimental setup. 41

3.3 Detail of the vacuum setup when initially placed. 42

3.4 Structure of the atomic levels of the D_2 line of ^{87}Rb. 44

3.5 D_2 line for ^{39}K and ^{41}K. 45

3.6 Schematics of the fiber splitters. 47

3.7 Schematics of the laser layout used for K and Rb laser cooling. 48

3.8 Schematics of the optic layout for both 1070 nm and 1550 nm dipole traps. 50

3.9 Schematics of the optic layout for the optical tweezer. 52

3.10 Schematics of the imaging system. 54

3.11 Screen-shot of *cam strip down*. 57

3.12 Screenshot of Cicero. 59

3.13 Schematics of the control system for our experiment. 60

4.1 Experimental sequence used to obtain a ^{87}Rb BEC. 63

4.2 Parametric heating of the ^{87}Rb BEC. 68

4.3 Optical density profiles obtained by absorption imaging for the ^{87}Rb cloud. 68

4.4 Optical density across the horizontal axis. 69

4.5 K temperature determination. 72

4.6 Absorption imaging picture of Rb and K atoms when loaded in the dipole trap. 73

4.7 Experimental sequence used to obtain a supercritical BEC by dissipation. . 76

4.8 Phase diagram for the condensed fraction versus the reduced temperature. 77

4.9 Different parameters for the experiment depicted in figure 4.7 versus evaporation time for a BEC. 78

4.10 Same as figure 4.9 but for a dissipation four times stronger. 78

4.11 Experimental sequence used to study the relaxation of the supercritical BEC back to equilibrium. 79

4.12 Difference between the measured F and that expected. 80

4.13 Different parameters for the experiment depicted in figure 4.11 versus evaporation time for a BEC with and without dissipation. 80

4.14 Depiction of model used and described by equations 4.6 and 4.7. 83

4.15 Evolution as a function of time of the number of atoms in the thermal component, the number of atoms in the BEC and the condensate fraction F. 84

4.16 Experimental sequence used to measure the scattering rate between the two species. 87

4.17 Rb atom number as a function of time with and without K atoms. 87

4.18 Theoretical prediction and experimental values for the γ_K. 88

5.1 Dipole potential for both Rb and K. 92

5.2 Signal from the atoms trap in the tweezer versus the detuning of the cooling in the fluorescence imaging stage. 95

5.3 Signal from the atoms trap in the tweezer versus the detuning of the repumper in the fluorescence imaging stage. 96

6.1 Depiction of the schematics of the model. 100

6.2 Normalized interatomic potentials obtained by dressing the atoms with Rydberg states. 102

6.3 The energy of the dressed states versus the interatomic distance. 104

6.4 Phase diagram showing $\tilde{a}/b$ as a function of a/b and V_0/c_1. 105

6.5 Different parameters versus a/b for the repulsive and springlike cases. . . . 108

6.6 Particle position with respect to the lattice potential for each value of V_0/c_1 for the springlike and the repulsive case. 112

6.7 Phonon spectrum for the springlike and repulsive cases. 115

A.1 Calibration of the trapping frequencies. 137

List of Tables

3.1 Parameters of the lasers used during the loading of the MOT. 49

4.1 Dipole traps power at the beginning of each stage of the evaporative cooling. 64

List of Abbreviations

AOM	Acousto-optic modulator.
BEC	Bose-Einstein Condensate.
ECDL	External-cavity diode lasers.
EOM	Electro-optic modulator.
FKM	Frenkel-Kontorova model.
Laser	Light amplification by stimulated emission of radiation.
MOT	Magneto-optical trap.
NEQT	Non-equilibrium quantum thermodynamics.
PBS	Polarization beam splitter.
PID	Proportional–integral–derivative controller.
TA	Tapered amplifier.

Chapter 1

Introduction

Back in the 19th century, the industrial revolution brought technological advancements that completely transformed the means of production. The most important of those technological advancements was the steam engine. The epochal changes and the huge transformative potential of these advancements, attracted also the curiosity of some scientists like Carnot, Calpeyron and Clausius. They tried to understand the limits of how efficient an engine could be and how it could be described theoretically, laying the foundation of the field known as thermodynamics.

Only a few decades later, a scientific revolution followed the industrial one, as relativity and quantum physics challenged the then known physics as well as our concept of time. The revolution that followed led to the creation of another field, closely related to thermodynamics, known as statistical physics, due to the growing interest in microscopic systems studied by quantum physics. This field provided a bridge between the microscopic behavior of the particles and the macroscopic description of thermodynamics. It was in those early years of the 20th century that Bose and Einstein also proposed theoretically the existence of the Bose-Einstein condensate (BEC). The BEC is a state of matter in which a system of bosons is placed in its lowest quantum level, resulting in the

manifestation of quantum effects, such as wave-particle interference, macroscopically.

In the following 70 years, the advances in laser technologies, together with the novel ideas and understanding of atomic physics continued to grow, culminating in the realization of the first experimental BEC in 1995 [1]. For this achievement and the related early work, Eric Allin Cornell, Wolfgang Ketterle and Carl Wieman received the Nobel Prize in 2001. At the turn of the century, the level of manipulation of cold atoms systems reached the single atom level [2]. Along these advancements, other fields such as computation hardware, biology, nanoscale physics, etc... have moved progressively to the study of systems that have reached the quantum level. Consequently, there is a growing interest in understanding thermodynamics as such small scales, in which the concept of temperature needs to be re-defined, as well as those of work and heat. This interest has resulted in the creation of a new field known as quantum thermodynamics.

As with classic thermodynamics, engines are fundamental for the understanding of quantum thermodynamics. The engines in this context are known as quantum engines. These have been the object of different studies [3, 4, 5, 6]. There is a growing interest in their understanding not only from a purely theoretical point of view but from an experimental too because engines using a quantum-coherent working fluid can theoretically obtain higher powers than their classical counterparts [7]. Furthermore, for non-thermal baths which are dominated by the many-body quantum effects instead of thermal fluctuations, one can achieve more efficient regimes [8, 9, 10, 11, 12]. A remarkable example of this is a heat engine operating an Otto cycle with a many-particle working medium that outperformed a single particle classical heat engine [13].

The experimental realization of the previously explained theoretical advances is nowadays a hot topic. Some recent examples are the use of nitrogen-vacancy(NV) centers in diamond and ultra-cold atoms to demonstrate features related to heat engines [14, 15]. It is here, where the original purpose of this thesis, the experimental realization of single-atom quantum engines finds its niche. In fact, the only experimental implementation of a

single-atom engine is reported in reference [16] in which a single atom is trapped in a Paul trap. However, this atom is not cold enough for the quantum effects to become relevant, making this engine single-atom but not quantum. In our case, the platform we chose is ultracold atomic mixtures, as this system allows for the degree of control required for the realization of arbitrary thermodynamic transformations. Consequently, we will be able to realize the different thermodynamics cycles at the quantum level [3, 4, 5] since the typical range of operation of this system falls in the quantum regime.

The advantage of using ultracold atomic mixtures is that the system is so flexible that it allowed us to study one of the most paradigmatic concepts in thermodynamics, which is dissipation. Dissipation is normally regarded as a detrimental mechanism. This applies not only to classic systems but to quantum systems as well. One of the most remarkable examples that we find in our day-to-day life is the friction that sometimes limits the performance of classical engines. In the quantum world, we can find the decoherence that destroys purely quantum effects as an example of dissipation. Despite these detrimental effects, dissipative processes can be engineered in a way that allows for the study of new physics. Some examples in which this has been achieved are the use of dissipation to generate new states of matter [17, 18, 19, 20], the manipulation of qubits [21], the distillation of quantum features [22] and the realization of decoherence-free subspaces [23, 24, 25] as well as entangled quantum states [26].

Concerning non-equilibrium quantum thermodynamics, dissipation can be used to drive a system out of equilibrium when applied to it with enough power so that the system can not restore its equilibrium in the considered timescale. This allows for the study of new regions of the parameter space [27, 28]. Some of the most relevant work related to the understanding of non-equilibrium many-body systems, including how they can be realized and the study of their evolution can be found in references [29, 30]. Closer to our experiment, we found that ultracold atoms have proven to be an ideal platform to study the dynamics of a wide range of non-equilibrium systems. This includes low dimensional

Bose gases [31, 32, 33], quenched quantum gases [34, 27, 35] and prethermalized states [36, 30]. In contrast with our experiment, but of interest for the study of non-equilibrium quantum thermodynamics, we find system such as photon BEC [37] and exciton-polariton condensates [38] in which the systems are inherently out of equilibrium instead of being driven out of equilibrium.

Lastly, I would like to mention the Frenkel-Kontorova model, for which I propose its experimental realization with ultracold atoms in this thesis. This model can be used to study a multitude of physical systems involving two length-scales [39]. In particular, it can be used to understand the effects of friction [40]. Where friction can be related to dissipation, as it is a type of dissipative process in which energy is lost irreversibly.

1.1 Thesis outline

At the start of my PhD, I inherited the experimental setup from the previous research group, described in [41]. I worked with the cited experiment for seven months in which I learned the basics of ultracold gases experiments. During that period, the machine proved to be unreliable, slow and built on somehow surpassed concepts, we thus decided to build a completely new one.

In the following months, I worked on the design and development of the new setup. Starting from an empty optical table, it took us one year to achieve the trapping of ^{87}Rb atoms in a magneto-optical trap (MOT). Just a few weeks later, we also produced an all-optical ^{87}Rb BEC by performing evaporative cooling in a dipole trap. After this, we started to develop the laser system to cool down the ^{41}K atoms. It took us a half year to trap the ^{41}K atoms in the MOT, achieving a setup capable of working with two different atomic species. We then attempted to produce a two species all-optical ^{41}K-^{87}Rb BEC, and then we modified our system to try to achieve this with ^{39}K instead of ^{41}K.

From this point, we took the first step towards the study of non-equilibrium quantum thermodynamics (NEQT) as we started to study the growth of a BEC in a high-temperature environment. This system was embodied by an ^{87}Rb BEC immersed in a cloud of ^{39}K trapped in a MOT. The temperature of the ^{39}K MOT was four orders of magnitude higher than that of the ^{87}Rb BEC. This induced the dissipation of the later allowing us for the production of out of equilibrium supercritical BEC samples. We named this process as dissipative distillation [42].

The next objective we are currently working on is the development of the optical tweezer for the experimental realization of a single-atom quantum engine. However, due to Covid-19, we were forced to close the experiment for half a year. While I was in lockdown, I decided to complete a theoretical work we started while I was working as a summer student in this group. In this work, I propose the experimental realization of the Frenkel-Kontorova model (FKM) with Rydberg-dressed atoms. This work culminated in the publication found in reference [43]. At the end of the lockdown, we were able to go back into the lab and we are now very close to trap single atoms of ^{41}K.

All of this is explained in the chapters of this thesis. The structure of the chapters is the following:

- **Chapter 2 Background theory:** in this chapter, I explain the different theory elements required to understand the model behind our supercritical BEC. It contains a very brief explanation of the connection between our planned single-atom quantum engine and the usual thermodynamic variables. Lastly, the reader can find an introduction to the Frenkel-Kontorova model.
- **Chapter 3 Experimental setup:** this chapter contains a summarised explanation of the experimental setup that I have built, including a summary of the vacuum, laser, control, and imaging systems we built.
- **Chapter 4 NEQT in a ^{87}Rb-^{39}K mixture:** the main part of this chapter is

devoted to our work to study and characterize non-equilibrium supercritical BECs. It also includes how we obtained the ^{87}Rb BEC and how we attempted the two species BEC.

- **Chapter 5 Single atom quantum engine:** a description of how our optical tweezer works and its current development can be found in this chapter. Together with this, this chapter contains a description of the planned quantum engine implementations.

- **Chapter 6 FKM with Rydberg-dressed atoms:** this last chapter is devoted to the simulations of the FKM using Rydberg-dressed atoms.

Chapter 2

Background theory

In this chapter, I introduce the theory required to understand the rest of this thesis, including the review of previous work related to the topics. The structure of this chapter is as follows:

- **Section 2.1** contains the theory needed to understand the model and the processes concerning the BEC transition in a dissipative environment, including the cooling techniques used to reach such state. The outcome of this is covered in chapter 4. I included as well a description of the equilibrium BEC transition together with the corrections for interactions and finite-size effects. After this, I present the theory addressing the BEC growth in the absence of dissipation and the model that describes the collisions between ultracold and cold atoms responsible for the dissipative phenomena.

- In **section 2.2**, the reader can find the theory related to the single-atom quantum engine. I cover the current state of development in chapter 5. This section explains the parallelism between the quantum and classical variables, the possible implementations of quantum thermodynamic transformations and engines, and a brief description of the tunable interactions used.

- Finally, **section 2.3** provides an introduction to the Frenkel-Kontorova model, helping the understanding of chapter 6, where I present the theoretical proposal for the realization of the Frenkel-Kontorova model with Rydberg-dressed atoms.

2.1 Non-equilibrium BEC

2.1.1 Equilibrium ideal BEC transition

A BEC is a state of matter in which all the particles of a system composed of Bosons are in their lowest quantum state. For a system of ideal Bosons, i.e. non interacting, the Bose distribution, f^0, provides us with the mean occupation number of the different states, ν,

$$f^0(\epsilon_\nu) = \frac{1}{e^{(\epsilon_\nu - \mu)/(k_B T)} - 1}, \tag{2.1}$$

where ϵ_ν is the energy of the given ν state, μ is the chemical potential, k_B is the Boltzmann constant and T is the temperature of the sample. The mathematical definition of the chemical potential, μ, is given by the following expression,

$$\mu = \left(\frac{dU}{dN}\right)_{S,V}, \tag{2.2}$$

where U is the internal energy of the system, N the particle number, S the entropy and V the volume. From equation 2.2 one can interpret the chemical potential as the energy required to place a particle in a given state. To calculate the total number of states, $G(\epsilon)$, we consider that the volume in the phase space per quantum state is h^3, with h being the Planck's constant. In the phase space we have that a sphere of volume $4\pi p^3/3$ will contain all the states with momentum less than p and we can consider the

kinetic energy as $\epsilon = p^2/2m$, with m the mass of the particles. Thus, we obtain the following result,

$$G(\epsilon) = V\frac{4\pi p^3}{3}\frac{1}{h^3} = V\frac{\sqrt{2}}{3\pi^2}\frac{(m\epsilon)^{3/2}}{\hbar^3}. \tag{2.3}$$

The density of states as a function of the energy, $g(\epsilon)$, can be calculated as follows,

$$g(\epsilon) = \frac{dG(\epsilon)}{d\epsilon} = \frac{Vm^{3/2}}{2^{1/2}\pi^2\hbar^3}\epsilon^{1/2}. \tag{2.4}$$

Given that our particles are confined in a harmonic trap, we calculate $G(\epsilon)$ for this particular case. If we consider that the particles are trapped in a 3D harmonic potential, U, given by the following expression,

$$U(\mathbf{r}) = \frac{1}{2}m\left(\omega_1^2x^2 + \omega_2^2y^2 + \omega_3^2z^2\right), \tag{2.5}$$

where ω_1, ω_2 and ω_3 are the trapping frequencies, the energy of a particle is,

$$\epsilon(n_1, n_2, n_3) = \underbrace{\left(n_1 + \frac{1}{2}\right)\hbar\omega_1}_{\epsilon_1} + \underbrace{\left(n_2 + \frac{1}{2}\right)\hbar\omega_2}_{\epsilon_2} + \underbrace{\left(n_3 + \frac{1}{2}\right)\hbar\omega_3}_{\epsilon_3}, \tag{2.6}$$

where n_1, n_2, n_3 are integers indicating the energy level of the particle. If we ignore the energy at $n_1, n_2, n_3 = 0$ and consider the energies as continuous variables, because of the small energy difference between the levels, the total number of states for a given $\epsilon = \epsilon_1 + \epsilon_2 + \epsilon_3$ is

$$G(\epsilon) = \frac{1}{\hbar^3\omega_1\omega_2\omega_3}\int_0^{\epsilon_1} d\epsilon_1 \int_0^{\epsilon-\epsilon_1} d\epsilon_2 \int_0^{\epsilon-\epsilon_1-\epsilon_2} d\epsilon_3 = \frac{\epsilon^3}{6\hbar^3\omega_1\omega_2\omega_3}, \tag{2.7}$$

from where it follows that

$$g(\epsilon) = \frac{dG(\epsilon)}{d\epsilon} = \frac{\epsilon^2}{2\hbar^3\omega_1\omega_2\omega_3} = \frac{\epsilon^2}{2\hbar^3\bar{\omega}^3}, \tag{2.8}$$

where $\bar{\omega} = (\omega_1\omega_2\omega_3)^{1/3}$ is the geometric average of the trapping frequencies. In the case of excited states the number of particles, N_{ex}, is given by,

$$N_{ex} = \int_0^\infty d\epsilon g(\epsilon) f_0(\epsilon). \tag{2.9}$$

When a BEC component is present there is a macroscopic amount of particles in the ground state. Thus, to define a critical temperature, T_c, in a system with N particles we should consider the case with no particles in the BEC component or equivalently, N particles in the excited states. At the critical temperature, the energy cost for a particle to be in any phase should be the same, the chemical potential is essentially the cost of adding a particle to a given component, so $\mu = 0$. Thus, we can obtain T_c from the following equation,

$$N = N_{ex}(T_c, \mu = 0) = \int_0^\infty d\epsilon g(\epsilon) \frac{1}{e^{\epsilon/k_B T_c} - 1}. \tag{2.10}$$

This leads to the following result,

$$T_c = \frac{\hbar\bar{\omega}N^{1/3}}{[\zeta(3)]^{1/3}k_B} \approx 0.94\frac{\hbar\bar{\omega}}{k_B}N^{1/3}, \tag{2.11}$$

with ζ the Riemann zeta function. Solving equation 2.10 for a temperature, T, below T_c and using equation 2.11 we obtain the relation,

$$N_{ex} = N\left(\frac{T}{T_c}\right)^3. \tag{2.12}$$

Considering that $N = N_0 + N_{ex}$ where N_0 is the number of particles in the ground state we can obtain the following relation,

$$F = \frac{N_0}{N} = 1 - \tau^3. \tag{2.13}$$

Where $F = \frac{N_0}{N}$ is usually referred to as the condensed fraction and $\tau = T/T_c$ is known as the reduced temperature. Since the previous relation only holds for $T < T_c$ and taking into account that $N_0/N = 0$ for $T > T_c$, it is usually written as,

$$F = \max\left(1 - \tau^3, 0\right). \tag{2.14}$$

This expression, depicted in figure 2.1, tells us the relation among the total number of atoms, those in the BEC phase, the temperature, and the trapping frequencies. This expression can be corrected to be used in our particular case. It is also useful to introduce the phase-space density (PSD). It is defined as the number of particles contained in a cube with a volume λ_T^3, with $\lambda_T = \sqrt{2\pi\hbar^2/mk_BT}$ the thermal de Broglie length. Thus, the PSD is calculated as follows,

$$\text{PSD} = n\lambda_T^3 \propto \frac{n}{T^{3/2}}, \tag{2.15}$$

with $n = N/V$ the atomic density. Using equations 2.4 and 2.10 it can be shown that the BEC transition occurs when PSD ≈ 2.612 [44]. Therefore, the PSD can be used as the figure of interest for the BEC transition.

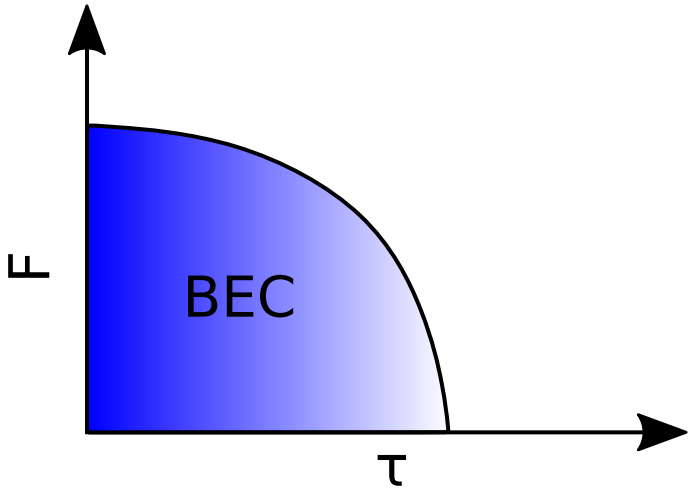


Figure 2.1: Condensed fraction versus reduced temperature for the BEC transition. The blue region represents the BEC phase.

2.1.1.1 Corrections to the equilibrium BEC transition

Equation 2.14 is only valid for a non-interacting and infinite gas of Bosons in equilibrium. However, the Bosons in our system are ^{87}Rb atom. This makes our bosonic gas not ideal due to the interatomic interactions and the finite size of the system. Thus, it has to be corrected to take into account these effects. In the following, I present the required corrections. The reader can complement this with a more extensive discussion of these corrections in reference [45]. Reference [46] supports this corrections with extensive experimental evidence and our data of the equilibrium BEC transition agrees as well with these correction [42]. The shift in the critical temperature, δT_c, due to finite size effects is given by [45]:

$$\frac{\delta T_c}{T_c} = -\frac{\omega}{\bar{\omega}} \frac{\zeta(2)}{\zeta(3)^{2/3}} N^{1/3}, \tag{2.16}$$

where ω is the arithmetic mean of the trapping frequencies. The shift due to interaction effects is given by [45, 47, 48]:

$$\frac{\delta T_c}{T_c} = -1.3\frac{a}{a_{\rm ho}}N^{1/6}, \tag{2.17}$$

where a is the s-wave scattering length and $a_{\rm ho}$ is the harmonic oscillator length defined as $a_{\rm ho} = \sqrt{\hbar/m\bar{\omega}}$. However, we also have to consider the effect of the interactions not only in T_c but in the condensed fraction as a function of the temperature as well. Equation 2.18, which is extracted from reference [45], can be used to calculate the total number of atoms in the excited levels or thermal atoms,

$$N_T = \int \frac{d\mathbf{r}d\mathbf{p}}{(2\pi\hbar)^3}\left\{\exp\left[\frac{\left(\frac{p^2}{2m} + V_{\rm eff} - \mu\right)}{k_B T} - 1\right]\right\}^{-1}. \tag{2.18}$$

where $V_{\rm eff}$ is the effective potential experienced by the atoms. To calculate the last integral, we use the Thomas-Fermi approximation [44] for the effective mean-field potential, given by the following expression,

$$V_{\rm eff} - \mu = |V_{\rm ext} - \mu|, \tag{2.19}$$

where $V_{\rm ext}$ is the external potential, described by the trapping potential. This approximation holds as long as $a_{\rm ho}/a << N_0$. The chemical potential when the interaction becomes relevant for large N, is given by [45],

$$\mu = \frac{\hbar\bar{\omega}}{2}\left(\frac{15Na}{a_{\rm ho}}\right)^{2/5}. \tag{2.20}$$

Using these approximations, the integral 2.18 for $T < T_c$ yields,

$$\frac{N_0}{N} = 1 - \tau^3 - \eta\tau^2 \left(1 - \tau^3\right)^{2/5}, \tag{2.21}$$

where $\tau = T/T_c$ and $\eta = 2.15(aN^{1/6}/a_{\mathrm{ho}})^{2/5}$. Thus, in the equilibrium situation the BEC phase transition is given by the following expression,

$$F = \frac{N_0}{N} = \begin{cases} 1 - \tau^3 - \eta\tau^2(1-\tau^3)^{2/5} & \text{for } T < T_c \\ 0 & \text{for } T > T_c \end{cases} \tag{2.22}$$

Here the meaning of equilibrium is that within the thermal noise the condensed fraction will follow the above equation if the sample is not altered externally. The usefulness of the last expression relies on the fact that it allows us to understand if an atomic sample is in equilibrium or not.

2.1.2 Cooling techniques

The goal of the used cooling techniques applied in the experimental setup presented in this thesis is to trap and cool down the atoms to a PSD ≈ 2.612 in which the BEC transition takes place by increasing the atomic density and reducing the temperature of the samples. In order to achieve this, we employ two different techniques. These are laser cooling, which allows us to reach a PSD $\sim 10^{-7}$, and evaporative cooling, used to achieve the BEC regime.

2.1.2.1 Laser cooling

Laser cooling belongs to those cooling techniques that rely on the absorption of photons by atoms to cool them. The simplest one is the Doppler cooling, where the cooling mechanism is the transfer of momentum from a photon to an atom reducing its kinetic energy, thus reducing its temperature. A simple example of this technique is a system of atoms with two energy levels placed between two counter-propagating laser beams with identical frequency, ν, that is red-detuned with respect to the frequency of the transition between the two energy levels, ν_0. Due to the Doppler effect, if the velocity of an atom, v, has a component along the propagation axis of the beams, v_p, it will observe the light propagating in the opposite direction to v_p to have a frequency closer to ν_0. This favors the absorption of photons from this beam. Thus, causing an imbalance in the transfer of momenta from the photons of both beams, which results in a viscous force, $F \propto -v_p$. This mechanism is also known as optical molasses. An efficient cooling requires the repeated absorption of photons. Thus, it requires a closed transition, meaning that the atoms are excited from a ground state, $|g\rangle$, to an excited one, $|e\rangle$, decaying naturally to $|g\rangle$, so that the absorption process can be repeated. The fundamental limit to this cooling mechanism is the line-width of the transition, which can cause that atoms absorb photons that will increase their kinetic energy. The minimum attainable temperature due to this effect is known as the Doppler temperature, T_D [49].

The problem of using Doppler cooling is that it cools down but does not confine the atoms. This issue can be solved by the implementation of a magneto-optical trap (MOT) [50]. The MOT uses the Zeeman effect to trap the atoms in the center of a magnetic quadrupole trap generated by a pair of coils in anti-Helmholtz configuration. Thus, the trapping relies on the atoms being in the appropriate magnetic sublevel, which requires the light of the beams to have the appropriate circular polarization. The resultant force is of the form $F \propto -r$, where r is the distance to the center of the trap. Thus, providing the required confinement. Even if the atoms can be trapped by a restorative

force, there are limits to the maximum attainable density of the atoms due to collisions and interatomic interaction [51].

The Doppler limit can be overcome by using other mechanisms such as Sisyphus and gradient polarization cooling in which the atoms lose kinetic energy as they 'climb' the potential generated by the light beams [52], allowing for sub-Doppler temperatures. The density limit in the MOT can be overcome by techniques that rely on the more complex energy level structure of the atoms. These techniques include compressed and dark MOT (see section 4.1.3). The chosen combination of cooling techniques depends on the trade-off between the gain in density and the reduction in temperature that maximizes the PSD. However, the fact that the atoms rely on the absorption of photons sets another fundamental limit. This limit is the energy transferred by a single photon and is known as the recoil temperature, T_r.

2.1.2.2 Evaporative cooling

Evaporative cooling has been the technique used to achieve the BEC state since the first BEC experiments, which are described in [1] and [53]. In some cases, one can reach the quantum degeneracy via laser cooling, as shown in reference [54], but this is not applicable in our case since it requires a narrow-linewidth transition, which is not present or at least not practical for ^{87}Rb. Evaporative cooling relies on removing the hottest atoms allowing the remaining ones to rethermalize. The thermalization process is crucial to reduce the temperature of the sample. Consequently, the thermalization time should be short when compared to the lifetime of the atomic sample. The thermalization takes place by the elastic collision between the atoms. During thermalization atoms reach the same temperature across the whole sample when they are thermalized. However, this does not mean that the sample is in equilibrium, since atoms can change from one component to the other, being the components BEC or thermal. The mathematical model behind evaporative cooling is out of the scope of this work, but it can be found in reference [55].

The different ways of implementing this technique are magnetic evaporation, and evaporation in a dipole trap also known as all-optical evaporation. Magnetic evaporation was the method used in the first BEC experiments and is still widely used. It relies on trapping the atoms magnetically by creating a gradient in which the atoms in a particular magnetic sublevel will be trapped. The hottest ones escape when the trap depth is reduced. This process can be enhanced by the use of an "RF knife" as described in [56] that pushes out the hottest atoms.

All-optical evaporation has become more and more common over the years since it was first implemented almost two decades ago [57]. This technique allows for the creation of BECs with atoms in all the possible magnetic sublevels. The principle behind the dipole trap is that an electric field, **E**, like the one generated by a laser in our case, can modify the charge distribution of the atoms inducing a dipolar moment, **p**, in the atoms. The potential, U_d, that the atom sees is,

$$U_d = -\frac{1}{2}\langle \mathbf{pE} \rangle = -\frac{1}{2\epsilon_0 c}\mathrm{Re}(\alpha) I, \tag{2.23}$$

where α is the polarizability of the atom, I the light intensity, ϵ_0 is the vacuum permittivity and c is the speed of light. Thus, we can trap the atoms in a potential proportional to the applied light intensity, and evaporative cooling can be performed by gradually reducing the potential allowing the hottest atoms to escape while the remaining rethermalize. One can find a more complete description about dipole traps in reference [58].

2.1.3 Ultracold and cold atoms collisions

As our system is composed of ultracold Rb atoms whose temperature is in the range of tens of nK and cold K atoms in the mK range, we require a model describing the interaction between them. The starting point for our model is the model for collisions between ultracold atoms and background atoms described in reference [59]. In their model they distinguish between the quantum and classical regimes. In the quantum regime, the collisions are usually classified as *s*,*p*,*d*... depending on the energy of the collision adding higher order terms for higer energy collisions. However, when the energy of the collision is high enough, the classical treatment matches with the quantum one. In this model, the crossover energy, E_c, delimits the border between the two regimes and is given by [59]

$$E_c \approx 2\frac{\hbar^{12/5}}{C_6^{2/5}}\frac{1}{m_{Rb}m_K^{1/5}}E_{col}^{1/5}, \tag{2.24}$$

where m_{Rb} and m_K are the masses of Rb atoms and K atoms, respectively, E_{col} is the collision energy between both atomic species, approximated here as the kinetic energy of the K atoms because of the temperature difference and C_6 is the van der Waals coefficient of the interaction between both atoms. In our case, we do not consider the background atoms but cold atoms instead. The typical energy of the collisions between a cold atom and an ultracold atom is at least three orders of magnitude larger than for a collisional process that can be considered purely as quantum, since cold atoms temperature is of the order of mK while ultracold ones temperature is less than a muK. Thus, we tried to understand our experimental results using this model. I report the corresponding results in section 4.4.1. For the collision between these two atomic species C_6=4290(2)$a_0^6E_h$ [60], where E_h is the Hartree Energy. Using equation 2.24 we calculated $E_c \simeq 300\mu$K. To calculate the collisional cross-section, we integrate the differential cross-section, $d\sigma_K$, given by the following expression

$$d\sigma(E_t) = \begin{cases} \alpha & \text{if} \quad E_t \leq E_c \\ \alpha \left(\frac{E_c}{E_t}\right)^{7/6} & \text{if} \quad E_t > E_c \end{cases} \tag{2.25}$$

where E_t is the energy transferred to the ultracold atom in a collisional process and $\alpha = \sigma_g^{class}(E_c)$, with $\sigma_g^{class}(E_c)$ the differential cross-section for a classical collision with energy E_c,

$$\alpha = \sigma_g^{class}(E_c) = \frac{\pi}{6}\left(\frac{9C_6^2}{E_{col}}\right) E_c^{-7/6}. \tag{2.26}$$

By integrating equation 2.25 we obtained an expression for the total scattering cross section, σ,

$$\sigma = \int_0^{E_c} \alpha dE_t + \int_{E_c}^{E_{max}} \alpha \left(\frac{E_c}{E_t}\right)^{7/6} dE_t. \tag{2.27}$$

The last equation contains the sum of the 'quantum' and 'classical' parts of σ. Consequently, E_{max} is the maximum possible energy for a classical collisional process. Since we can consider that the ultracold atoms are effectively at rest in comparison with the cold atoms, due to their temperature difference, we consider E_{max} as the energy of an elastic collision. Therefore, we calculate it as,

$$E_{max} = 4\frac{m_{Rb}m_K}{(m_{Rb}+m_K)^2}E_K. \tag{2.28}$$

Where E_K is the kinetic energy of a cold K atom. The scattering rate, γ_K, due to the collisions between Rb and K atoms is given by:

$$\gamma_K = n_K \sigma v_K, \tag{2.29}$$

where n_K is the atomic density of K and v_K the average velocity of the atoms. We calculate v_K as the average thermal velocity, so $v_K = \sqrt{2k_B T_K}$ with T_K the temperature of the K atoms. Considering that the Rb atoms will escape from the trap after one collision with the K atoms due to the energy of the collisions being orders of magnitude higher than the trap depth, we can model the collisional process as one body losses. In particular, the trap depth is less than 1μK while the energy of the collision between both atomic species is of the order of the temperature of the K, around 1mK. If we consider N as the number of Rb atoms, we obtain the following expression,

$$\dot{N} = \frac{dN}{dt} = -\gamma_K N, \tag{2.30}$$

We use the last equation to model the losses of Rb atoms due to the collision with K, which in turn helps us to understand the mechanism behind the dissipation of Rb atoms.

2.1.4 Condensate growth

To understand the physics behind the BEC transition in a dissipative environment, we firstly need a model that explains the condensate growth in the equilibrium case. Even in the equilibrium case, this is a complicated problem. In the following, I provide a summary of the development of such a model. The starting point is reference [61], where the authors formulated a quantum kinetic master equation for a dilute gas of Bosons without a trapping potential. The next step was taken in reference [62], in which the authors added a trapping potential to the previous model, equivalently to the trapping potential we use to trap our Rb atoms, thus providing a master equation for the condensate growth in a trapping potential. This master equation was then used to obtain a rate equation that models the problem [63]. The rate equation is the following,

$$\dot{N} = 2W^{+}(N)\left[\left(1 - e^{(\mu_n - \mu)/kT}\right) + 1,\right] \tag{2.31}$$

where μ_n and μ are the chemical potentials of the condensate and the thermal bath, respectively. W^{+} is the transition probability of an atom to be transferred from the thermal phase to the BEC phase. The authors assumed a thermalized atomic sample, with a thermal component at a temperature T. Formally the BEC component has no temperature, but as it is thermalized together with the thermal component an atom changing from the BEC to the thermal component has temperature T. This equation represents the particular case of the growth of a BEC component of N atoms for a starting point of an empty BEC component. The BEC component is in contact with the thermal bath, and the thermal bath does not deplete. However, as explained in [64], the experimental data does not match the theory, which is particularly true for the low-temperature case. The cause behind this is the non-triviality in the calculation of the transition probabilities when the different energy levels in the thermal bath intervene. Nevertheless, this rate equation was probed to be still useful as it is in good agreement with the experimental data by adjusting the parameters to it [64]. In section 4.3.3 we apply equation 2.31 as a starting point to develop our rate equation. In our model, we take into account, in a simplified manner, the depletion of the thermal bath and the dissipation of Rb atoms due to the collisions with the K atoms to model the experimental data concerning the BEC transition in a dissipative environment.

2.2 Single atom quantum engine

2.2.1 From classical to quantum thermodynamics

In our single-atom quantum engine, we essentially have a single particle in a harmonic oscillator, with frequency ω, immersed in a thermal bath. In the quantum regime, the thermal energy is on the order of the energy of the harmonic oscillator $k_B T \sim \hbar\omega$, contrasting with a classical engine in which the thermal noise dominates. Considering a quantum system, the energy is quantized in different levels with a characteristic energy E_n, with an associated probability $P_n = exp(-E_n/k_B T)$. We can use the Boltzmann probability distribution of occupation since we have a single particle, thus reducing Bose and Fermi statistics to the Boltzmann distribution.

To explain the parallelism between the classic and quantum cases I first calculate the total internal energy of our system, U, given by,

$$U = \sum_n P_n E_n, \tag{2.32}$$

differentiating, we obtain the following expression:

$$dU = \sum_n E_n dP_n + \sum_n P_n dE_n. \tag{2.33}$$

This equation may remind the reader of the first principle of classical thermodynamics, $dU = đQ + đW$. To relate the terms in equation 2.33 with the classical thermodynamics quantities, we take the von Neumann entropy [65],

$$S = -k_B \mathrm{Tr}(\rho \log \rho), \tag{2.34}$$

where ρ is the density matrix of the system. In the case of a harmonic oscillator, this equation reduces to the Shannon entropy:

$$S = -k_B \sum_n P_n \log P_n, \tag{2.35}$$

we differentiate again to obtain the following expression,

$$dS = -k_B \sum_n \cancel{\log P_n}^{-\frac{E_n}{k_B T}} dP_n - k_B \sum_n \cancel{dP_n}^{0} = \sum_n \frac{E_n}{T} dP_n, \tag{2.36}$$

from where we can identify $đQ$ as,

$$đQ = TdS = \sum_n T\frac{E_n}{T} dP_n = \sum_n E_n dP_n. \tag{2.37}$$

We conclude the following identification,

$$dU = \underbrace{\sum_n E_n dP_n}_{đQ} + \underbrace{\sum_n P_n dE_n}_{đW}. \tag{2.38}$$

The last expression shows how the heat and work are related to the energy and probabilities of the quantum levels.

2.2.2 Thermodynamic transformations in the quantum level

To realize a quantum engine we need to understand the thermodynamics transformations in terms of the variables that define our system, which are P_n and E_n, the probability and the energy of the different energy levels of the single atom respectively. In the following

I explain and depict the different thermodynamic transformations. In these depictions, the single atom is shown in its lowest level. However, the atom can move between the different energy levels as energy is transferred between the bath and the atom. This can be measured by using sideband Raman spectroscopy [66].

1. The quantum adiabatic transformation depicted in figure 2.2 implies a transformation in which no heat is transfer from the bath to the working fluid or single atom. This means varying the trapping potential while the interaction between the two species is "switch off" as explained in section 2.2.3 by tuning the magnetic field to zero crossing of the interspecies scattering length. Thanks to this, there is no way for the single atom to interchange heat with the thermal bath, which equates to $dQ = 0$ and consequently $dP_n = 0$.

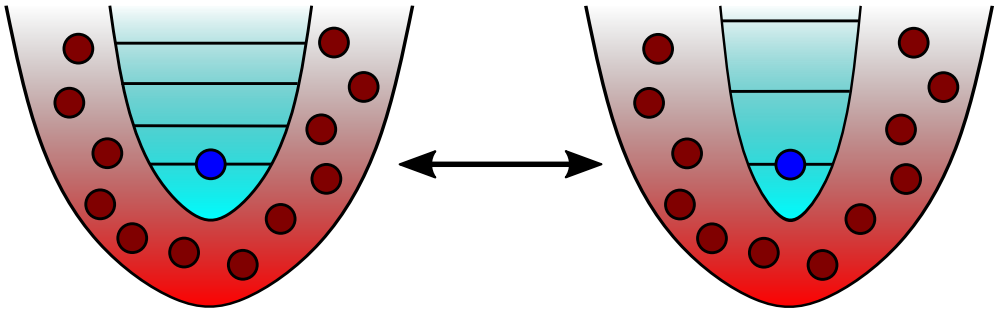


Figure 2.2: Depiction of the quantum adiabatic transformation. The blue particle represents the single K atom trapped in the tweezer, represented by the blue background, the horizontal lines represent the energy levels of the harmonic trap. The red particles represent the Rb atoms trapped in the dipole trap, represented by the red background.

2. The quantum isothermal transformation depicted in figure 2.3 requires the two species to interact in order for the single atom to constantly retermalize with the bath. If we vary the tweezer trapping potential while keeping constant the trapping potential of the bath, i.e. keeping its temperature constant, we can keep the temperature of the single atom effectively constant if the transformation is slow enough. The change in the tweezer trapping potential leads then to a change in the energy levels spacing.

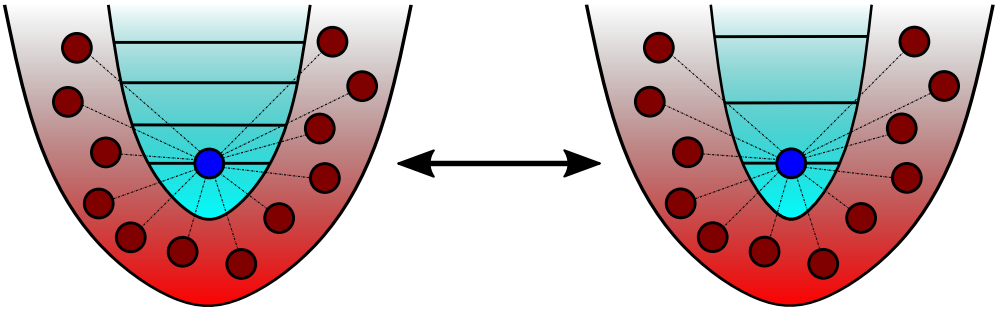


Figure 2.3: Depiction of the quantum isothermal transformation. The dashed lines represent the interaction of the Rb atoms with the single K atom.

3. The quantum isochoric transformation depicted in figure 2.4 involves no work done in the system which in this system equates to $dE_n = 0$. To achieve this we put the single atom interacting with the bath and we change the temperature of the bath. This translates into a change of the occupation probability distributions, so that $dP_n \neq 0$ and thus $dS \neq 0$. While this is done, the tweezer potential is kept constant so that $dE_n = 0$ fulfilling the requirement of a isochoric transformation.

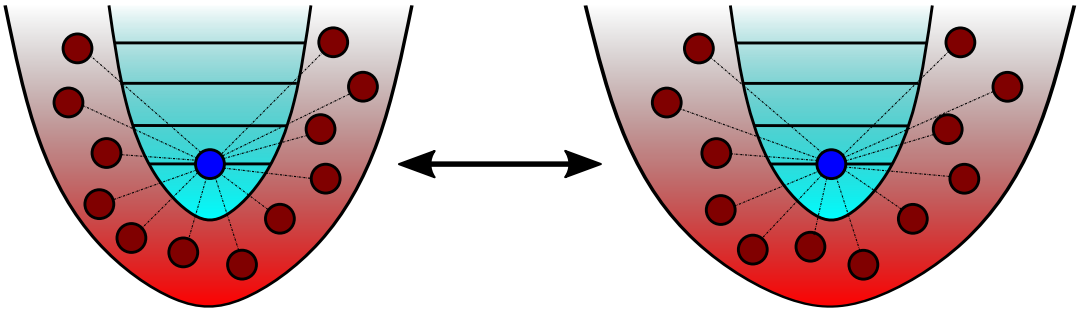


Figure 2.4: Depiction of the quantum isochoric transformation.

4. The quantum isobaric transformation is depicted in figure 2.5. To understand this transformation we must understand what is the pressure equivalent to pressure in this system. In classical thermodynamics the relation between the internal energy, U, and the pressure, P, is,

$$P = -\left(\frac{\partial U}{\partial V}\right)_S, \tag{2.39}$$

replacing U by its definition given in equation 2.38, we obtain the *quantum pressure*,

$$\Pi = -\sum_n P_n \left(\frac{dE_n}{da_{ho}} \right), \tag{2.40}$$

where a_{ho} is the harmonic oscillator length defined as $a_{ho} = \sqrt{\hbar/m\omega}$. Here, we have take into account that the single atom placed in the tweezer is a quantum haromic oscillator with frequency ω and mass m. Using that,

$$U = \sum_n P_n E_n = \sum \exp\left(-\frac{\beta}{\hbar\omega} E_n \right) E_n, \tag{2.41}$$

with $\beta = \hbar\omega/(k_B T)$, we obtain,

$$\Pi = \frac{\sqrt{\xi}\sinh\beta}{\cosh\beta - 1}, \tag{2.42}$$

where $\xi = hm\omega^3$. We can then rewrite the last expression as,

$$\frac{\hbar\omega}{k_B T} = \ln\left(\frac{\Pi + \xi^{1/2}}{\Pi - \xi^{1/2}} \right), \tag{2.43}$$

this provides us an expression of how we can vary ξ together with T to keep Π constant. We can change arbitrarily T by changing the temperature of the bath by changing its trapping potential and ξ by changing the trapping potential of the single atom.

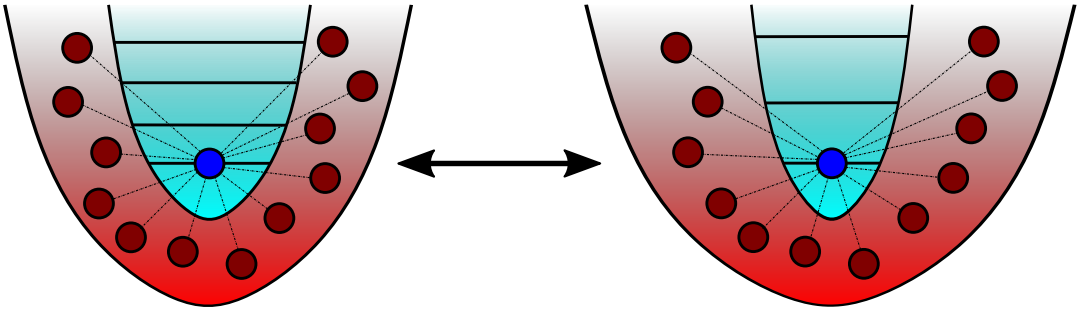


Figure 2.5: Depiction of the quantum isobaric transformation.

2.2.3 Feshbach resonances and tunable interactions

To model the short-range interaction between a pair of atoms, we can use a molecular potential that depends on the internal states of such atoms. We can consider the collision as a simple two-channel model, the open and closed channels. Figure 2.6 shows such model. For an atomic separation, R and a total energy, E, we have that $V_{bg}(R)$ is the open channel potential for which $V_{bg}(R \to \infty) < E$ and $V_c(R)$ is the closed channel potential for which $V_c(R \to \infty) > E$ [67]. In the closed channel, the internal states of the atoms change as a result of the collision.

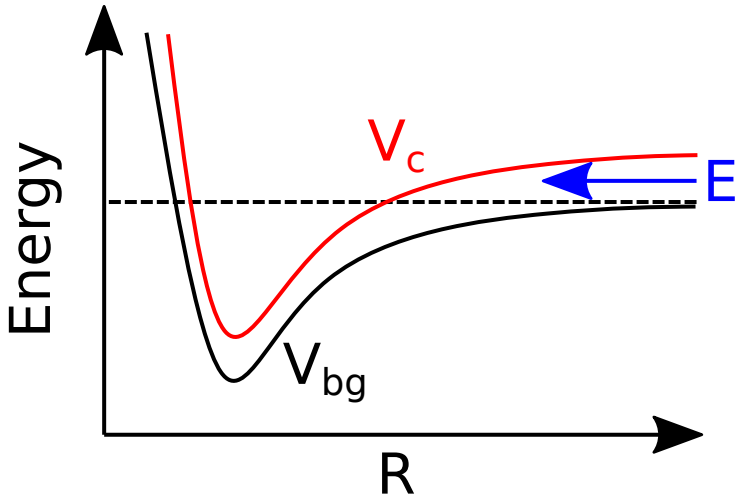


Figure 2.6: The the two channel model used to describe the physics behind the Feshbach resonances where R is the atomic separation. [67]

We can shift the potential energy of the closed channel thanks to its dependence on the internal levels of the atoms. In our case, we will use Feshbach magnetic resonances,

which, as the name indicates, are dependant on the magnetic field that shifts the energy of the magnetic sublevels. When we tune the potential energy of the closed channel close to the open channel, we observe a change in the collisional properties. The explanation behind this is that the system goes into a metastable molecular state. At the point in which both energies are the same, we find a resonant behavior, and the scattering length, a_{sc}, diverges. The shape of this resonant behavior is described by:

$$a_{sc}(B) = a_{bg}\left(1 - \frac{\Delta_{sc}}{B - B_0}\right), \tag{2.44}$$

where B is the applied magnetic field, a_{bg} is the scattering length corresponding to the open channel, Δ_{sc} is the amplitude of the resonance, and B_0 is the value of B at which the resonance takes place.

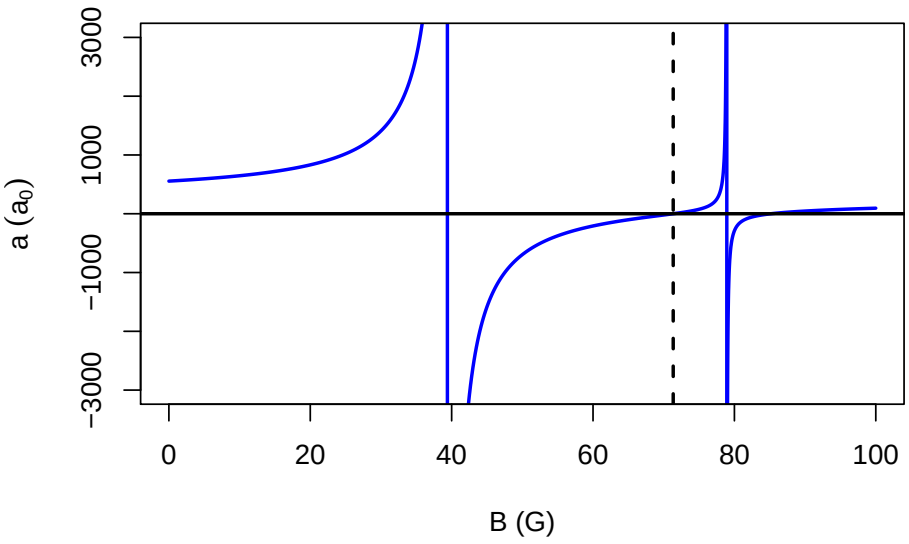


Figure 2.7: Scatering length of the interaction between ^{87}Rb$|1,1\rangle$ and ^{41}K$|1,1\rangle$ as a function of the applied magnetic field where we can observe two Feshbach resonances [60]. The dashed line at B=71.34G marks the zero-crossing of the scattering length.

To control the interaction between the two atomic species we take advantage of

the presence of two heteronuclear Feshbach resonances between $^{87}\text{Rb}|F = 1, m_F = 1\rangle$ and $^{41}\text{K}|F = 1, m_F = 1\rangle$. While the ground state of both species is $F = 1$, in order to obtain the atoms in the magnetic sublevel $m_F = 1$ we need to distillate the desired sublevel by applying a magnetic field that favors the trapping of the required sublevel. Figure 2.7 shows the scattering length, a_{sc}, between the cited atomic species versus the applied magnetic field. The presence of two low-field Feshbach resonances allows for the easy control of interaction for the easily achievable range ∼50G-70G. In this range, the interaction goes from attractive to repulsive crossing zero. Which means we can "switch off" the interaction between the species. Previous experimental results [68] demonstrated that for these atomic species, the losses due to three-body collisions in the required range should not be a problem for the realization of our experiment.

2.2.4 Quantum engines

In this section, I explain the different quantum engines implementations proposed in reference [69]. We plan to realize these implementations and we are currently working towards the completion of the experimental setup. The current state of development together with some discussion can be found in chapter 5. In these implementations, we will use ultracold ^{87}Rb atoms as our thermal bath and a single ^{41}K as the working fluid. In this context, ultracold means that the quantum effects become relevant without necessary reaching the quantum degeneracy, this regime is in the order of few μK. As explained in section 2.2.3, the interaction between these two atomic species can be tuned, which is used for these implementations. Again it is difficult to depict how the single atom jumps between the different energy levels during these transformations. Due to the quantum nature of the system the atom can be measured in different levels for the same measurement. Thus, the results will have to be averaged over several cycles.

2.2.4.1 Quantum Carnot engine

The classic Carnot cycle consists of two isothermal and two adiabatic transformations. Analogously, the Quantum Carnot engine (QCE) consists of two isothermal and two adiabatic quantum transformations which are realized as explained in section 2.2.2. Figure 2.8 depicts the QCE. For a realistic application we chose the temperature of the bath to be $T_A = \hbar\omega_A/2k_B$, where ω_A refers to the trapping frequency of the the tweezer. T_A refers to the initial temperature of the single atom at the beginning of the cycle, achieved by sympathetic cooling using the thermal bath. This makes $P_0 + P_1 + P_2 > 0.99$ for a single K atom, with P_i the occupation probability of the different energy levels of the harmonic trap.

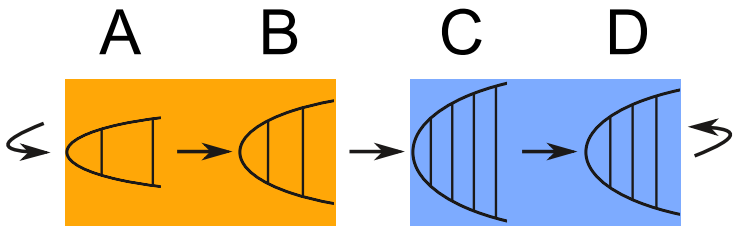


Figure 2.8: Depiction of the Quantum Carnot engine. [69] In here, A→B and C→D are isothermal transformations while B→C and D→A are adiabatic transformations. The colors represent the hot (orange) and cold (blue) baths.

While for the adiabatic transformation we only have to "switch OFF" the interactions by tuning the magnetic field so $a = 0$, with a the interespecies scattering length. For the isothermal transformations we have to take into account that in the ultra-cold regime the heat capacity of the bath is reduced which has to be compensate by making the atom-bath interaction stronger as we approach such regime [70]. This in turn, increases the inelastic scattering rate which scales as $\propto a^4$. The consequence of this, is that the survival probability of the K atom in the tweezer decreases as the strength of interaction increases. In fact, the survival probability can be understood as an an *effective friction*, as only the cycles in which the K atom survives in the trap count towards the calculation of the real efficiency. Obviously, the real efficiency, η_{real}, is the product of the maximum theoretical

efficiency, η_{max}, and the survival probability of the atom in the trap. In any case, the required number of collision for a K atom to rethermalize with the bath is in the order of ∼4 collisions, result found following the work of reference [71]. Thus, the strength of the interactions depend on the transformation time, t_f, as we can decrease the interaction strength and increase the transformation time. Therefore, we have to look for the optimal point between t_f and interaction strength which maximizes η_{real}. Figure 2.9 depicts the evolution of the trapping frequencies of the bath and the tweezer for the used Quantum Carnot cycle.

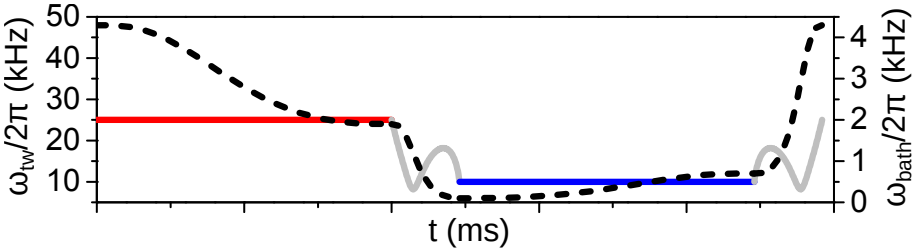


Figure 2.9: Evolution of the trapping frequencies of the bath (solid line) and the tweezer (dashed line) for the Quantum Carnot engine. [69] The colors simply illustrate the hot (red) and cold (blue) baths.

In figure 2.10(a) the authors report the ratio of the maximum real efficiency, η_{real}, and the maximum efficiency, η_{max}, versus the starting temperature, T_A. Due to the correlation between the transformation time and the efficiency, a fixed value of t_f is chosen, in this case t_f =1ms. From the calculations, it can be concluded that for a T_A below 1μK the real efficiency drops substantially. Figure 2.10(b) reports η_{real} versus η_{max} for different values of t_f and $T_1 = 1.1\mu$K. As t_f is increased the interaction strength can be decreased which decreases the effective friction. One may conclude from here that the bigger t_f the better efficiency we get. Although, this does not take into account the photon scattering rate due to the tweezer light. As discused in section 5.2.1, the tweezer light causes the heating of the atom which which limits the practical value. The authors found that the most convenient setting of parameters is T_A =1.1μK and t_f =1ms for the isothermal transformations. The information we can extract from this graph is that even if this

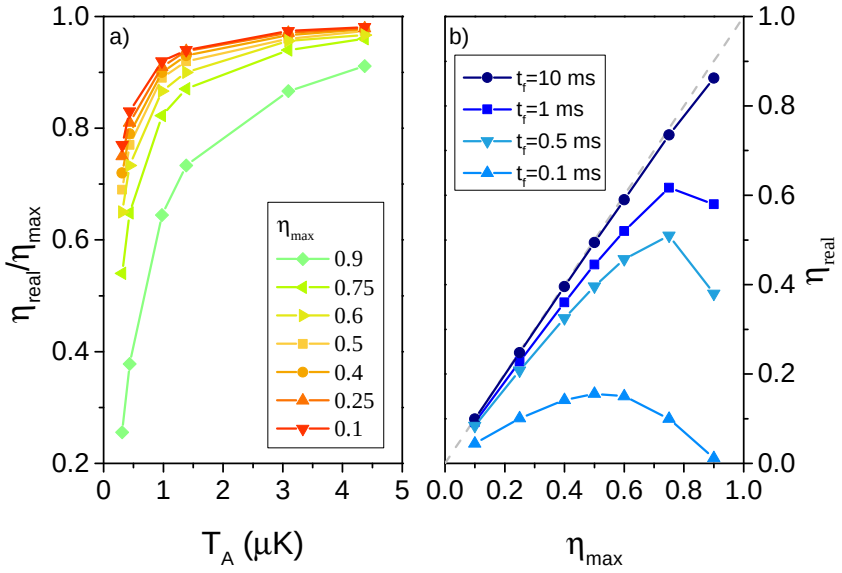


Figure 2.10: Plot a) reports the ratio of real efficiencies and the maximum theoretical efficiency as a function of the starting temperature T_A for a QCE with two isothermal strokes of 1 ms each. Plot b) shows the maximum real efficiency versus the maximum theoretical efficiency for a QCE with $T_A = 1\mu K$ for different lengths of the isothermal transformations. [69]

engine is not subject to the usual effects of the friction of the classical engines, it can suffer an effective friction which can be quite detrimental. This friction is not really a purely quantum effect since it is essential due to the atom escaping from the trap.

2.2.4.2 Quantum Otto engine

Moving to the next quantum engine, we encounter the Quantum Otto engine. The corresponding cycle is depicted in figure 2.11. The authors used the same initial conditions as for the Quantum Carnot Engine to facilitate a more direct comparison. Thus, they set $\eta_{max} = 0.75$ and $T_B = 2T_A$. The power obtained using the route in figure 2.12 is $\mathcal{P}/k_B = 2.36$ mK/s, with $\tau = 2.35$ ms and $\eta_{real} = 0.68$. Therefore a real ultra-cold QOE is both more efficient and more powerful than a real QCE with the same initial conditions and the same maximum theoretical efficiency.

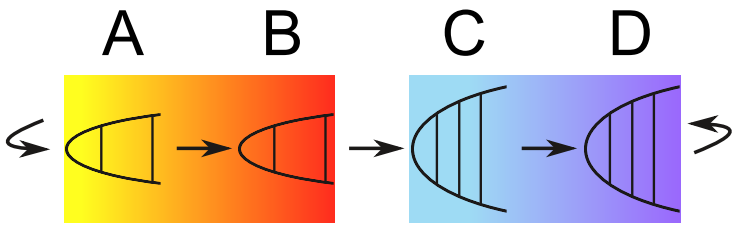


Figure 2.11: Depiction of the Quantum Otto engine. [69] In here, A→B and C→D are isochoric transformations while B→C and D→A are adiabatic transformations. The colors represent the hot (yellow-red) and cold baths (blue), and the color gradient denotes the change in temperature of the baths.

To close the cycle it must be ensured that $T_B/T_D > \omega_A/\omega_D$ [72], where ω_i the trapping frequency of the tweezer. The maximum theoretical efficiency of the Quantum Otto engine is $\eta_{max} = 1 - \Delta_D/\Delta_A = 1 - T_C/T_B$ which can be attained by using super-adiabatic transformations. Super-adiabatic means that the temperature gradient during the transformation is sharper than for an equivalent adiabatic transformation. In this case, the isochoric strokes are also super-adiabatic which reduces friction effects in the bath. The length of these strokes is 1 ms for a good compromise between the required length and the strength of the interactions. The super-adiabatic transformations are similar to the ones in the Quantum Carnot case. However, the transformation (B→C) one may be faster because of the reduced decompression. Also, the effective friction of the Quantum Otto engine is reduced with respect to the QCE due to the higher average temperature of the two baths as the interaction strength can be lowered [70]. The work done in one cycle is

$$W_{QOE} = \sum [E_n(B) - E_n(C)] \sum [P_n(B) - P_n(A)], \tag{2.45}$$

using this expression, the power extracted is $\mathcal{P}/k_B = 2.36$ mK/s, with $\tau = 2.35$ ms. The real efficiency is $\eta_{real} = 0.68$ which is higher than for the classical case and higher than for the Quantum Carnot engine.

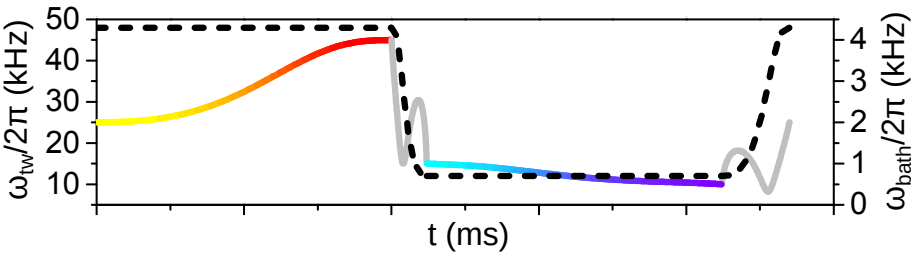


Figure 2.12: Evolution of the trapping frequencies of the bath (solid line) and the tweezer (dashed line) for the Quantum Otto engine. [69] The colors simply illustrate the hot (yellow-red) and cold (blue) baths, the color gradient represents the change in temperature.

2.2.4.3 Quantum Diesel engine

Lastly, the authors studied the Quantum Diesel engine, which is depicted in figure 2.13. Similarly to the Quantum Otto engine, the authors used the same initial conditions, so $\eta_{max} = 0.75$. They additionally imposed that ω_D/ω_A is 0.9 times the value in the Quantum Otto engine, which yielded $\omega_A/\omega_B \simeq 1.23$.

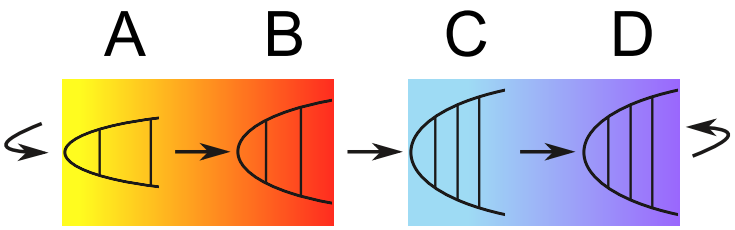


Figure 2.13: Depiction of the Quantum Diesel engine. [69] In here, A→B is an isobaric transformation, C→D is an isochoric transformation, and B→C and D→A are adiabatic transformations. The colors represent the hot (yellow-red) and cold baths (blue), and the color gradient denote the change in temperature of the baths.

The total cycle time is $\tau = 2.42$ ms, so the authors obtained that the power that can be extracted is $\mathcal{P}/k_B = 2.54$ mK/s. The real efficiency is $\eta_{real} = 0.64$, which sits in between the efficiencies of the Quantum Carnot and Otto engines. In this case, the transformations are the same as those of the Quantum Otto engine but the (A→B) isochoric transormation is replaced by a quantum isobaric expansion. Transformation in

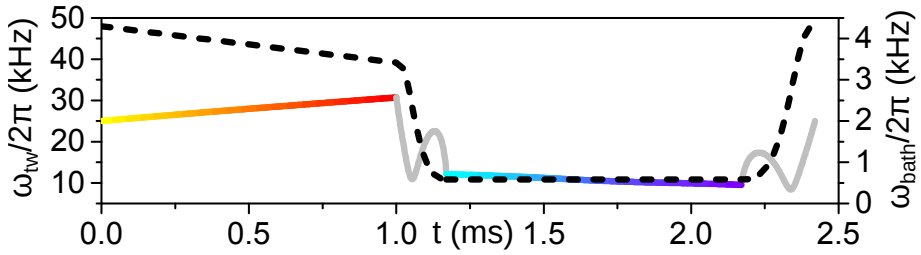


Figure 2.14: Evolution of the trapping frequencies of the bath (solid line) and the tweezer (dashed line) for the Quantum Diesel engine. [69] The colors simply illustrate the hot (yellow-red) and cold (blue) baths, the color gradient represents the change in temperature.

which the heat is transferred to the working fluid. The maximum theoretical efficiency is given by the following expression,

$$\eta_{max} = 1 - \frac{\omega_D}{3\omega_A} \frac{\left(\frac{\omega_A}{\omega_B}\right)^{3/2} - 1}{\left(\frac{\omega_A}{\omega_B}\right)^{1/2} - 1}. \tag{2.46}$$

During the isobaric stroke the temperature of the bath is varied following equation 2.43, the authors used a linear compression ramp for simplicity. In this case it is not possible to realize a super-adiabatic transformation for the isobaric stroke. Yet again, the authors chose 1 ms for the strokes in which thermalization is required and the corresponding evolution of the trapping frequencies of the bath and the tweezer are depicted in figure 2.14. The work done by the Quantum Diesel engine is

$$W_{QDE} = \Pi_{AB} \Delta V_{AB} - \sum E_n(C)[P_n(C) - P_n(D)] \tag{2.47}$$

where ΔV is the change in volume during the isobaric expansion. The authors report that the power that can be extracted is $\mathcal{P}/k_B = 2.54$ mK/s for a total cycle time of $\tau = 2.42$ ms. The real efficiency is $\eta_{real} = 0.64$ siting in between the performance of the Carnot and Otto engines.

2.3 The Frenkel-Kontorova model

The last part of my thesis is devoted to the FKM. The FKM was introduced in 1938 by Yakov Frenkel and Tatiana Kontorova to describe the structure and dynamics of a crystal lattice near a dislocation core. This model uses a simple depiction of such a system. The interaction between atoms in a lattice is an infinite-range spring interaction potential, which is non-realistic. The potential due to the crystal lattice or substrate potential is a simple sinusoidal potential. This model is depicted in figure 2.15. The energy of this system, for N particles with x_i and p_i their position and momenta, respectively, is

$$E = \sum_{i=1}^{N} \frac{p_i^2}{2m} + \frac{1}{2} \sum_{i=1}^{N-1} (x_{i+1} - x_i - a)^2 + \sum_{i=1}^{N} \left[V_0 - V_0 \cos\left(2\pi x_i / b\right) \right], \tag{2.48}$$

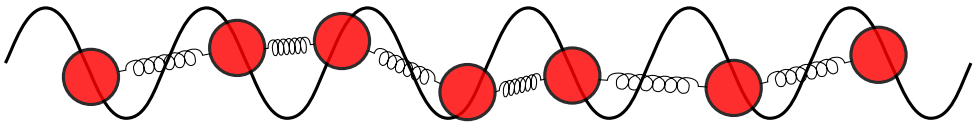


Figure 2.15: Depiction of the Frenkel-Kontorova model.

where m is the mass of the particles, a is the natural length of the springs connecting the particles, V_0 is the strength of the substrate potential, and b the substrate potential spacing. From this equation, it is easy to conclude that there are two characteristic length-scales, one related to the interaction, a, and one related to the substrate, b. If the ratio between these two length-scales is rational or irrational, the particle configuration is *commensurate* or *incommensurate* with the substrate, respectively. An ideal system, with no borders and infinite particles, in the incommensurate phase, can undergo the so-called Aubry phase transition. In this transition, as one increases V_0 over a certain critical value, the ground state of the system transitions from an *unpinned* to a *pinned* configuration [39]. The increase of V_0 limits the particles to the regions closer to the minima of the lattice, meaning that the function that defines the particle position in the system becomes discontinuous, also known as breaking of analyicity.

The phonon spectrum of the ground state configurations shows another characteristic of the Aubry transition. In the unpinned case, the minimum frequency of the phonon spectrum is *zero*, corresponding to an excitation mode of zero energy known as phason in which particles slide energy-free between the possible configurations. That is why the unpinned phase is also known as the sliding phase.

The unpinned phase presents another property that requires an extension of the Frenkel-Kontorova model known as the Frenkel-Kontorova-Tomlinson model. This model adds an external force of magnitude F applied to all the particles. In this system, one can show that for an unpinned configuration, one can displace the center of mass of the system for $F \to 0$. This phenomenon is known as superlubricity, and it has been the object of different studies using the cited model [73, 74].

The Frenkel-Kontorova model can be extended to a more general form given by

$$E = \sum_{i=1}^{N} \frac{p_i^2}{2m} + \frac{1}{2} \sum_{i=1}^{N-1} c_1 V_{\text{int}}(x_{i+1} - x_i) + \sum_{i=1}^{N} \left[V_0 - V_0 \cos\left(2\pi x_i / b\right) \right], \tag{2.49}$$

where c_1 is the strength of the interaction and V_{int} is the interaction potential. This has been proven useful to describe a multitude of condensed matter systems. Some examples are the study of dislocation dynamics in solids [75], surfaces and adsorbed atomic layers [76], incommensurate phases in dielectrics [77], crowdions [78], magnetic chains [79], Josephson junctions [80] and tribology [81] using the Frenkel-Kontorova-Tomlinson model. Simulating this model with cold atoms will allow for a more realistic implementation and it could be easily extended to 2D. Moreover, the flexibility of cold atoms systems will allow to simulate a variety of systems that can be described using this model.

Chapter 3

Experimental setup

I devoted the second and third years of my PhD to design, build, and commission an experimental setup able to cool down and manipulate two atomic species in the ultracold regime. I have divided this setup into five different blocks corresponding to the sections of this chapter:

- In **section 3.1** I explain the vacuum system. It provides the environment for the cooling and trapping of the atoms, as ultracold atomic samples would heat up in contact with background atoms which are at a higher temperature.

- The laser system is described in **section 3.2**. It is used for both cooling down and trapping the atoms to manipulate them in the ultracold regime.

- **Section 3.3** explains the optical tweezer setup. The function of it is to trap and image a single atom so that we can realize our single-atom quantum engine.

- In the following section, **section 3.4**, I develop the imaging system. We use the imaging system for data acquisition. In this section, I also explain how we quantify the number of atoms and temperature from the acquired images.

- The last section, **section 3.5**, contains a description of the control system used to control the different components of the experiment from the control computer.

3.1 Vacuum system

The vacuum system contains the sources of both atomic species in two ampoules. It is required as the cold atomic samples would be heated up by collisions with background atoms. These are atoms coming either from the trapped air or the atomic sources that are at a much higher temperature than the cold atoms. To achieve the cold regime pressure required is in the order of 10^{-7} mbar. To reach the ultra-cold regime the pressure required has to be as low as 10^{-10} mbar. Our vacuum system, shown in figure 3.2 and schematized in figure 3.1, is divided into two chambers. The first one is known as the 2D MOT chamber, where we precool the atoms, using a MOT (see section 2.1.2.1) that confines and cool the atoms across two directions, from room temperature vapours, providing a cold atoms flux. These are captured in the 3D MOT chamber, also known as the science chamber, by performing laser cooling across the three spatial directions.

Both chambers are connected by a differential pumping stage, which is essentially a hole with 1 mm diameter and 1 cm allowing us to keep the pressure difference of three orders of magnitude. Thus, we can maintain the 2D MOT pressure in the order of 10^{-7}mbar while maintaining the pressure in the 3D MOT in the order of 10^{-10}mbar. The higher pressure in the 2D MOT helps us to obtain a higher-density flux of atoms that we cool to the ultracold regime in the 3D MOT. Thus, the use of two chambers allows for an efficient trapping and cooling of the atomic species from samples at room temperature to the ultracold regime.

The 2D MOT chamber was built from a single block of titanium. It has four rectangular windows glued to it, using the glue Aremco 631. The windows' size is 4×10cm.

This chamber is connected to the 3D MOT chamber by the already mentioned differential pumping stage. On the other end of the 2D MOT, we have an ion pump that allows us to keep the vacuum. On this end, we connected to the chamber two metallic bellows that contain the Rb and K ampules. There is also a viewport used for the pushing beam and a valve to connect the turbopump used only in the initial pumping.

We use a glass cell as our 3D MOT chamber, maximizing the optical access. In it, we load the atoms in a 3D MOT and evaporate them into the BEC state. It is also called the science chamber. The pressure can be as low as $\sim 10^{-10}$mbar thanks to the differential pumping stage and the ion pump it has attached.

Moving onto the technicalities of how we built the vacuum system, we firstly used a turbopump connected to two valves placed in each of the chambers. This stage is shown in figure 3.3, which shows the early stages in the experiment before building the laser system. During this process, we baked the system at 100°C for two weeks by wrapping the system in aluminum foil and heating it with heating tapes. After this, the valves were closed, and the ion pumps connected. The next step was to test that the system was closed. Once we did this, we disconnected the turbopump. We used two different ion pumps to keep the pressure difference between both chambers. In the 2D MOT the pressure was and is higher due to the vapor pressure of the atomic samples. Due to a malfunction, the ion pump in the 2D MOT is not longer working but the pressure is stable using only the one in the 3D MOT.

The 2D MOT chamber has four magnetic coils in anti-Helmholtz configuration placed around this chamber provide the required magnetic field for the realization of the MOT. In the 3D MOT, we have two coils that can we switch from anti-Helmholtz to Helmholtz configuration using a four-way relay allowing to generate the trapping potential for the MOT and the tuning of the scattering length via Feshbach resonances (see section 2.2.3), respectively.

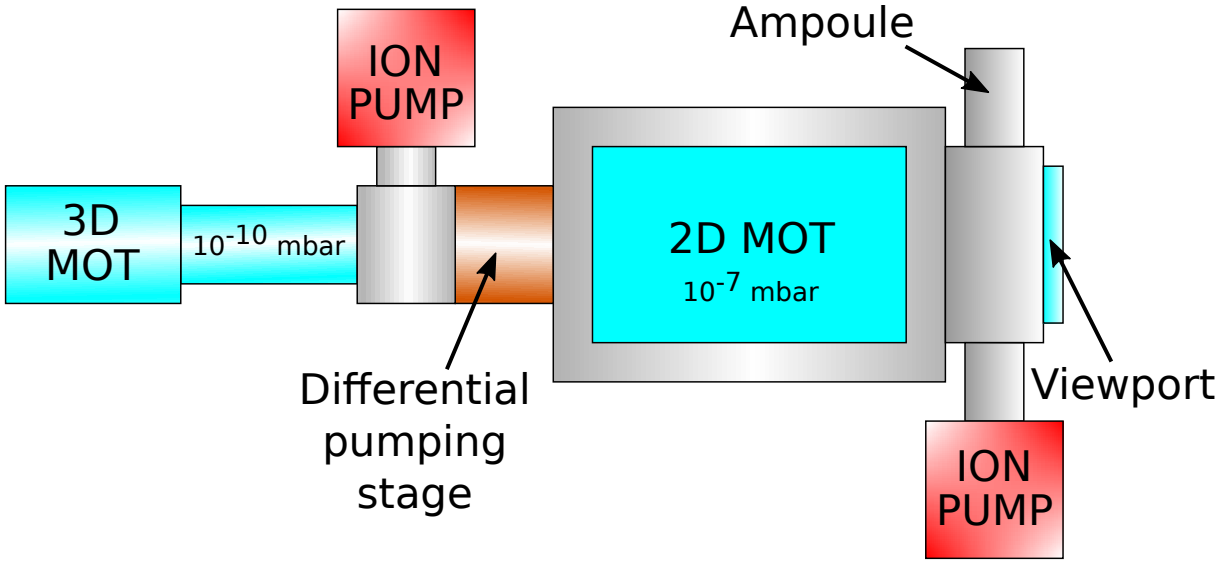


Figure 3.1: Schematics of the vacuum system.

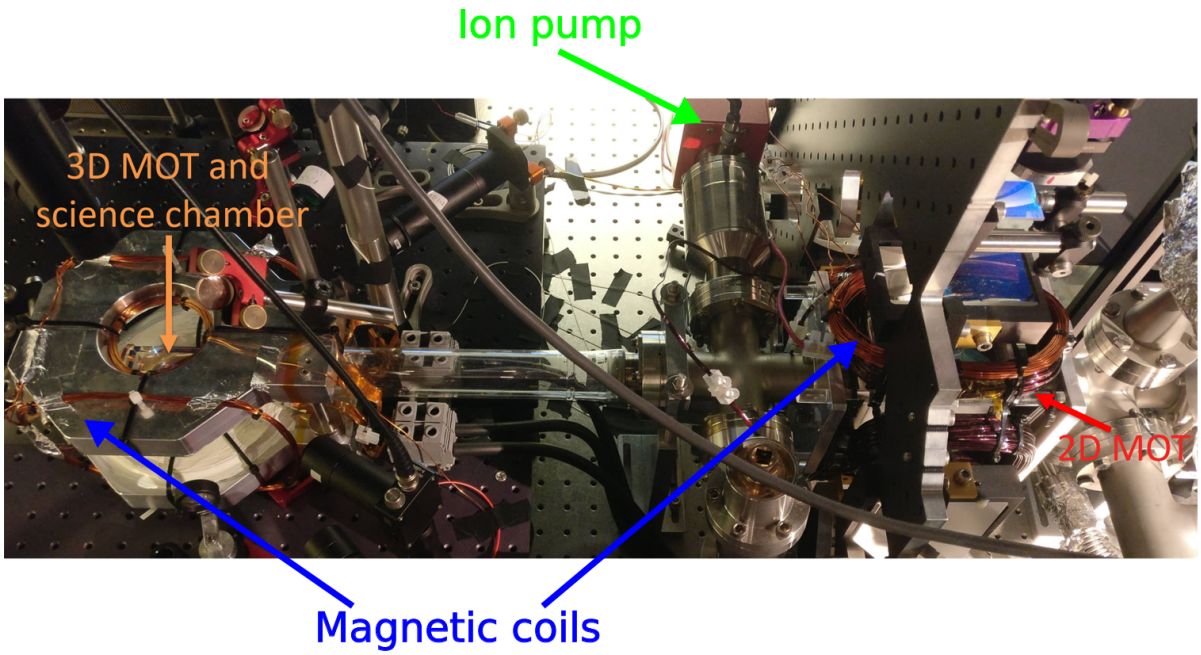


Figure 3.2: Picture from the top of the vacuum system, with the 3D MOT chamber in the left and the 2D MOT chamber in the right.

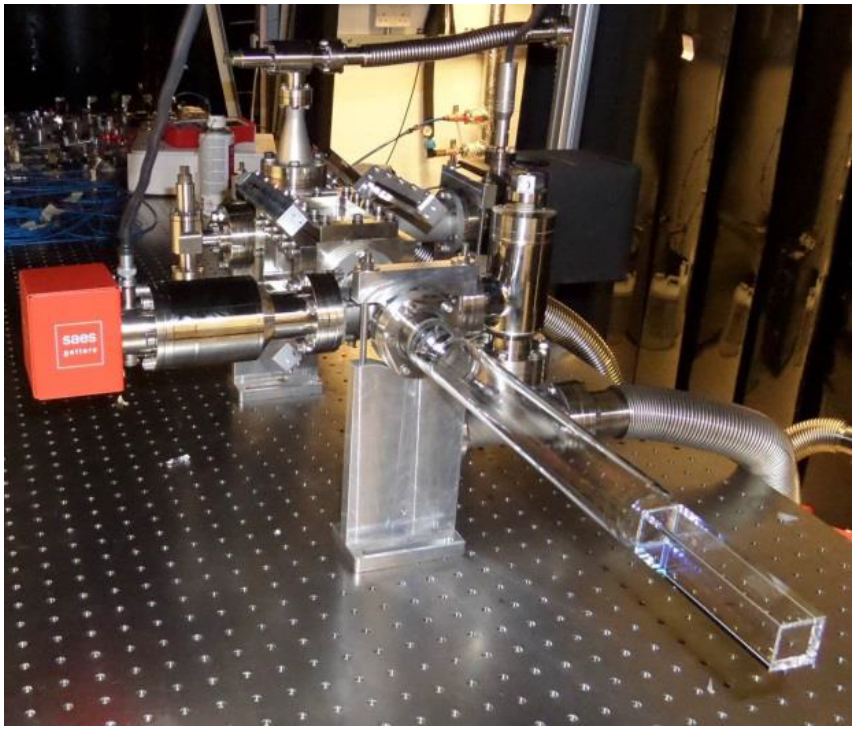


Figure 3.3: Detail of the vacuum setup when initially placed.

3.2 Laser system

Our laser system can be better understood if split into two parts. In the first part, I explain the laser system used to perform laser cooling that allows us to cool down the atoms from the room temperature to few tens of μK. The second part is devoted to the dipole trap laser system used for the trapping of the previously cooled atoms. These allow not only for the trapping but also for performing the evaporative cooling used to reach the ultracold regime. In section 4.1, I explain the experimental realization and the physics behind these cooling techniques. Although the laser system is similar to the one used in any other cold atoms experiments [82] we managed to fit all the components needed to cool down two different atomic species in a single optical table by using smaller optic components and fiber splitters as explained in the following.

3.2.1 Laser cooling system

In both MOTs for both species, we perform laser cooling by using the transitions in their respective D_2 lines. The different laser cooling techniques require of a closed atomic transition so that the atoms cycle between two levels meaning that the atoms are in their ground state, then excited to their excited stated and then, they decay to their original ground state. This allows for the cooling mechanism to be repeated every cycle leading to a reduction in temperature of the sample. However, there is not a perfect closed transition in our atomic species. Thus, we need a cooling laser addressing the transition that is closest to the ideal closed transition and a repumper laser that puts back in the cycle the atoms that fall out of it. Figures 3.4 and 3.5 show the structure of the atomic levels of the D_2 line of ^{87}Rb and $^{39-41}$K, respectively. In both figure ω_{cool} and ω_{rep} denote the frequency of the cooling and repumper lasers, respectively while Δ_{cool} and Δ_{rep} are their corresponding detunings. The cooling laser addresses the $|F = 2\rangle \rightarrow |F' = 3\rangle$ transition which are the ground and excited levels involved in the cooling cycle. In both cases there is a non-zero probability of an atom to be excited from the $|F = 2\rangle$ to $|F' = 2\rangle$ and then decaying to $|F = 1\rangle$, which is out of the cooling cycle. To solve this, we use the repumper laser addressing the $|F = 1\rangle \rightarrow |F' = 2\rangle$ transition. As shown in figure 3.5, the levels in the excited manifold are very close in the K case. In fact, they are not resolved as the frequency difference between these levels is a few MHz, being in the order of the natural linewidth of the D_2 line, Γ_{K}. In contrast, this does not happen in the Rb case, with a difference of hundreds of MHz. Consequently, the roles of the cooling and repumper light are not clearly delimited in the K case. Because of this, the repumper can exert force in the atoms.

To clarify, the cooling transition is $|F = 2\rangle \rightarrow |F' = 3\rangle$, in the case of each atomic specie this translates into $\left|4s^2S_{1/2}, F = 2\right\rangle \rightarrow \left|4p^2P_{3/2}, F = 3\right\rangle$ and $\left|5s^2S_{1/2}, F = 2\right\rangle \rightarrow \left|5p^2P_{3/2}, F = 3\right\rangle$ for K and Rb, respectively. For the K and Rb the repumper addresses the $|F = 1\rangle \rightarrow |F' = 2\rangle$ transition, which translates as $\left|4s^2S_{1/2}, F = 1\right\rangle \rightarrow \left|4p^2P_{3/2}, F = 2\right\rangle$

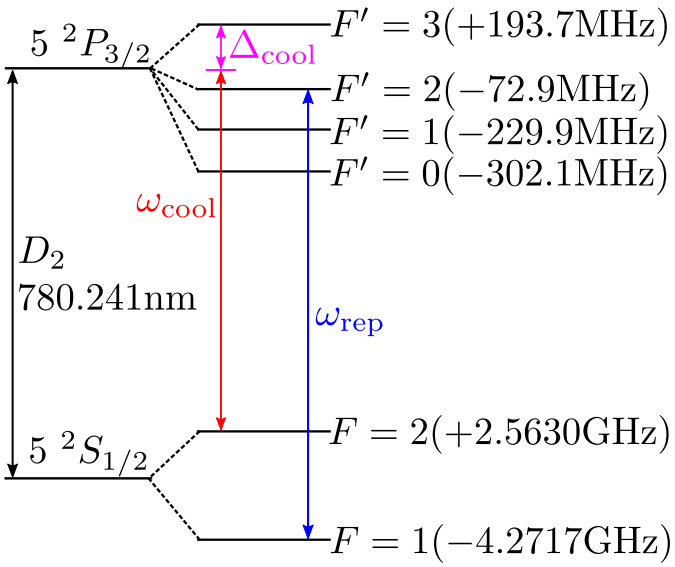


Figure 3.4: Structure of the atomic levels of the D_2 line of ^{87}Rb where the frequency difference between the hyperfine levels and their corresponding fine levels is denoted between brackets. ω_{cool} and ω_{rep} denote the frequency of the cooling and rempumper lasers, respectively. Δ_{cool} is the detuning between the cooling laser and the cooling transition.

and $\left|5s^2S_{1/2}, F = 1\right\rangle \rightarrow \left|5p^2P_{3/2}, F = 2\right\rangle$, respectively.

Laser cooling requires that the lasers' frequencies address the required transitions, and they have to be stable in the long term and tunable. To stabilize the frequencies, we use two different techniques. The first one is Doppler-free saturated absorption spectroscopy [84]. This technique uses an atomic transition as a reference, the signal obtained is a peak shaped signal. However, we require a signal with a zero crossing to use a proportional-integral-differential (PID) circuit to lock the frequency to the right point. In order to obtain the desired signal we use a fast modulation on top of the scanning signal to obtain the derivative of the signal by phase modulation. The PID circuit is in-build in the laser controller (TOPTICA DLC pro). The second technique is known as sideband offset locking [85]. This method requires a master laser, which is used as a reference to lock a slave laser using the beating between both frequencies as the locking signal. Similarly to saturated absorption spectroscopy, we use a PID circuit to lock to the desired frequency.

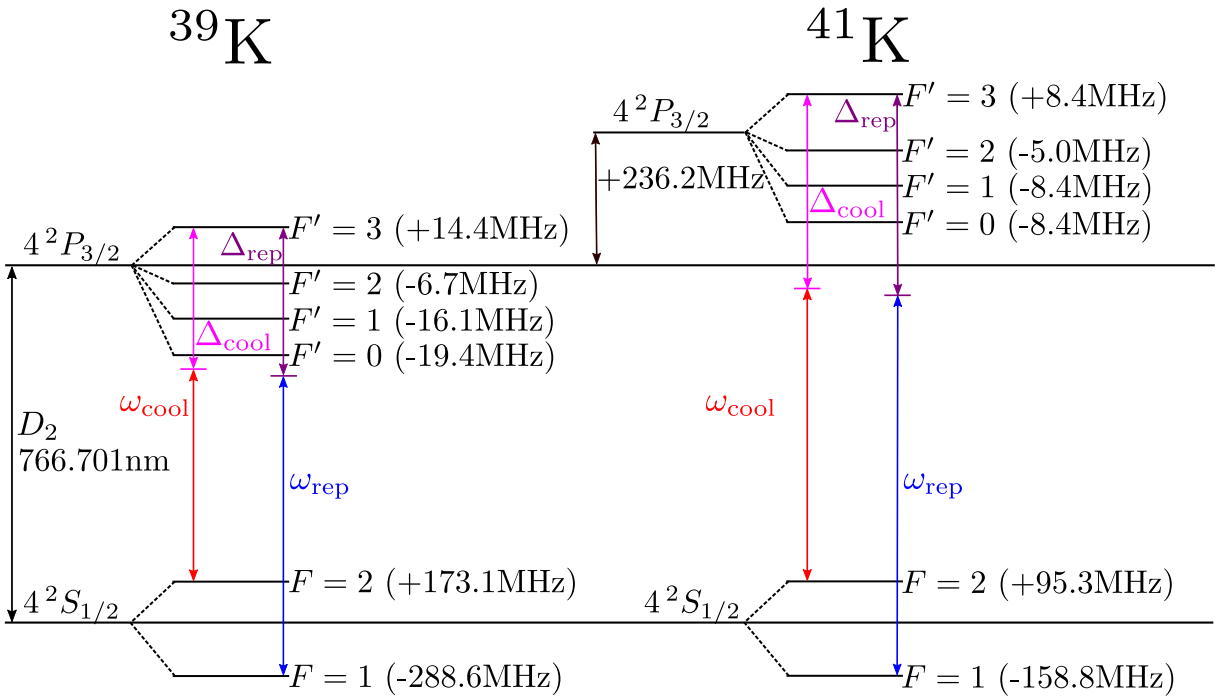


Figure 3.5: D_2 line for ^{39}K and ^{41}K. [83] ω_{cool} and ω_{rep} denote the frequency of the cooling and rempumper lasers, respectively. Δ_{cool} Δ_{rep} are the detuning between the cooling laser and the cooling transition, and the detuning between the repumper laser and the repumping transition, respectively.

3.2.1.1 Laser cooling layout

The laser layout I explain here is depicted in figure 3.7. In the following, I explain the system that I divided into four parts:

- In *K laser sources* we have the seed laser sources for the K, a Toptica DL PRO laser, and the required tapered amplifiers (TAs), model EYP-TPA-0765. These amplify the power of the seed lasers laser providing enough to perform laser cooling, around 1W each. There are two double-pass acousto-optic modulators (AOMs) used to shift the frequencies. We use the K cell to perform saturated absorption spectroscopy to lock the K laser. We send the resulting light to *K distribution* system via free space. In the case of K, the frequencies of the cooling and the repumping are close enough that they can be obtained by using AOMs from the same laser.

- In *K distribution* we have the laser distribution system for K. The light comes from *K laser sources* via free space. We use the three single-pass AOMs to control the intensity. The five fiber couplers are 1a, used for the imaging and the pushing beam, 2a, used for the 2D MOT light, and the last three, 3a, 4a, and 5a, used for the 3D MOT light.

- In *Rb laser sources*, we have 3 TAs, model EYP-TPA-0780, to amplify the light from the two New Focus Vortex lasers. In this case, we have a fiber collimator, denoted as *Rb master*, that provides the master laser light from an external module. This module contains a Rb cell used to lock the master laser by saturated absorption spectroscopy and it is placed on top of our experiment, it is not depicted here as it is equivalent to the one used in *K laser sources* to lock the K laser. This is then mixed with the light from the Vortex lasers that provide the cooling and repumper lights and sent to two different photodiodes (PDs) to generate the beat signal required to lock these two lasers using sideband offset locking.

- *Rb distribution* is similar to *K distribution* but it is used for the Rb light. We use different AOMs to control the frequency and the intensity of the laser beams. The five fiber couplers have the same function as those in *K distribution*.

To deliver the light to the atoms, we use a set of optical fiber splitters shown in figure 3.6. We use 2:2 fiber splitters to output the cooling and repumper for the 2D and 3D MOT. We use a polarization beam splitter (PBS) to mix both beams before the coupling. This type of fibers has two inputs and two outputs. In one of the inputs we couple the light corresponding to Rb, while we use the other input to couple the light for K. The light from each input is splitted and output evenly through both outputs. This means that the light from each output contains the light required to cool both species.

For the 2D MOT, we use a fiber splitter to deliver two light beams, both of which are collimated by two cylindrical lenses of focal distance 6 cm and 20 cm placed perpen-

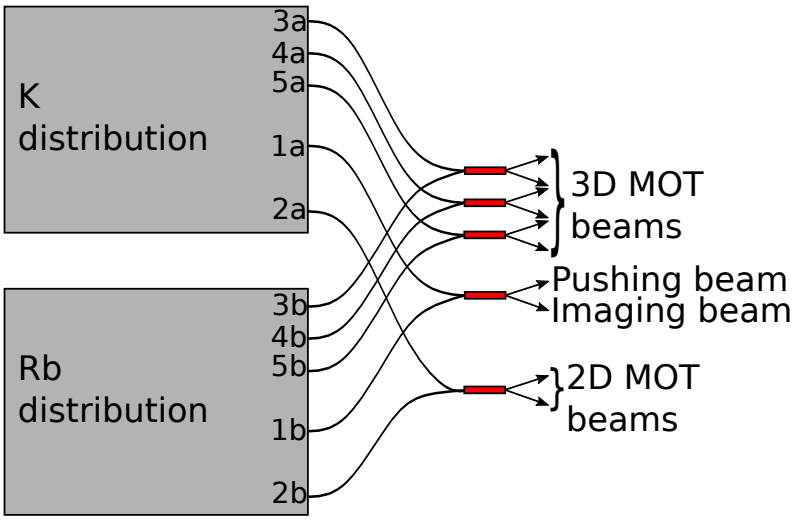


Figure 3.6: Schematics of the fiber splitters layout used to mix the laser cooling light for K and Rb. The numbers with letters denote the fiber couplers depicted in figure 3.7.

dicularly in respect to each other to achieve a elliptical beam size of 4×9 cm. To obtain the required circular polarization, we use two $\lambda/4$ waveplates. We counter-reflect both beams using prisms to keep the correct polarization on their way back. The prisms and the cylindrical lenses are rectangular and of the size to fit the whole elliptical beams.

Similarly, we use three fiber splitters in the 3D MOT to provide six beams. In this case, we use six lens tubes with $\lambda/4$ waveplates and 10 cm focal distance lenses to obtain a 25.4 mm beam size. We use the last fiber splitter for the pushing and imaging beams.

The cooling process requires balanced power for all the cooling beams. In the case of K, care must be taken to ensure that this is true for the repumper beams. As previously mentioned, the roles of the cooling and repumper are not that clearly defined in the case of K, so the repumper can act as the cooling beam and thus, the power of the beams has to be balanced so that the forces are balanced. The splitting ratio of the fiber splitters is polarization dependant, meaning that for the light to be evenly split, the polarization has to match the slow axis of the fiber. The problem we found was that when we use a PBS to mix the cooling and repumper lights, the resultant light beam contains both lights with perpendicular polarizations. Thus, we have to design the layout of *K distribution* accordingly. In particular, we used two PBSs in series, mixing all the cooling and repumper

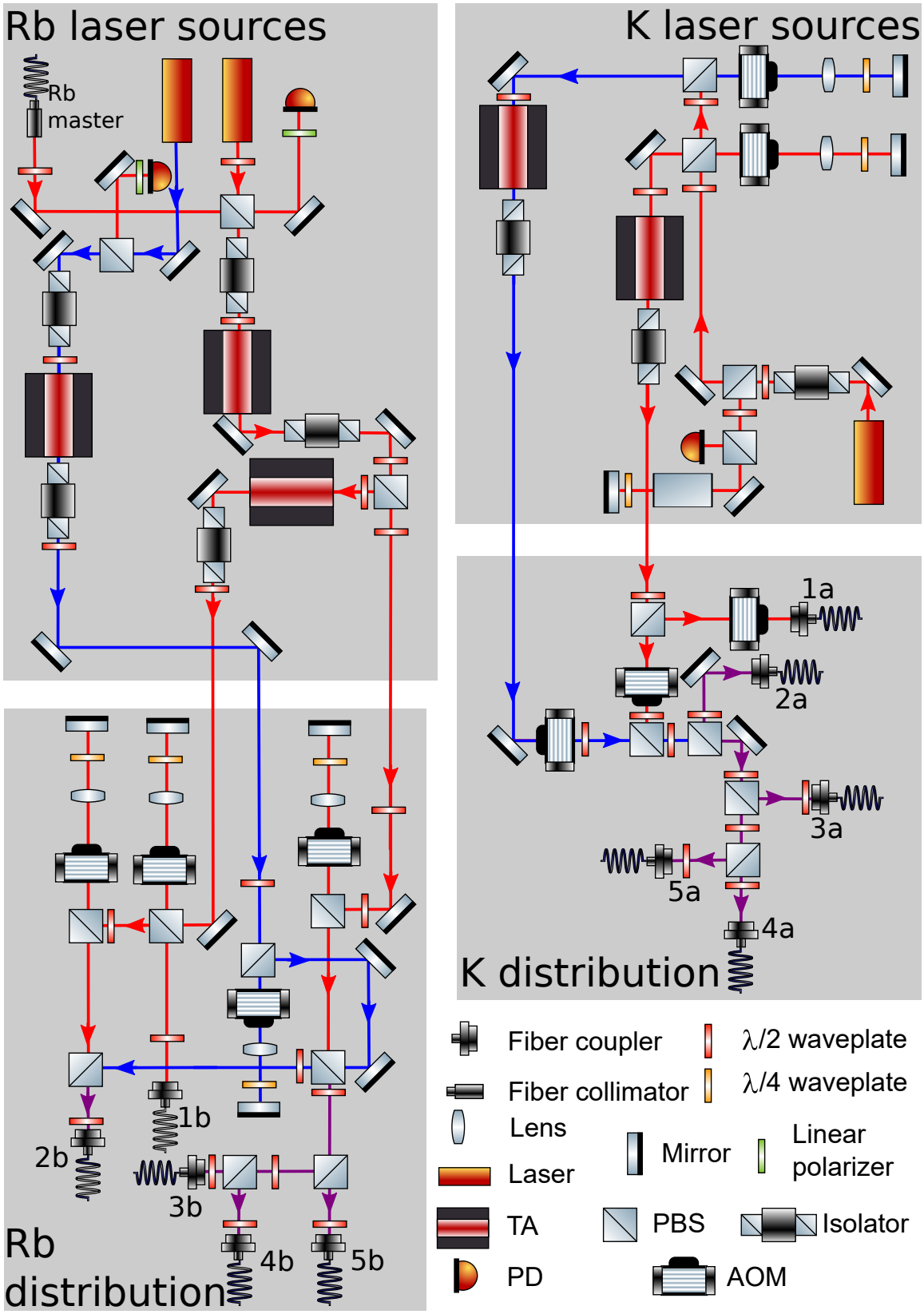


Figure 3.7: Schematics of the laser layout used for K and Rb laser cooling. Red beams represent the cooling light, blue ones the cooling light and purple the mixing of both.

light in the first one and splitting both components in the second one for the 2D and 3D MOTs.

The powers and detunings used when loading atoms in the MOTs are in table 3.1.

Table 3.1: Parameters of the lasers used during the loading of the MOT.

Laser	P_{cool} (mW)	Δ_{cool}	P_{rep} (mW)	Δ_{rep}
2D MOT Rb	80	-1.5 Γ_{Rb}	30	0
3D MOT Rb	80	-2.5 Γ_{Rb}	8	0
Pushing beam Rb	1	0	0	0
2D MOT K	100	-3 Γ_K	60	-2.5 Γ_K
3D MOT K	80	-3 Γ_K	40	-2.5 Γ_K
Pushing beam K	1.2	-1.5 Γ_K	0	0

3.2.2 Dipole trap system

The function of the dipole trap lasers in our experiment is to trap the atoms previously cooled by laser cooling. We use the dipole for the manipulation and the evaporative cooling of the atoms to the ultracold regime. This is explained in detail in section 4.1.4. Our dipole trap consists of two laser beams crossed in their waist, a design that is known as a crossed dipole trap. This trap design provides a better aspect ratio of the trapping frequencies than the one in single-beam traps in which the trapping frequency in the longitudinal direction is tens times smaller than in the radial direction. We use two lasers at different wavelengths in order to avoid any undesired interference effects. The first laser is a 1070 nm Ytterbium fiber laser (model YLR-20-AC-Y14), with a maximum output power of 20W. After all the optical elements, the maximum power is 11W with a beam waist of 36±1 μm in the dipole trap. The second one is a fiber amplified laser at 1550 nm (model NuAmp PSFA-1550-01-10W-2-1), with a maximum power of 8W. In the dipole trap the maximum power is 5W with a beam waist of 40±1 μm. We measured the waists using a knife edge mounted in a translational stage and a powermeter to get a graph of the power versus the position of the knife edge, we then fitted an error function to obtain the

waist. Figure 3.8 shows the optics layout for the dipole trap. In the following, I explain the layout for each of the dipole trap lasers.

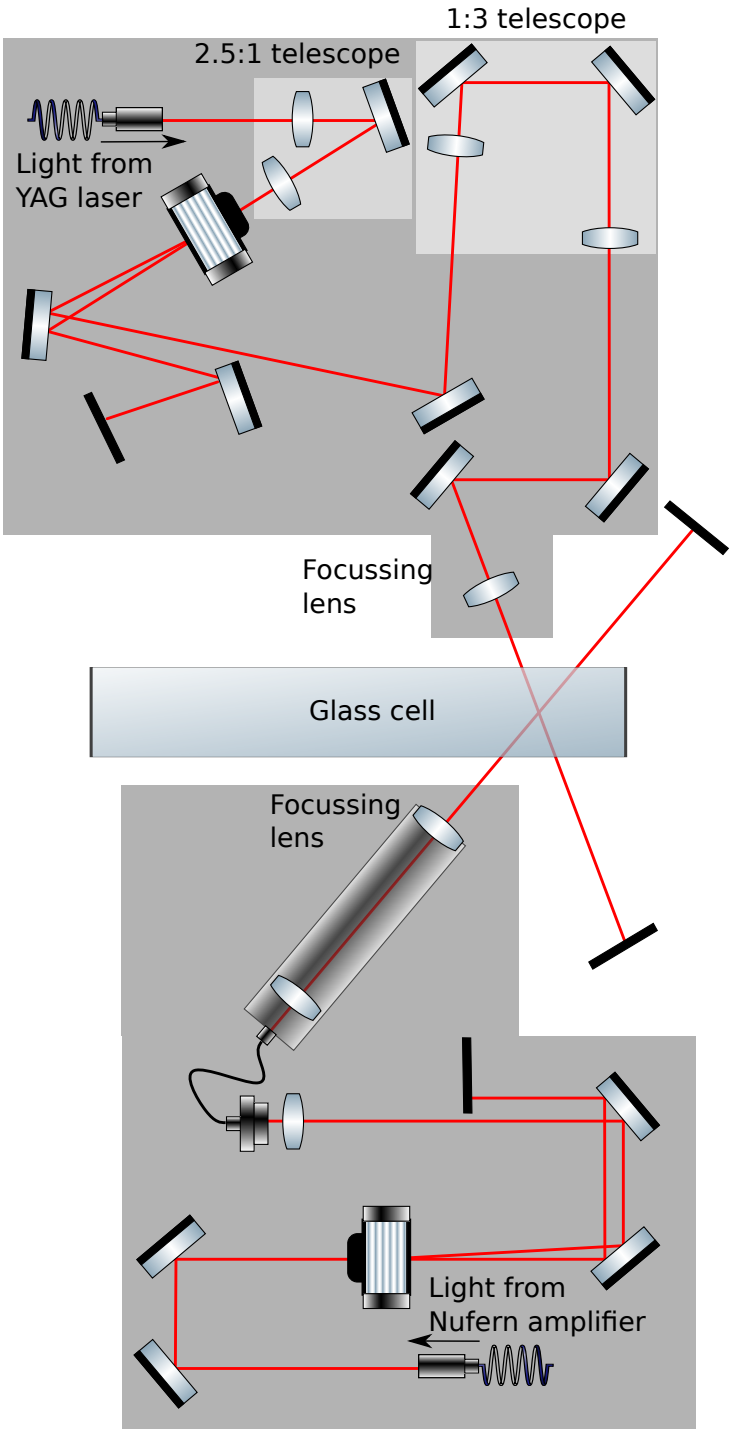


Figure 3.8: Schematics of the optic layout for both 1070 nm (top) and 1550 nm (bottom) dipole traps.

1070 nm: This laser delivers a continuous beam of unpolarized light. It has an integrated fiber output collimator that gives a beam size of 5 mm. A 2.5:1 telescope is used to reduce the beam size so that it fits the AOM aperture. The AOM is used to control the power of the laser beam. We use a D-shaped mirror to reflect the high power zero-order beam to a beam damp. The first order deflected beam goes through a 1:3 telescope that magnifies the beam before it is focused on the atoms in the μm regime, using a lens of 10 cm focal length to obtain the desired beam waist.

1550 nm: We use an ECDL laser diode (model Thorlabs SFL1550P) to seed a Nu-Fern fiber amplifier that output linearly polarized light. In this case, the output of the fiber collimator has the right beam size for the AOM aperture. The zero-order beam is also directed to beam damp. The first order beam is coupled to a high power optical fiber. We use a 3 cm focal distance lens to collimate the light from the fiber output that is then focused onto the atoms using a 17.5 cm focal distance lens. Both lenses and the optical fiber output are placed in a lens tube.

3.3 Optical tweezer

To build a single atom quantum engine, we require an optical tweezer to trap and manipulate a single atom. An optical tweezer is essentially a dipole trap with a very narrow waist (<2 μm). Due to the collisional blockade, we can achieve a regime in which we trap only a single atom. I explain this mechanism in detail in section 5.2. To achieve the desired beam waist, we use a long working distance microscope objective, in particular, the 10x magnification Mitutoyo Apochromatic Objective. This objective provides a beam waist below 2 μm and a working distance of 34 mm. Thanks to this, it can be placed outside of the glass cell and far enough to avoid blocking any of the other laser beams.

The optical tweezer setup is depicted in figure 3.9. The light source for the tweezer

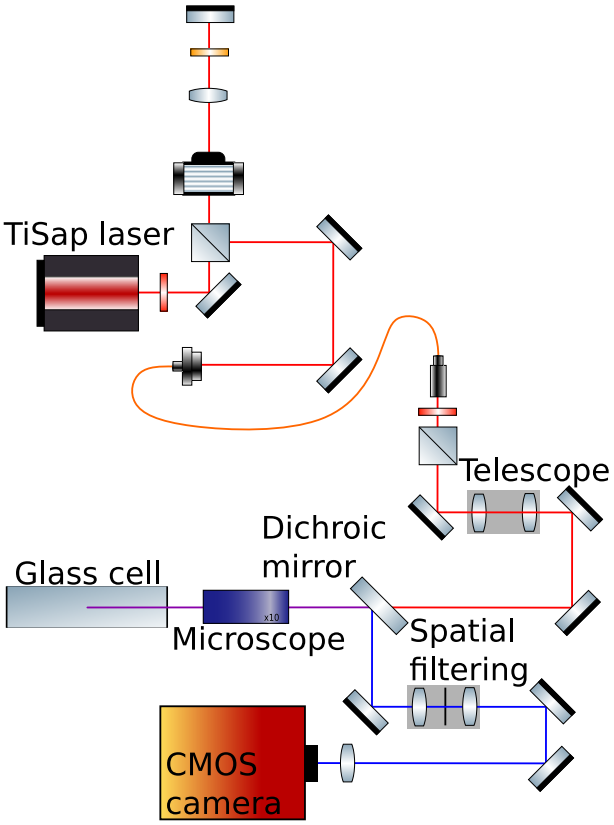


Figure 3.9: Schematics of the optic layout for the optical tweezer. The red path is the tweezer light, which is transmitted trough the dichroic mirror and the blue is the fluorescence light from the atoms, which is reflected by the dichroic. The purple path depicts the part in which the tweezer and fluorescence lights are overlapped. All light is actually red, the colors chosen are just used for depiction.

is a Ti:Sa (Titanium Sapphire) laser (model M-Squared SolsTis) which wavelength can be tuned from 600 nm to 900 nm. The pump laser used for it is a 532 nm laser (model Coherent Verdi) that outputs up to 12W. The maximum power the Ti:Sa laser provides for a 12 W input is 4 W when we set the wavelength at 789.82 nm. This is the magic wavelength for Rb, for which no Rb can be trapped, see section 5.2. However, this light can be used to trap K. A double-pass AOM allows for the control of the intensity of the tweezer beam (red) that is then coupled in a fiber, after which we use a PBS to clean the polarization of the light, as polarization fluctuations may affect the trapping potential. After this, a telescope is used to expand the beam size, so that we can achieve the required small waist. Then, the light is transmitted through a dichroic mirror, used to separate

the atoms' signal from the tweezer light. Finally, the tweezer beam is focused down into the glass cell using the microscope.

The fluorescence light from the atom trapped in the tweezer is collected and collimated by the microscope. The wavelength of this beam is 767 nm, which is reflected by the dichroic mirror. Then, this light goes through and subsequently spatially filtered using to lenses and a pinhole placed between them at the focal point. The first one focuses down the beam and the second one recollimates it. The function of the spatial filtering is to remove the reflections from the light beams used to induce the atom fluorescence since they are partially reflected into the microscope by the glass cell. Lastly, we focus the collected fluorescence light on a single pixel in a CMOS camera (model Hamamatsu ORCA C-14440). We placed a bandpass filter for the 767 nm light in the camera to avoid noise from the ambient and tweezer lights.

3.4 Imaging system

In the case of a cold atoms experiment, we sample the cloud of cooled atoms by imaging it. We use two different cameras for this purpose, one (model Allied Vision Guppy PRO F-031) records images across the horizontal axis, and the other one does it across the vertical direction (model Allied Vision Mako G-040). The horizontal camera pixel size is 5.6 mum and 6.9 μm in the vertical case. This pixel size is ideal since the size of the atomic samples ranges from few mm to tens of μm requiring only a simple telescope to image the atoms. We connect both cameras to the so-called imaging computer through a software interface named *acquire*, and the acquired data is analyzed in the same computer by a different software called *cam strip down*.

The optical layout for the horizontal and vertical imaging systems is shown in figure 3.10. In the horizontal system, we use a lens to demagnify the image by a factor 3, while

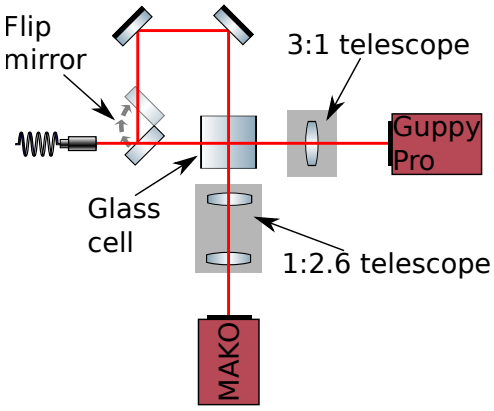


Figure 3.10: Schematics of the imaging system.

in the vertical direction, a telescope system magnifies it by a factor 2.6. In the horizontal imaging, we can see the whole atom cloud trapped in the MOT, while the BEC is just a few pixels in this imaging system.

To image properly the BEC we use the vertical imaging, which has a bigger magnification. Moreover, the vertical orientation allow to image the atoms for different times of flight as they fall. In both imaging systems, the calculated diffraction limit is of the order of 5μm, which is smaller than the smaller atomic samples we image. In the worst case the depth of focus is 500 μm, this may be a problem in the vertical imaging system as the atoms fall in the axis of the imaging. The usual displacement is around 1 mm, to correct this we can essentially move the camera position to correct this. In conclusion, we are not really limited by our imaging system. A flip mirror allows us to choose the path for the imaging beam so that we can perform absorption imaging in both directions depending on what we want to measure.

3.4.1 Imaging techniques

We use two different imaging techniques. These are fluorescence imaging and absorption imaging.

Fluorescence imaging This technique is based on the stimulation of the fluorescence of an atom. To do this, we briefly illuminate the atoms with cooling and repumper lights. Thus, the atoms are in the cooling cycle absorbing the photons from the laser that take the atom to the excited state and emitting them when it natural decays to the ground state. The emitted photons are then collected by a camera. The atom number, N, is related with the number of emitted photons, N_{ph}, via the scattering ratio, R_{sc}, given by the following expression [49],

$$R_{sc} = \frac{N_{ph}}{N} = \frac{\Gamma}{2} \frac{I/I_s}{1 + \frac{I}{I_s} + 4\frac{\Delta^2}{\Gamma^2}}. \tag{3.1}$$

Where Γ is the natural linewidth of the transition, I is the intensity, I_s is the saturation intensity, and Δ is the detuning of laser frequency with respect to the frequency of the transition. N_{ph} is measured experimentally. Using this technique in the horizontal imaging system, we are to image samples as low as $\sim 10^6$ atoms contain in a volume of ~ 1 cm^3.

Absorption imaging To perform absorption imaging, we take advantage of the atoms absorbing light close to the atomic transition frequency. Thus, we measure the intensity profile of a laser traveling through the science chamber with, I_f, and without the atoms, I_0. We also measure the background light, I_b. From these intensity profiles, we can calculate the optical density, OD,

$$\text{OD} = -\log\left(\frac{I_f - I_b}{I_0 - I_b}\right). \tag{3.2}$$

To relate this amount with the number of atoms, we use Beer's Law. If every pixel has an effective area, A, the total number of atoms, N, is

$$N = \frac{A}{\sigma_{\text{abs}}} \sum_{i}^{\text{pixels}} OD_i, \tag{3.3}$$

where σ_{abs} is the absorption cross-section given by the following expression [49]:

$$\sigma_{\text{abs}} = \frac{6\pi c^2}{\omega_0^2 \alpha} \frac{1}{1 + 4\Delta^2/\Gamma^2 + I/I_s}, \tag{3.4}$$

where ω_0 is the frequency of the transition and α is the absorption coefficient. Thus, the total number of atoms is given by the following expression:

$$N = \frac{A\omega_0^2 \alpha}{6\pi c^2} \left(1 + 4\frac{\Delta^2}{\Gamma^2} + \frac{I}{I_s}\right) \underbrace{\sum_{i}^{\text{pixels}} OD_i}_{\dagger} \tag{3.5}$$

This expression gives us the total number of atoms. However, since we fit a distribution to the optical density profile we replace (†) by the integral of the the fitted distribution.

This technique destroys the atomic samples. Thus, there is a trade-off between the power used to image and the optical density one can measure. In terms of imaging ultra-cold samples, using the vertical imaging system, we are able to image samples of OD$\approx 2.5 with \sim 10^5$ atoms. This allows us for the imaging of the BEC.

Temperature determination The density profile of a thermal atomic sample can be fitted by a Gaussian profile [86]. The size of the cloud depends on the temperature and the expansion time. The expansion of the cloud follows the expression,

$$\sigma_{\text{TOF}}^2 = \sigma_0^2 + \frac{k_b T}{m} t^2, \tag{3.6}$$

where σ_{TOF} is the standard deviation of the cloud density profile after a certain time of flight, t, and σ_0 is the standard deviation of the cloud density profile at $t = 0$. Thus, we

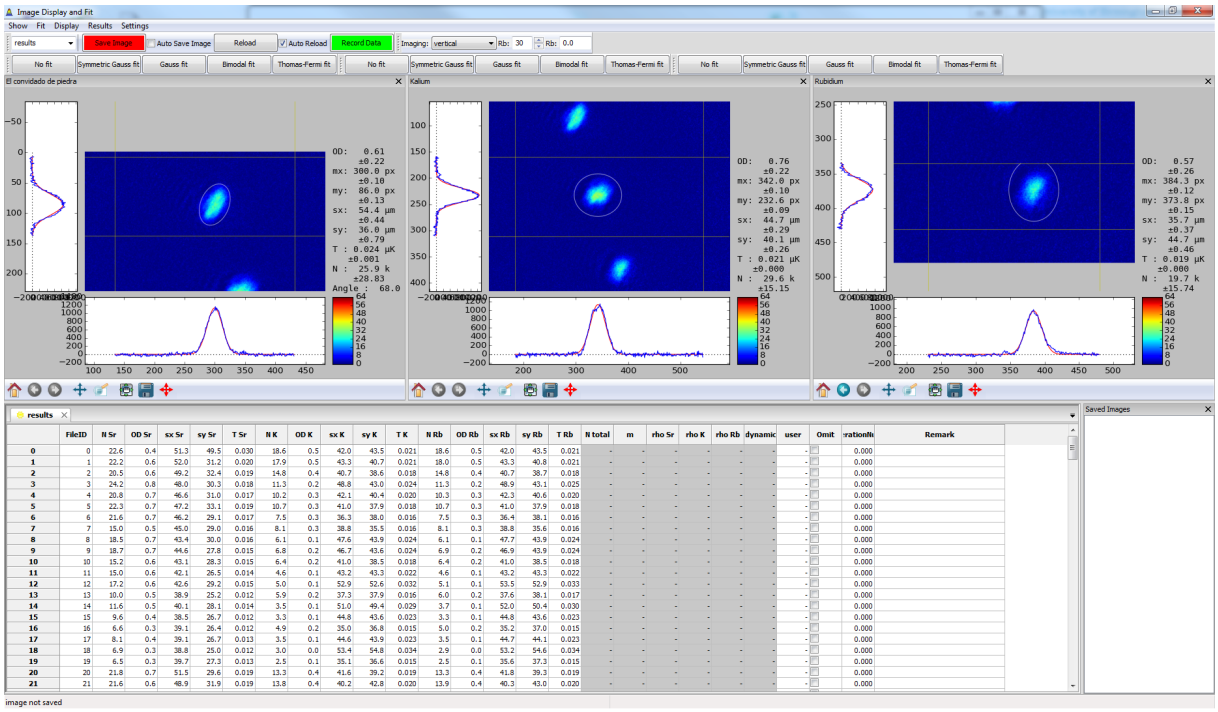


Figure 3.11: Screen-shot of *cam strip down*. The top 3 panels show different portions of the absorption image and display the fit results on the side, the bottom table contains the fit parameter that can be fitted "live" together with the value of the parameter we are scanning.

can fit a Gaussian profile to the atom cloud images to obtain the different values of σ_{TOF} and use the obtained values in a linear fit to determinate the temperature of the atomic sample using equation 3.6.

3.4.2 Acquisition software

The acquisition software is composed of two programs written in Python that we adapted to our system. The first one, called *acquire*, controls the camera and outputs the images taken by the camera. The second one, called *cam strip down*, reads the pictures saved by *acquire* and has in-built functionalities for the fitting of the optical density profiles for different cases, such as Gaussian fit for a thermal cloud or Thomas-Fermi for a BEC.

Figure 3.11 shows a screenshot of this program for the case of a Stern-Gerlach ex-

periment for an ^{87}Rb BEC in $|F = 1\rangle$. In this case, we have three clouds corresponding to the magnetic sublevels, $m_f = -1, 0, 1$. The program has the capability of fitting the atomic distribution for the three clouds and calculating different magnitudes such as the number of atoms and temperature.

3.5 Control system

In this section, I explain the computer control, including the hardware and software used to control the experiment. In our experiment, we require a control system with a time resolution of $1\mu s$. To achieve the required performance, we use PCI eXtensions for Instrumentation (PXI), which is a standard from National Instruments. In our case, the components of the PXI are compatible with the standard DAQmx, which is the driver required by the software we use. Our PXI consists of four PXI cards installed in a chassis (model PXI-1042Q),

- One card PXI-8360, it is the one that connects the rest of the PXI with the computer that controls it.
- One card PXI-6533, this card has 32 digital channels that can output two voltage values, 0V or $3.6V$. The time resolution of this card is $0.1\mu s$
- Two cards PXI-6713, each of them has eight analog channels. These analog channels can output any voltage between -10V and 10V.

A Field Programmable Gate Array (FPGA), model Opal-Kelly XEM3001, provides the time reference. We use the FPGA as a variable frequency clock, meaning that it produces a clock signal which is used by the PXI. The FPGA changes the clock frequency for the different stages depending on the required time resolution for each stage of the

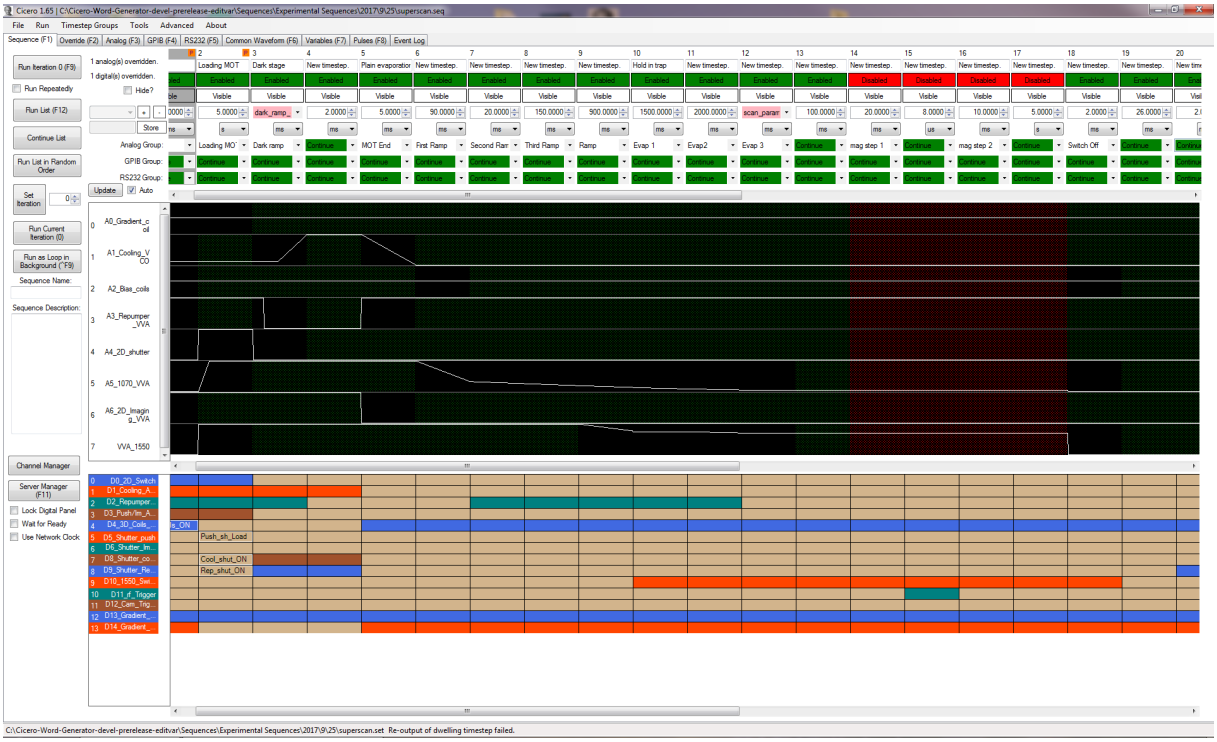


Figure 3.12: Screenshot of Cicero. The top panels show the different time slots for each stage, the middle panel shows the value of the analog channels along the sequence and the bottom one shows the digital channels.

experimental sequence. The variable time resolution reduces the requirement for in cards' memory, optimizing the capabilities of our control system.

The software we use in our control system is Cicero Word Generator [87], this software is written in C and used in the cold atoms experiments at MIT. It consists of two different programs, Atticus and Cicero. Atticus recognizes the hardware components and provides an interface to translate the instructions from Cicero to the hardware. Atticus essentially lists the hardware components and some options concerning them. Cicero is the program used to design the different experimental sequences and to run the experiment. Both programs communicate via .NET Framework v2.0. In figure 3.12, I show a screenshot of Cicero, in which we have sequence loaded where we can see the different time slots for the stages of the experimental sequence at the top. Under these slots, we have the signals of the analog channels and the digital channels' control at the bottom.

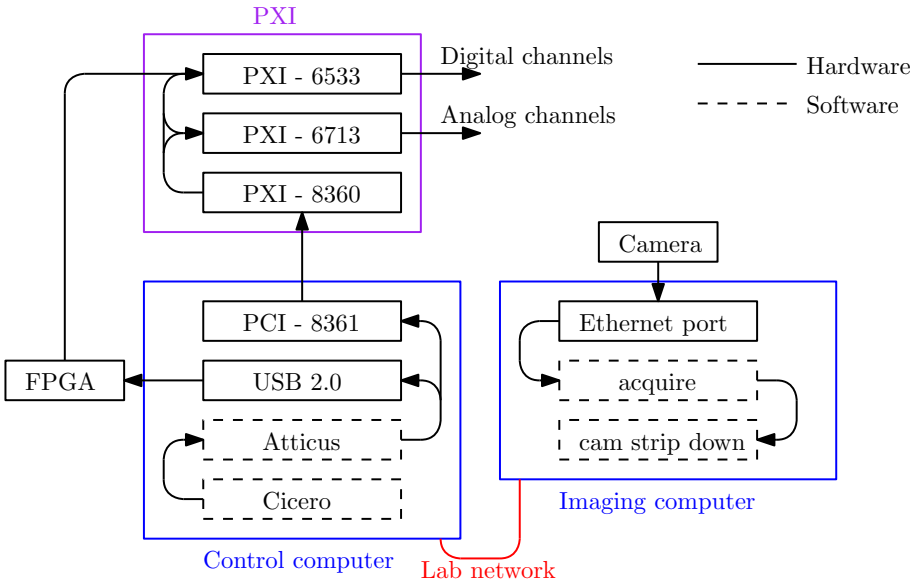


Figure 3.13: Schematics of the control system for our experiment.

In figure 3.13, I present a scheme of the whole control system together with the imaging system. When we run an experimental sequence, Cicero generates the instructions that are translated and sent by Atticus to the FPGA, connected via USB to the computer, and the PXI via the D-sub cable that connects the PXI-8360 card with the dedicated PCI card (model PCI-8361) installed in the computer. While the PXI runs the sequence, it uses the reference clock provided by the FPGA. The clock signal is provided by an SMA cable that connects the FPGA with the appropriate port in the breakout board of the PXI-6533 card. The same breakout board and the corresponding for the other cards contain all the input and output ports of the cards. These breakout boards also have the appropriate current buffers used by the channels' output. These allow us to control some of the electronic devices that require a control current higher than the one provided directly by the PXI cards. The imaging and control computers are connected through the lab network so that the control computer can send the parameters of the sequence to the imaging computer to storage it together with the data acquired by the camera. This setup can achieve a time resolution of 1μs for a sequence of 1min using a computer with 4GB of RAM [87].

Chapter 4

Non-equilibrium quantum thermodynamics in a ^{87}Rb-^{39}K mixture

In this chapter, I explain the experimental realization of the BEC transition in a dissipative environment that led to the creation of out-of-equilibrium supercritical BEC samples by dissipative distillation. This was the starting point of the study of NEQT, exploiting the ^{87}Rb BEC in conjunction with a ^{39}K MOT. The chapter is divided into the following sections:

- **Section 4.1** explains the realization of an all-optical ^{87}Rb BEC in our setup. This includes the laser cooling of the ^{87}Rb atoms from room temperature to the BEC state and its characterization.

- In **section 4.2** I explain the techniques used to cool ^{39}K in the MOT and some preliminary results of ^{39}K trapping in the dipole trap.

- Section **section 4.3** contains the results of the supercritical ^{87}Rb BEC that we achieved by immersing it in the ^{39}K MOT. I describe as well the phenomenological model that we developed to understand the obtained results.

- Finally, in **section 4.4** I explain the mechanism behind the dissipation and how the dissipative environment was realized experimentally.

The last two sections of this chapter contain a partial reproduction of my first author publication found in reference [42]. I built the experiment, took the data, collaborated in the data analysis and in the writing the manuscript of the cited publication.

4.1 Realizing an all-optical ^{87}Rb BEC in our setup

The first milestone of this experiment was the realization of an all-optical ^{87}Rb BEC. To achieve this, we firstly cool down the atoms from room temperature to a few tens of μK using laser cooling. The laser cooling setup is explained in section 3.2. Then these cold atoms are loaded in the dipole trap and further cooled by evaporative cooling. The advantage of an all-optical BEC experimental setup is that it does not require coils carrying the high current needed to perform magnetic RF evaporation. Usually, that type of coils require active cooling, thus increasing the size and complexity of the system. Another advantage is that the magnetic sublevels, m_f, are degenerated in the absence of a magnetic field, allowing for the atoms in any magnetic sublevel to be cooled to the BEC state. That makes possible the study of richer systems such as spinor BEC or the effects of synthetic magnetization [88].

4.1.1 Experimental sequence

The experimental sequence used to obtain ^{87}Rb BEC is depicted in figure 4.1. We start the sequence by loading the 3D MOT using the stream of cold atoms generated in the 2D MOT. The atoms are pushed from the 2D to the 3D MOT by the pushing beam. The 3D MOT saturates in 3s after which, we switch off the lights from the 2D MOT and the

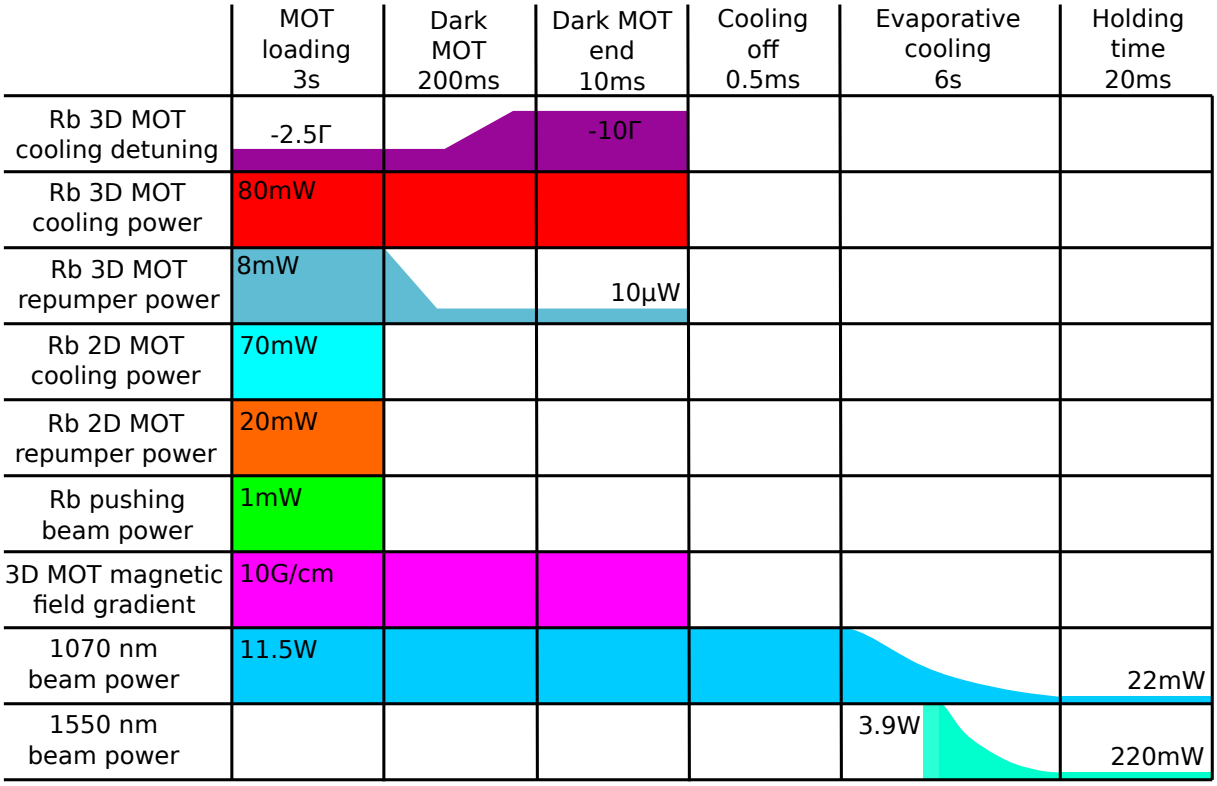


Figure 4.1: Experimental sequence used to obtain a ^{87}Rb BEC.

pushing beam. After this, we obtain $\sim 10^9$ atoms at $\sim 300\mu$K. The 1070nm dipole trap beam is switch ON full power at this stage.

The next stage is to cool down the atoms below the Doppler limit by using a temporal dark MOT stage as explained in section 4.1.3, reaching 50μK. We found that keeping the final values of the dark MOT stage for 10 ms longer improves the loading into the dipole trap. After this, we switch off all the cooling lights and the magnetic field gradient, and we start the evaporation first by reducing the power of the 1070nm dipole trap beam and later in both traps in different stages using the values specified in table 4.1.

Finally, we hold the atoms in the dipole trap using the last parameters of the evaporation for 20ms allowing for the final rethermalization before we release them. In the following, I explain in more details the different stages of the cooling process.

Table 4.1: Dipole traps power at the beginning of each stage of the evaporative cooling.

Stage	1550nm power (W)	1070nm power (W)	Time (ms)
Ramp 1	0	11.5	100
Ramp 2	0	5.18	200
Ramp 3	0	4.88	600
Ramp 4	3.90	2.55	500
Ramp 5	3.90	1.50	1000
Ramp 6	0.68	0.24	2000
Ramp 7	0.345	0.073	2100
Final	0.220	0.022	N/A

4.1.2 Loading Rb atoms into the 3D MOT

The cooling process starts in the 2D MOT that confines the atoms in two dimensions where they are cooled by Doppler cooling (see section 2.1.2.1) producing a cold and dense flux of atoms of $\sim 10^9$atoms/s, with a speed of ~ 10 m/s. The stream of atoms is propelled by the pushing beam. The resultant stream of atoms obtained in the 2D MOT is then loaded in the 3D MOT, which cools and confines the atoms in three dimensions. Typical values for the 3D MOT are $\sim 5 \cdot 10^9$ atoms at $\sim 300\mu$K which are loaded in ~ 3s. The combination of a 2D MOT with a 3D MOT allows for the quick and robust loading of atoms in the 3D MOT [89].

In both MOTs, we perform Doppler cooling by using the transitions in the D_2 line. As explained in section 3.2.1, we require a cooling and a repumper laser. Trapping the atoms in the MOT by the quadrupole magnetic field requires the correct circular polarization of the MOT beams in order to interact with the appropriate m_f sublevels.

The typical values for cooling detuning, Δ_{cool}, are -2.5Γ and -1.5Γ for the 3D and 2D respectively, where Γ is the natural linewidth of the D_2 line of Rb. The repumper is set in resonance with the repumper transition. The pushing beam is set in resonance with the cooling transition. The powers of the combine beams are specified in figure 4.1. The magnetic gradient in both MOTs is 10 G/cm.

4.1.3 Rb dark MOT

The idea behind our Rb dark MOT is known as temporal dark MOT and it has been widely studied [90, 91]. In this technique, the repumper light power is reduced. Thus, the atoms fall out the cooling cycle and are "shelved" in a dark state, $|F = 1\rangle$, in which they avoid strong interaction with the cooling light meaning a reduction in rescattered radiation and excited state collisions. The result of this process is an increase in atom density and a reduction of temperature. The fact that the atoms are contained in a smaller volume closer to the minimum of the magnetic field also helps other cooling mechanism such as gradient polarization cooling.

In practice, we ramp down the total power of the repumper beams from ~ 5 mW to ~ 10 μW in 50 ms and we detune the cooling light from Δ_{cool} = -2.5 Γ to $\Delta_{\text{cool}} = -10\Gamma$ in 150 ms. The change of the detuning is used to address the hotter atoms since they require a larger red detuning due to their larger Doppler shift. This ultimately reduces the temperature from 300 μK to 50 μK. The final temperature is below the Doppler limit, T_D=146 μK.

One may ask why we do not use optical molasses, which can cool down the atoms to the same temperature. The reason for this is that we found the dark MOT to be more efficient and robust as the optical molasses do not provide adequate spatial confinement of the atomic sample, which is crucial to trap the atoms in the dipole trap.

4.1.4 Evaporative cooling

We use all-optical evaporation to reach the BEC regime. This technique is explained in section 2.1.2.2. We use a crossed dipole trap to trap the atoms from the dark MOT. The crossed dipole trap setup is described in section 3.2.2. In our particular case, for an alkali atom with linear polarized or unpolarized light, the dipole trap potential, U_d, is given by

the following expression [58],

$$U_d(\mathbf{r}) = \frac{\pi c^2 \Gamma}{2} \left(\frac{2}{\omega_2^3 \Delta_{2,F}} + \frac{1}{\omega_1^3 \Delta_{1,F}} \right) I(\mathbf{r}), \tag{4.1}$$

where ω_0 is the laser frequency, and $\Delta_{2,F}$ and $\Delta_{1,F}$ are the detuning of the laser with respect to the D_2 and D_1 lines. For a laser red detuned with respect to both spectral lines, $\mathrm{Re}(\alpha) > 0$, which means that the minimum of the potential is located in the maximum of intensity. Considering that the intensity profile of the trap beams is Gaussian, atoms can be trapped in the focus of the laser beams where the intensity is maximum. Once they are trapped, we perform evaporative cooling by reducing the power of the dipole trap lasers to allow the hottest atoms to escape as the trap depth decreases. As explained in section 2.1.2.2, this has to be done slowly enough so that the atoms that remain in the trap have enough time to rethermalize.

4.1.5 ^{87}Rb BEC characterization

To characterize the BEC we meassured the critical temperature, T_c, and the trapping frequencies, ω_1, ω_2 and ω_3. To find T_c experimentally, we use equation 2.14, replacing by its definition found in equation 2.11, obtaining:

$$N_0 = \max \left[N - \left(\frac{k_B T}{0.94 \hbar \bar{\omega}} \right)^3, 0 \right]. \tag{4.2}$$

Now, we consider the relation between the potential and the trapping potential found in [58],

$$\omega_i = \sqrt{\frac{2\hat{U}}{m w_i^2}}, \tag{4.3}$$

where $\hat{U}$ is the first order term of the Taylor expansion of the trapping potential in the direction of the trapping frequency, m is the atom mass and w_i the beam waist. $\hat{U}$ it

is proportional to the temperature, since the trap depth defines the temperature of the atoms. In fact, we assumed this and tested it experimentally in our case. We only used this as a quick test to check that the condensation was working as expected. Thus, we can write $\bar{\omega} = \beta T^{1/2}$, where β is a constant. Thus, equation 4.2 can be rewritten as,

$$N_0 = \max\left[N - \left(\frac{k_B T}{0.94\hbar\beta T^{1/2}}\right)^3, 0\right] = \max\left[N - \alpha T^{3/2}, 0\right], \tag{4.4}$$

where $\alpha = [k_B/(0.94\hbar\beta)]^3$. We can use the previous equation to fit the experimental data obtaining T_c, which is the point in which $N_0 > 0$. In that point, we can measure directly the trapping frequencies to check that the magnitudes of our system are right.

The way we measure the trapping frequencies in our system is parametric heating. This technique relies on modulating the power of the dipole trap with a certain frequency, ω_m. When $\omega_m \approx 2\omega_i$, the modulation introduces energy in the system, heating it and depleting the atoms from the trap. Thus, we can observe a resonant like behaviour when we look at the temperature of the atoms as a function of ω_m. In figure 4.2, I report the cloud size which is proportional to the temperature versus ω_m, we can observe three different peaks corresponding to the three trapping frequencies. I fitted the sum of three Lorentzian functions to obtain the three trapping frequencies. The results of the fit are $\omega_i = (60.2 \pm 0.4, 91 \pm 1, 128 \pm 2)$ Hz.

However, the effects of anharmonicity, due to the trap being only perfectly harmonic in the center, cause the measured frequencies to be shifted with respect to the calculated values [92]. In our case, we use the real values calibrated to take into account this. In appendix A I provide a further discussion of this as well as the comparison between the real and calculated values. The potential at the end of the evaporation can be calculated using the experimental parameters in equation 4.1.

In figure 4.3, I show the 2D optical density profiles for the ^{87}Rb cloud after 20 ms time of flight, for different temperatures across the phase transition. As soon as $T < T_c$,

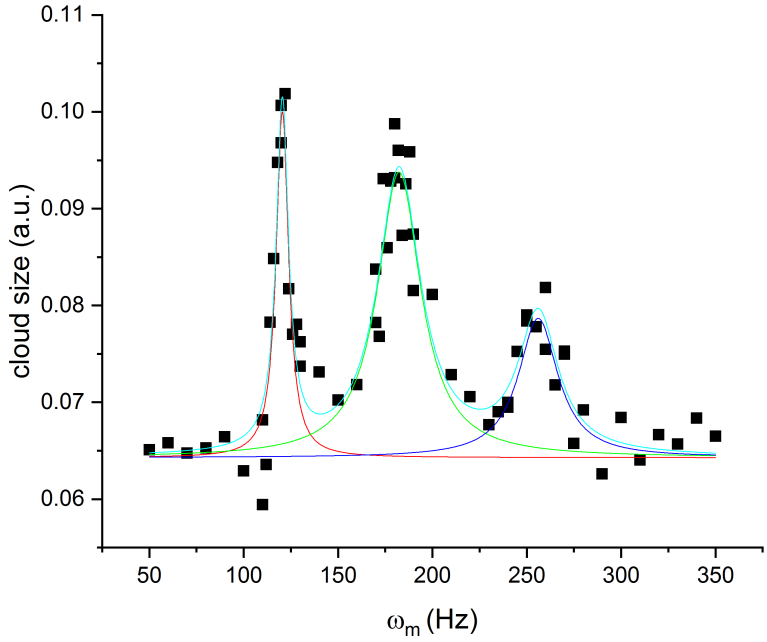


Figure 4.2: Cloud size versus the modulation frequency of the dipole trap.

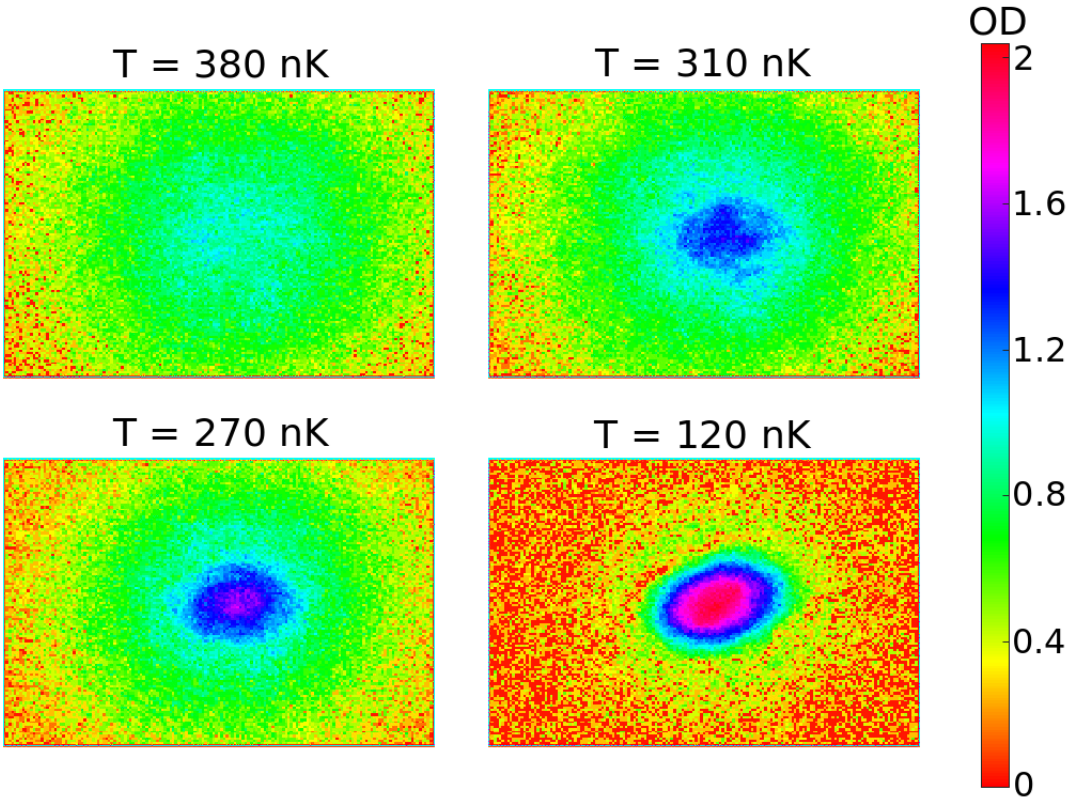


Figure 4.3: Optical density profiles obtained by absorption imaging for the ^{87}Rb cloud at different stages of the evaporation for 20 ms of expansion time. The approximate size of each image is 90×120 μm.

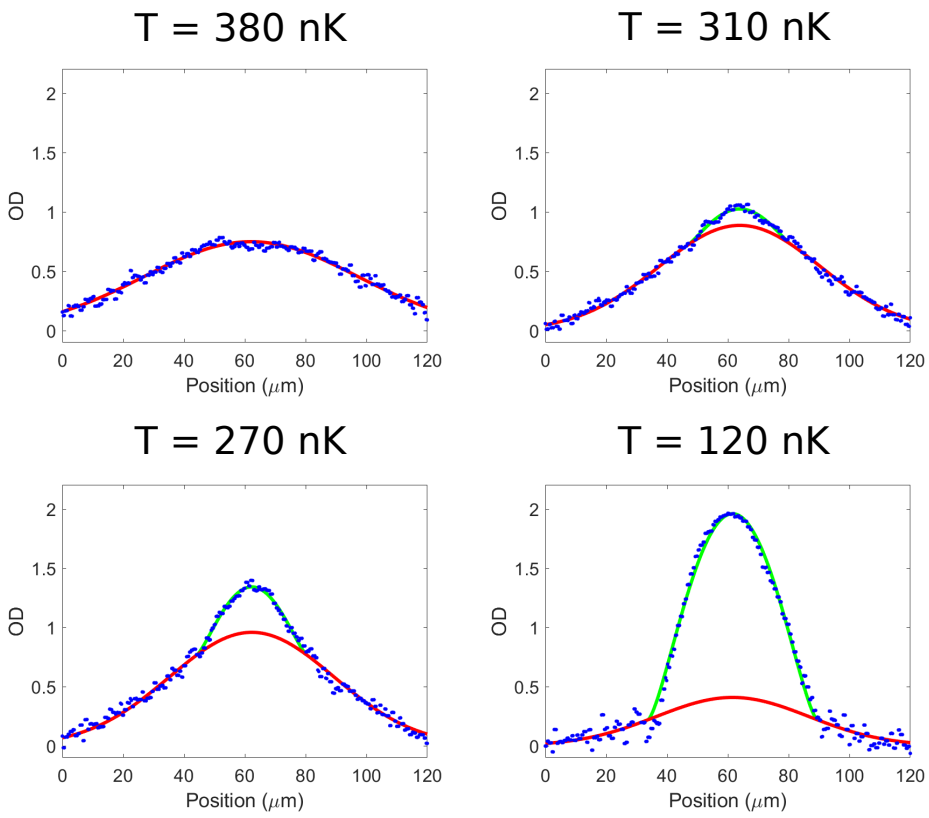


Figure 4.4: Optical density across the horizontal axis for the 2D profiles shown in figure 4.3. The blue dots are the data, the green lines represent the Thomas-Fermi distribution corresponding to the BEC component and the red lines represents the Gaussian distribution corresponding to the thermal component.

which is $T_c \approx 350$ nK, the optical density profile changes from a thermal distribution to a bimodal. This can be clearly seen in figure 4.4, where I have plotted a transversal cut of the previous figure across the horizontal dimension. The bimodal distribution is the sum of a Thomas-Fermi distribution that describes the BEC and the Gaussian describing the thermal component. We can observe in figure 4.3 how the BEC component is asymmetric, this is another signature of the BEC, and it is due to how the BEC component expands when released. Finally, when no thermal component is left, the distribution is simply a Thomas-Fermi one.

4.2 Cooling and trapping of K

Our apparatus was designed with the purpose of trapping a single ^{41}K atom in a bath of ultracold ^{87}Rb, as this is required for the realization of the single-atom quantum engine (see chapter 5). The ultracold bath of ^{87}Rb is already within our reach since, as explained in the previous section, we are even able to reach the BEC regime. To trap a single atom, we plan to use an optical tweezer, explained in section 5.2. In order for the atom to be trapped in the optical tweezer, we need to cool down the ^{41}K. Similarly to the case of ^{87}Rb, we use the MOT and other laser cooling techniques to trap and cool down the atoms. These techniques are explained in sections 4.2.1 and 4.1.3, respectively. As the MOTs of both species were (and are) overlapped and the dipole trap lasers are far-red detuned with respect to the D_1 and D_2 transitions of both species, we were in the position of trapping both atomic species in the dipole trap. In principle, this should have allowed us for the evaporative cooling of ^{41}K to the BEC regime and the consequent realization of a two-species all-optical BEC, a system that has not been previously realized. This system is of interest because it would combine the rich physics of all-optical BECs with the phenomena of two species BECs [93].

However, we were not able to trap enough ^{41}K atoms in the dipole trap. After this, and considering that ^{39}K is ten times more abundant in the atom source used in the experiment and that it can be cooled further down using optical molasses in the D_2 line [94], we decided to change our laser system to cool ^{39}K instead. Doing this only involved the change of the order used for some of the AOMs due to the small frequency difference between the cooling and repumper transitions of both K isotopes. Nevertheless, we were not able to load enough atoms in the dipole trap to start the evaporation since we lost all of them in few hundreds of ms after they were loaded, way before the BEC regime. In section 4.2.3 I explain this phenomenon.

As we only obtained a good enough signal from the atoms in the dipole trap for ^{39}K,

this section is limited to it. This species is also used for the realization of the BEC in a dissipative environment. More details about the cooling of ^{41}K can be found in section 5.2.4.

4.2.1 K MOT and dark MOT

Similarly to the cooling of ^{87}Rb we use the same cooling and repumper transitions to obtain a closed cooling cycle in the D_2 line that allows for Doppler cooling. As explained in section 3.2.1, the roles of the cooling and repumper light are not clearly delimited in the K case, the repumper needs to be detuned. Because of this, the most efficient cooling of ^{39}K in the MOT is achieved when the detuning for the cooling and the repumper are $\Delta_{\text{cool,K}}$ = -3 Γ_{K} and $\Delta_{\text{rep,K}}$ = -2.5 Γ_{K}, respectively, Γ_{K} is the natural linewidth of the D_2 line of K. The power of the cooling is similar to the ^{87}Rb case. While as mentioned, the repumper power is half of that of the cooling. As the repumper is red detuned, it exerts a force on the atoms. Thus, the repumper power for the beams has to be balanced.

As a result of the difficulties of cooling ^{39}K, the Doppler cooling process is hampered, leading to a ^{39}K MOT with a temperature of $\sim$ 1mK. Similarly to the Rb case, we implemented a dark MOT stage (see section 4.1.3). In this case, we bring the repumper to resonance and reduce its power by a factor twenty of its value in the MOT stage, allowing us to cool down the sample to the Doppler limit, $T_D^K = 125\mu$K.

4.2.2 K Sub-Doppler cooling with D_2 molasses

In order to further cool down the atoms before trapping them in the optical trap, we implemented a molasses stage. There are two different strategies to implement them. The first one is to implement a gray-molasses using light close to the D_1 line [95] that allows for temperatures as cold as $6\mu K$. The second strategy is to use molasses close to the

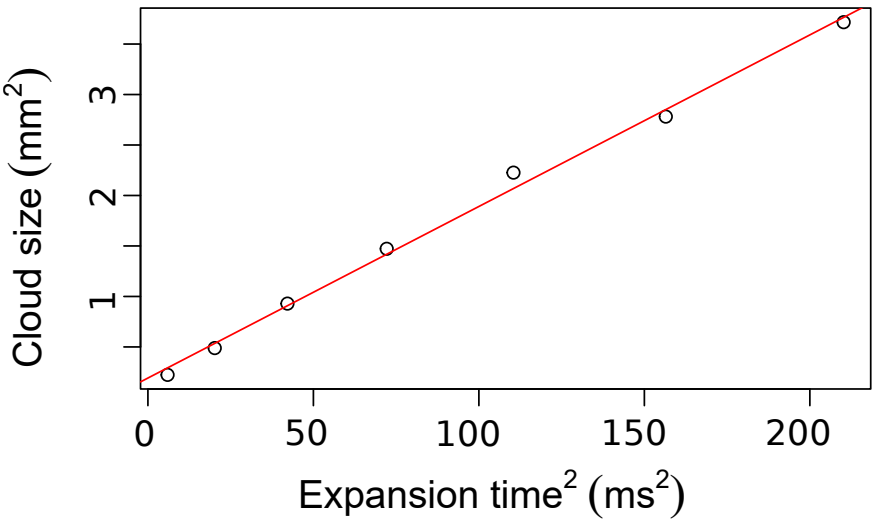


Figure 4.5: Determination of the temperature after molasses performed using the D_2 line of K. The obtained temperature from this fit is 80±3μK.

D_2 line [94], allowing for sub-Doppler temperatures as low as $25\mu K$. We chose the latter implementation as it did not require any additional laser. In our case, following the recipe found in [94], we were able to reach the sub-Doppler regime cooling with $(3.4\pm0.4)\cdot10^7$ atoms at 80±3μK. Figure 4.5 shows the size of the atomic cloud as a function of the expansion time. We used this measurement to determine the temperature. These were preliminary results in which we tuned the parameters over a large range. To do this in a reasonable time-scale, we only took a data point per set of parameters. Consequently, this figure does not have error bars and the error is the standard error of the fitting.

4.2.3 Loading K atoms in the dipole trap

When compared with the typical Rb values at the end of the dark MOT stage (see section 4.1.3), we found that the K atom number is one order of magnitude lower and its temperature is four times lower. Considering that the PSD, which is the figure of interest

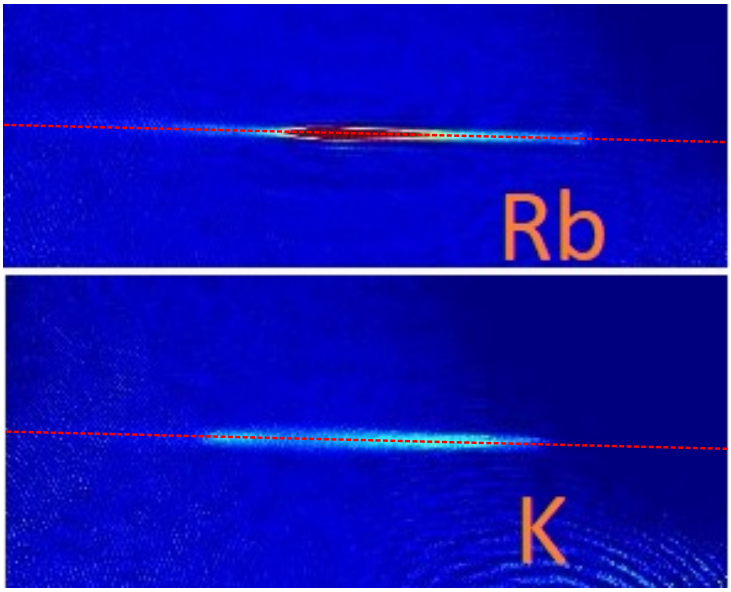


Figure 4.6: Absorption imaging picture of Rb (top) and K (bottom) atoms when loaded separately in the dipole trap. The dashed line is only a guide for the eye, placed at the same position.

to obtain a BEC, scales as PSD $\propto NT^{-3/2}$, we obtain a ^{39}K atomic sample with similar PSD to the one of ^{87}Rb prior to the loading in the dipole trap. One may expect then a similar behavior in the dipole trap loading and evaporation. However, we observed strong atom losses, being particularly evident in figure 4.6 where we compare both atomic species in the 1070nm dipole trap beam for the same dipole trap powers at the beginning of the evaporation. In the ^{87}Rb case, the main part of the atoms is located in the focus of the dipole trap beam, contrasting with the ^{39}K atoms that are avoiding the region with the highest intensity. This indicates the presence of light-induced losses due to the 1070nm dipole trap beam. To avoid this effect, we tried different ways of loading the trap, such as switching ON the trap during the different laser cooling stages (K MOT, dark MOT, K molasses) and ramping up the power of the trap. We also check the effect of the K cooling ligh in the Rb BEC and we observed some loses but for a time-scale longer than the usual of the experiment. The best ^{39}K loading results, shown in figure 4.6, were obtained when we ramped up the trap power during the molasses stage.

We found two other experiments, described in references [96] and [97], in which the authors obtained an all-optical K BEC. In reference [96], the authors observed enhanced losses for high powers of a 1070nm dipole trap beam. The possible explanation the author describes is the existence of a Raman transition to a bound molecular state (a process also known as photoasociation). In this process, the binding energy of the molecule gets converted into kinetic energy, and the molecule itself is lost from the trap. However, I have not been able to find any spectroscopy measurement concerning the cited transition. It is important to note that in our experiment, the beam waist is less than half than in the cited experiment. Consequently, we have a higher atomic density that may favor the collisions in the photoasociation process contributing consequently to the observed losses. In the experiment described in reference [97], they used a 1550nm laser, and they did not observe any of these phenomena even for a trap tighter than ours. Inspired by them, we tried with our 1550nm laser to trap the K atoms. However, our laser power was lower and so was our trap depth. This together with the fact that we can not perform D_1 bright molasses that can achieve temperatures of $\sim 4\mu$K, 20 times lower than ours, made the performance in this case worse than when we tried to trap the K atoms using the 1070nm laser.

4.3 Study of NEQT in a dissipative environment

As explained in the previous sections, we are able to experimentally realized a ^{87}Rb BEC and a ^{39}K MOT, the temperature of the K MOT is 1mK whose temperature is four orders of magnitude higher than that of the Rb BEC. We can overlap the K MOT with the Rb BEC, which leads to the *dissipation* of Rb atoms, since any collision between a K atom and a Rb atom results in the Rb atom being kick out of the optical trap.

In this section, I show how an experimental realization of a supercritical BEC by immersing it in a dissipative environment can be achieved. In the following, I discuss

how the obtained samples deviate from the BEC in equilibrium, how these supercritical states are longlived, the theoretical model behind the formation of such states, and the experimental implementation. The characterization of the collisions between both atomic species is described in section 4.4.

4.3.1 Supercritical BEC

As shown in section 2.1.1.1, the condensed fraction in an equilibrium situation, taking into account finite size effects and interactions is provided by equation 2.22 that I recall in the following expression,

$$F = \frac{N_0}{N} = \begin{cases} 1 - \tau^3 - \eta\tau^2(1-\tau^3)^{2/5} & \text{for } T < T_c \\ 0 & \text{for } T > T_c \end{cases} \tag{4.5}$$

where $\tau = T/T_c$ and $\eta = 2.15(aN^{1/6}/a_{\text{ho}})^{2/5}$. A supercritical BEC will be above the line described by equation 4.5. As it turns out, we can achieve a supercritical Rb BEC by immersing the Rb atomic sample in a cloud of cold K atoms while the evaporation of the Rb takes place. The experimental realization is depicted in figure 4.7. In essence, we use the same evaporation sequence for Rb as the one explained in section 4.1. The only difference is that we start to load the K MOT at a fixed time t_0, for which we measured the condensed fraction at different times.

The resulting data is reported in figure 4.8. We used the calibrated trapping frequencies shown in appendix A to calculate T_c in every point. In this figure, the open symbols represent the cases with no dissipation i.e. the equilibrium case in which the K MOT is not present. For open diamonds and circles, the waiting time, which is the time we keep the dipole trap at a constant power before imaging, is 4 s. In all the other cases, this time is 20 ms. For the data in the absence of dissipation, we varied the number of atoms

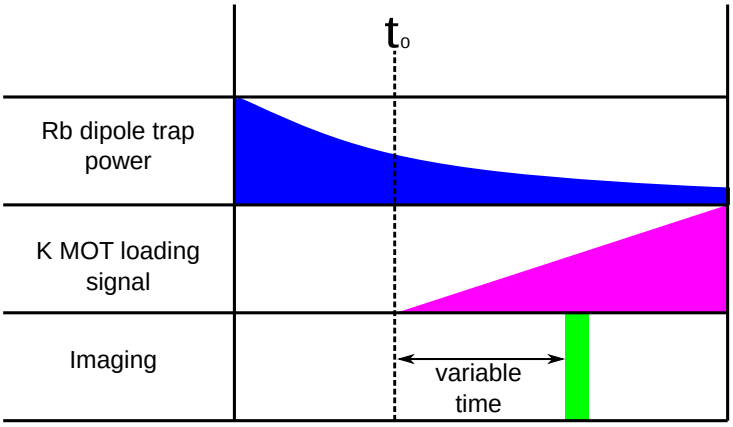


Figure 4.7: Experimental sequence used to obtain a supercritical BEC by dissipation.

from 70×10^3 to 25×10^3 at 3s before the evaporation end by changing the Rb MOT load time. We did this to double-check that the equilibrium case matched the theory for a wide range of parameters. The theoretical curve for the equilibrium case is the blue curve. We can observe how the data for the no dissipation case matches it perfectly.

In the dissipation case, represented by the filled points, we took two sets of data. For the filled circles the dissipation rate is four times the dissipation rate of the filled squares. The dotted lines are the results of the rate equation model that we developed to explain to model the physics behind the formation of the supercritical BEC. This model is explained in section 4.3.3.

Figure 4.9 compares the evolution of different parameters as a function of the evaporation time for the dissipation case (red circles), represented by the filled squares in figure 4.8, with the equilibrium case (blue triangles). As we can observe, for similar temperatures, we are able to obtain condensed fractions in the dissipation case higher than the expected values, represented by the dashed line in figure 4.9(c). We also calculated the chemical potential using the method explained in appendix B. Figure 4.10 shows the same but for the dissipation case, corresponding with the filled points in figure 4.8. In this case, the dissipation rate is four times stronger, and we can observe again the difference between the actual values of the condensed fraction and the theoretical ones for the

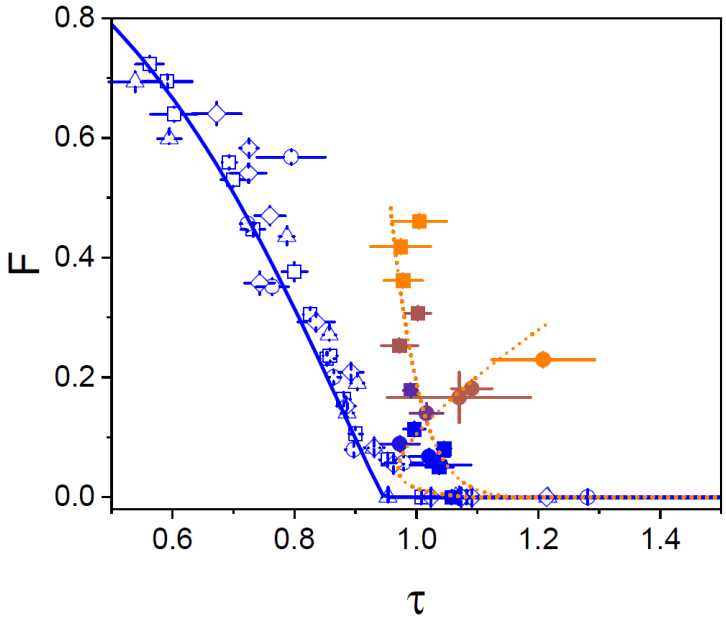


Figure 4.8: Phase diagram for the condensed fraction, F, versus the reduced temperature, $\tau = T/T_c$. Open symbols represent the data points in the no dissipation case and the filled ones with dissipation. For the filled circles the dissipation rate is four times the dissipation rate of the filled squares. The error bars are the standard errors of the mean of the measurements. The solid line represents the calculated equilibrium fraction while the dashed lines represent the calculated trajectories of the non-equilibrium situation, calculated using the model described in 4.3.3.

dissipation case.

4.3.2 Relaxation towards equilibrium state

To understand how the system restores to the equilibrium situation, we performed the experiment shown in figure 4.11. We switch off the K MOT at a time t_{off}, and we keep the dipole trap with the same parameters. Supposedly, under these circumstances, we should observe the usual situation that should follow equation 4.5. Following this idea, we measured the difference between the measured F and that expected using equation 4.5 for different times after switching off the K MOT, being δF this difference. The obtained results are in figure 4.12. In this case, we switch OFF the K MOT at t_{off}= 1.5 s. We

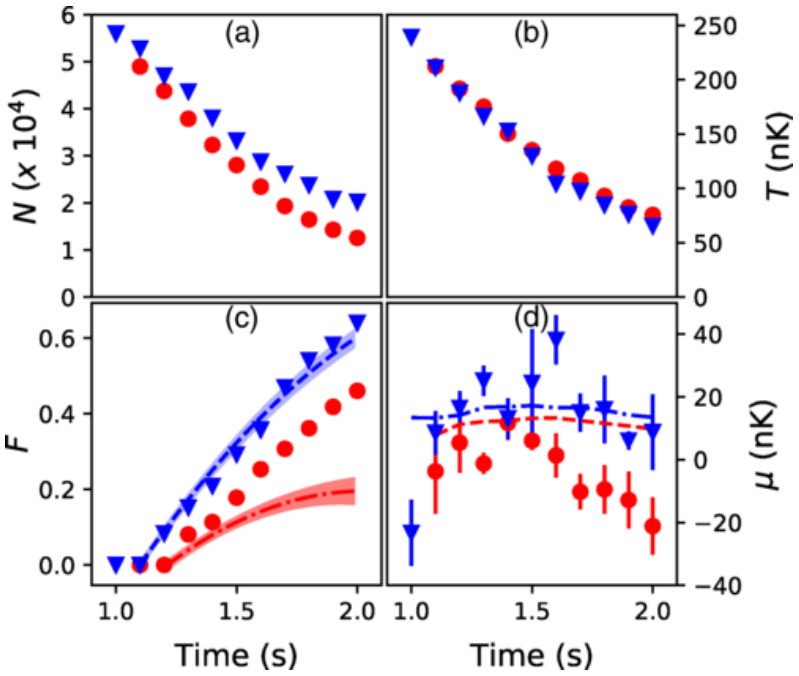


Figure 4.9: Different parameters for the experiment depicted in figure 4.7 versus evaporation time for a BEC with (red circles) and without dissipation. (a) is the atom number, (b) is the temperature, (c) is the condensed fraction where the dashed lines denoted the theoretical values in the equilibrium case and (d) is the chemical potential.

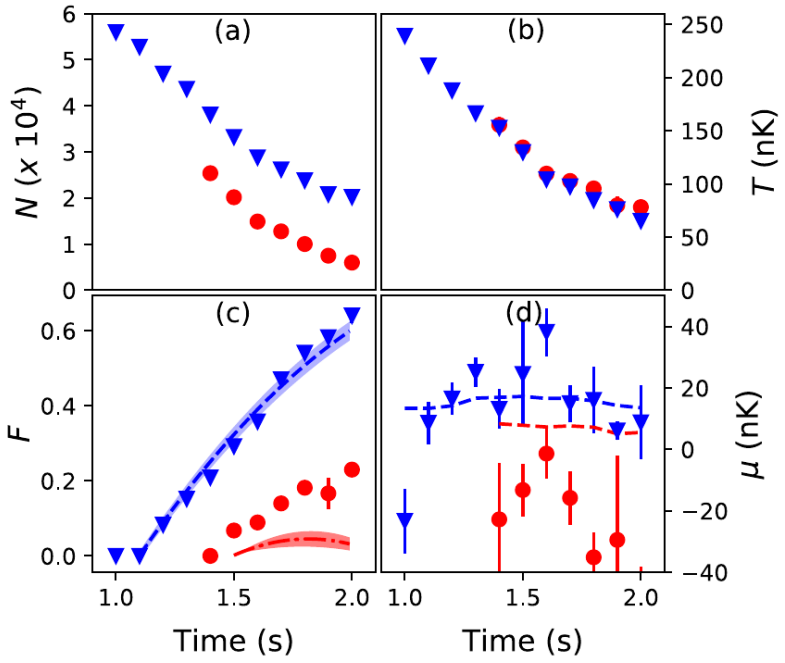


Figure 4.10: Same as figure 4.9 but for a dissipation four times stronger.

can observe how the system goes back to equilibrium as δF tends towards zero. We fitted an exponential curve in good agreement with the data to quantify the magnitude of the relaxation time. We found that the supercritical state has a lifetime in the order of seconds, as in this case, the time constant of the exponential fit is 3.9 ± 0.3 s. As for the evolution of the different experimental parameters, one can refer to figure 4.13.

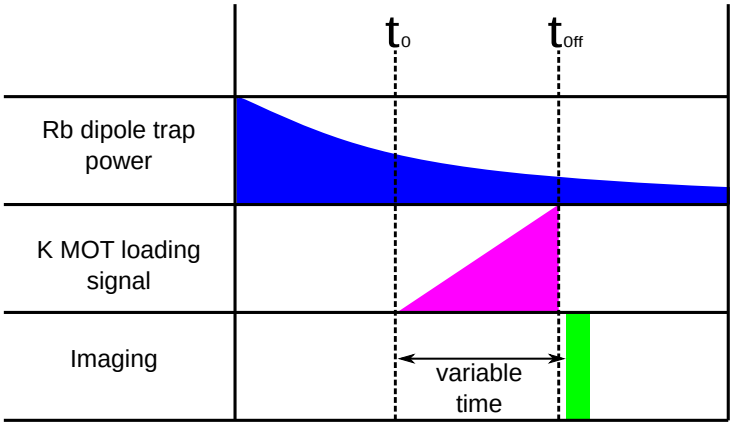


Figure 4.11: Experimental sequence used to study the relaxation of the supercritical BEC back to equilibrium.

4.3.3 Modeling the system

In section 2.1.4, I introduced a dynamical equation that describes the behavior of the condensate growth during evaporation. As explained, this is a complex many-body problem, and the microscopic theory behind it is quite complex. In fact, it has only been solved for a particular set of settings (constant temperature and infinite atom reservoir) with partial success [62, 64]. In our case, not only the atom reservoir is not infinite and the temperature variable, but we also have dissipation due to the K MOT. However, starting from equation 2.31, we developed a phenomenological rate equation that allows us to describe our experimental data and derive important information that might be used to develop a rigorous microscopic theory. Our model, depicted in figure 4.14, describes our system as a two-mode system, with one mode being the BEC and the other the thermal component. If we denote the condensate and thermal parts as N_0 and N_{th} respectively,

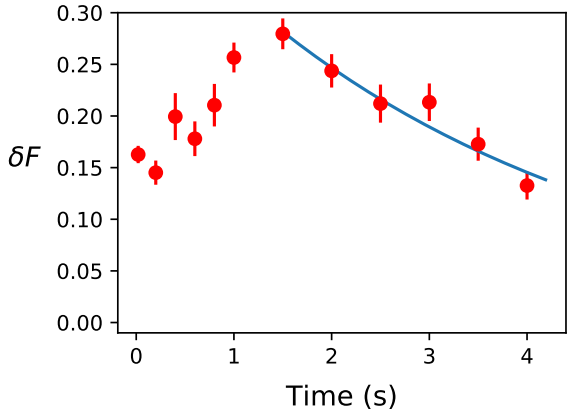


Figure 4.12: Difference between the measured F for the experiment depicted in figure 4.11. The line shows an exponential fit to the data after the dissipation is switched off. The time constant is 3.9 ± 0.3 s.

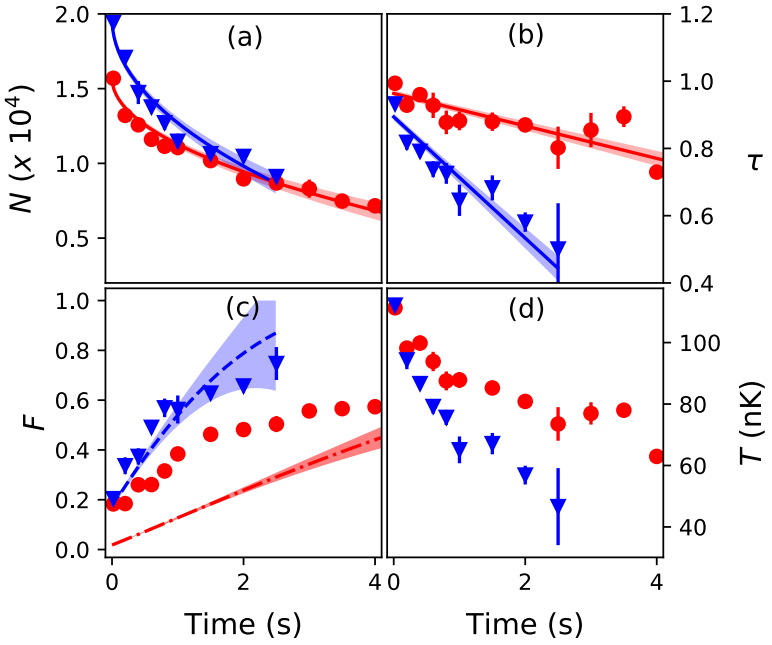


Figure 4.13: Different parameters for the experiment depicted in figure 4.11 versus evaporation time for a BEC with (red circles) and without dissipation (blue triangles). (a) is the atom number, (b) is the reduced temperature, (c) is the condensed fraction where the dashed lines denoted the theoretical values in the equilibrium case and (d) is the temperature.

we get the following rate equations,

$$\dot{N}_0 = \bar{W}\left[\left(1 - \frac{t}{t_f}\right) N_0 + 1\right] - \bar{K}(\tilde{N}_{th} + 1) - \gamma_K(t) N_0, \tag{4.6}$$

$$\dot{N}_{th} = -\bar{W}\left[\left(1 - \frac{t}{t_f}\right) N_0 + 1\right] + \bar{K}(\tilde{N}_{th} + 1) - [\gamma_K(t) + \gamma] N_{th}, \tag{4.7}$$

where γ_K is the dissipation rate coming from the K MOT, calculated in section 4.4.1 and γ the dissipation rate due to the evaporative cooling. The term proportional to N_0 in the square parenthesis and the one proportional to $\tilde{N}_{th}$ account for the bosonic stimulation [62, 64, 63]. The introduction of the effective number of thermal atoms, $\tilde{N}_{th}$, accounts for the reduction of the non-condensed energy band to a single state. Indeed, if we were considering such a state as populated by N_{th} atoms, its bosonic stimulation would be enhanced by a factor N_{th}. However, we need to take into account that the non-condensed energy band is not uniformly populated and that the more energetic levels are less involved in the exchange of particles. These two effects effectively reduce the bosonic stimulation. The amount of such reduction is difficult to evaluate. Therefore, $\tilde{N}_{th}$ is used as a free time-independent fit parameter.

For the BEC state, the exponential implies that the steady-state is reached when the chemical potential of the condensate equals the equilibrium chemical potential. In our model, we have made the approximation that the energy levels are time-independent. To account for the reaching of the steady-state in absence of dissipation, we replace the exponential in equation (2.31) with t/t_f, where t_f is the time at which the steady-state is reached and all the atoms are in the BEC. In general, the coefficients W and K are complicated functions of T, μ, N_0 and N [62, 64, 63] and an expression for them exists only for the case of constant temperature and infinite reservoir of atoms. Even in this case, as mentioned above, the coefficients can be wrong up to an order of magnitude. For these

reasons, in our model, we drop the functional dependence and treat them as constants having average values $\bar{W}$ and $\bar{K}$. In references [62, 64], the growth of the condensate is the result of the unbalancing between the two-body scattering process that transfers atoms from the thermal component to the BEC and the opposite process, without creation or absorption of quasiparticles. Using quantum kinetic theory, the authors found that

$$\bar{W} \simeq e^{(\epsilon_{th}-\epsilon_0)/k_B T}\bar{K}, \tag{4.8}$$

meaning that for a given temperature, the larger is the energy gap the harder it is to excite an atom to the thermal component and the easier is to promote an atom in the condensate. The exploitation of this effect allows us to drive the system out of equilibrium. The energy gap, $\epsilon_{th} - \epsilon_0$, can be roughly estimated from the energy spectrum obtained with a first-order treatment of a uniform Bose gas with contact interactions. For $\tau \leq 1$, this reduces to [98, 99]:

$$E = \sum_p \frac{p^2}{2m} + \frac{4\pi\hbar^2 a N^2}{mV}\left(1 - \frac{1}{2}F^2\right) \tag{4.9}$$

The last term of this equation is of quantum mechanical origin and accounts for bosonic stimulation. From equation 4.9, it follows that once an atom is in the condensed phase, it needs an amount of energy $\Delta = 2\pi\hbar^2 a N_0/mV$ to leave the BEC, yielding an unbalancing between $\bar{W}$ and $\bar{K}$. More detailed calculations including higher-order perturbation theory [98, 99] and the effect of the mean-field potential of the BEC [64, 63] show that the spectrum exhibits a strong modification of the density of states right above the condensed state. Therefore, equation 4.9 is valid only for low values of F. Regardless, for $\tau \simeq 1$, in our experimental conditions, $\epsilon_{th} - \epsilon_0$ is already of the same order of magnitude as T.

Concerning the data shown in figure 4.15, to derive $\bar{W}$ we fit the curve $N_0(t)$ in

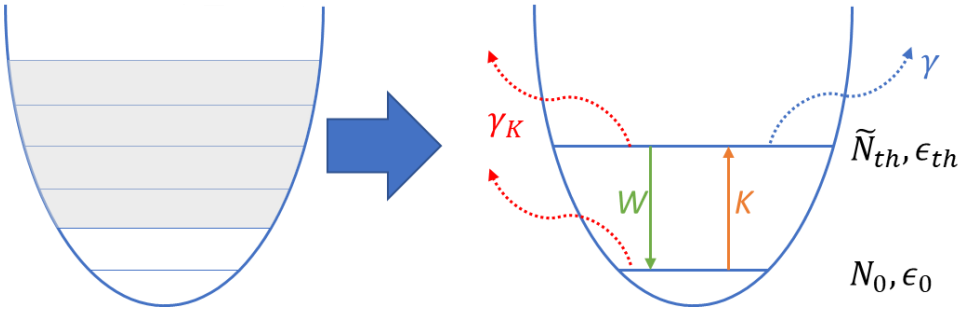


Figure 4.14: Depiction of model used and described by equations 4.6 and 4.7.

absence of dissipation with the solution of

$$\dot{N}_0 = \bar{W}\left[\left(1 - \frac{t}{t_f}\right) N_0 + 1\right] \tag{4.10}$$

with $t_f = 1.4$ s the time at which the evaporation ends (please note the origin of time is shifted by 0.6s in this data analysis), obtaining $\bar{W} = 3.45 \pm 0.1$ Hz. We derive $\bar{K} = 0.25 \pm 0.03$ Hz from an exponential fit of the relaxation curve in figure 4.12. The evaporation loss rate $\gamma = 0.95 \pm 0.03$ Hz is obtained by fitting with an exponential the decay of the total number of atoms in absence of dissipation. Finally, $\gamma_K(t)$ is obtained as explained in the next section. The only free parameter of our model is $\Xi = N_{th}/\tilde{N}_{th}$, which determines the effective occupation of the thermal energy band. We found that we can reproduce our data, as shown in figure 4.15, by imposing $\Xi = 25 \pm 5$, value obtained by fitting the data of the mentioned figure. The result of our model is also reported as the dotted trajectory in the $\tau - F$ plane in figure 4.8. By increasing the dissipation rate γ_K by a factor of four, leaving all the other parameters unchanged, we obtain the second trajectory that reproduces well the open circle data in figure 4.8.

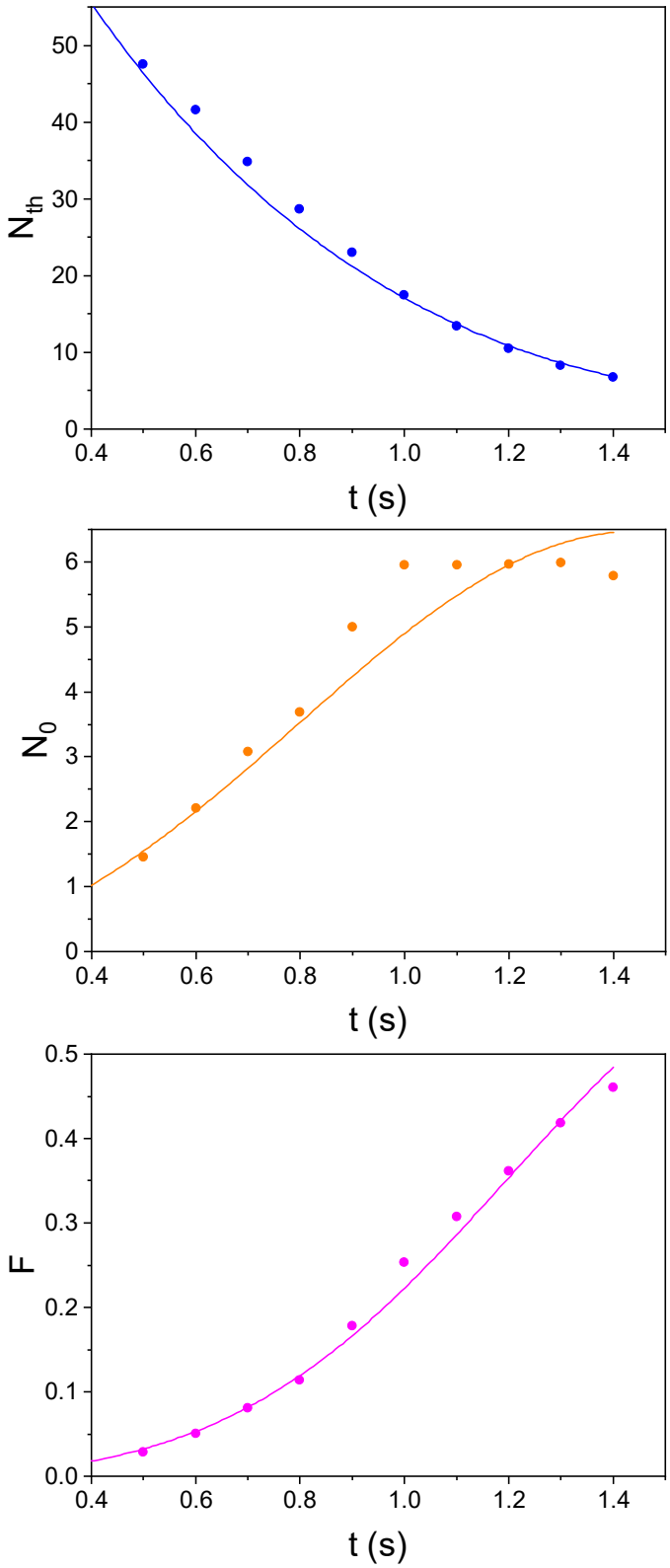


Figure 4.15: From top to bottom, evolution as a function of time of the number of atoms in the thermal component, the number of atoms in the BEC and the condensate fraction F. The points are the experimental data when the dissipation is ON, the lines are the results of our model.

4.4 Inducing dissipation in the Rb BEC

As the dissipation is caused by the collisions between the K and Rb atoms, it is important to understand the physics behind them and characterize them. Thus, in this section, I explain how we determined the scattering rate between both atomic species and the corresponding experimental measurements. Before this, I would like to mention that we measured the effect of the K cooling light in the Rb atoms and we did not observe relevant Rb losses in the considered time-scale due to the K cooling light.

4.4.1 Measuring the interspecies scattering rate

We used the model described in 2.1.3 to model the collisional process between both atomic species. Following this model, we consider the background atoms to be the K atoms and the ultracold atoms to be the Rb atoms. We first calculate E_c, using equation 2.24, where C_6=4290(2)$a_0^6 E_h$, value that we extracted from [60]. This yields $E_c \simeq 300$ μK allowing us to calculate the collisional cross section, σ_K, using equation 2.27. The result we obtained is $\sigma_K \simeq 5.61 \times 10^{-17}\mathrm{m}^2$. We can then obtain a theoretical prediction of the scattering rate, γ_K, using equation 2.29 as,

$$\gamma_K = n_K \sigma_K v_K, \tag{4.11}$$

where the density of K atoms, n_K, is measured directly in the experiment and v_K is obtained from the measured temperature*. To obtain the experimental value of γ_K we can use equation 2.30. We include as well the losses of Rb atoms in absence of the K MOT, characterised by its scatering rate, γ_{Rb}. These losses can be simply modeled as one body loses processes. This means that the rate equation can be rewritten as,

*We consider the average kinetic energy to be the thermal energy, so $v_K = \sqrt{2k_b T_K/m}$.

$$\dot{N}_{Rb} = -(\gamma_{Rb} + \gamma_K)N_{Rb} = -(\gamma_{Rb} + n_K \sigma_K v_K)N_{Rb}. \tag{4.12}$$

In plain evaporation†, γ_{Rb} is constant while γ_K is not, since n_K increases with time. From the experimental data we determined that this increase is linear in time, so we can write $\gamma_K = at$. Thus, we obtain the following equation,

$$\dot{N}_{Rb} = -(\gamma_{Rb} + at)N_{Rb}, \tag{4.13}$$

differential equation which solution is,

$$N_{Rb}(t) = N_{Rb}(0) \exp\left(-\gamma_{Rb}t - \frac{a}{2}t^2\right). \tag{4.14}$$

The experimental sequence used is depicted in figure 4.16. We evaporate the Rb following the recipe explained in section 4.1. At a certain point in the evaporation, t_0, we stop the evaporation by keeping the dipole trap power constant, and then, we start loading K atoms in the MOT. We then image the Rb cloud for different times after we switch on the K MOT. In the case with no K atoms, we impose $a = 0$ obtaining γ_{Rb} by fitting equation 4.14. Then, we repeat the measurement with the K atoms allowing us to obtain a by fixing the value of γ_{Rb} to the one previously obtained. One question that emerged was if γ_K depended on the possible Rb states (BEC or thermal). To answer this question we repeated the experiment for both cases, a pure Rb BEC and a pure Rb thermal cloud by simply changing t_0. The data and the corresponding fits of this measurements are shown in figure 4.17. We concluded that within experimental error of the data shown in figure 4.17, the value of γ_K is the same for a given n_K regardless of the Rb state.

†Plain evaporation refers to the evaporation that takes place for constant intensity of the dipole trap beams.

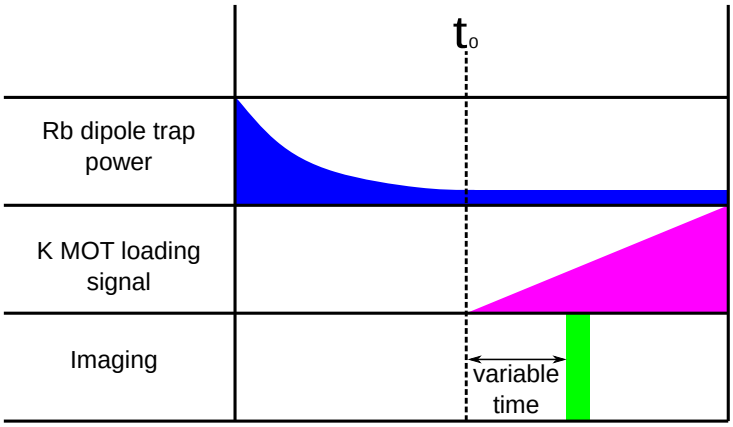


Figure 4.16: Experimental sequence used to measure the scattering rate between the two species.

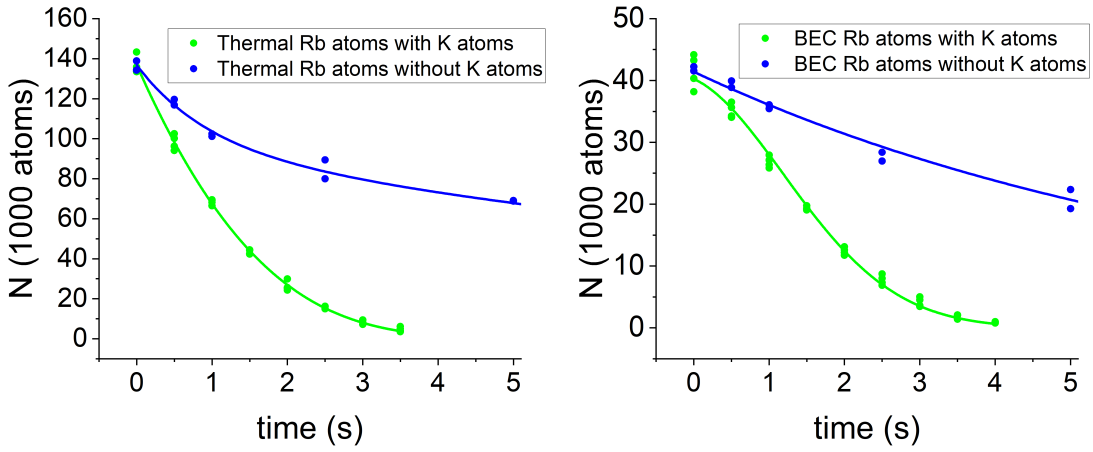


Figure 4.17: Rb atom number as a function of time with and without K atoms, for both Rb thermal cloud (bottom) and Rb pure BEC (top).

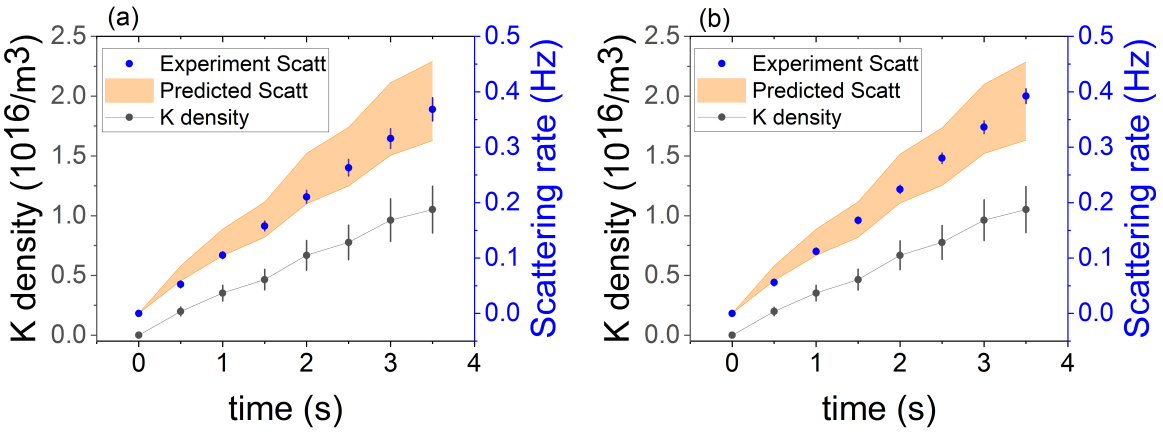


Figure 4.18: Theoretical prediction and experimental values for the scattering rate, γ_K. The shown n_K is the K atom density that we used for the theoretical predictions. (a) corresponds to the case of all the Rb atoms in the thermal component and (b) corresponds to the case with all the Rb atoms in the BEC component.

Finally, in figure 4.18 we compare the theoretical prediction with the obtained experimental values. From it, we conclude that the model explains the observed losses in Rb atoms. The error in the theoretical prediction is large, since it depends on n_K, which depends on the cloud volume. Considering that $n_K \propto 1/r^3$, where r is the radius of the cloud, any small noise in the determination of r magnifies when determining n_K. We performed the measurement for a pure thermal and a pure BEC, the corresponding results are shown in figures 4.18(a) and 4.18(b), respectively. In both cases, the experimental data obtained by fitting the rate equation found in equation 4.14 agrees with the theoretical value calculated using equation 4.11.

4.4.2 Why non-equilibrium quantum thermodynamics?

Before discussing about non-equilibrium, we have to clearly distinguish between the two types of equilibrium in our system. Firstly, we have thermal equilibrium, we consider our system to be in thermal equilibrium when we perform the measurements as we wait for it to rethermalize for few ms before taking our measurements. Then, we have the

dynamical equilibrium, this equilibrium refers to the equilibrium between the different phases in absence of external perturbations. As shown in this chapter, when we stopped applying the dissipation, the system restored its dynamical equilibrium in few seconds. This means that the system was out of equilibrium or equivalently in a non-equilibrium situation. It is also important to note that even considering that the dissipation is a mainly classical mechanism in this case, it affects the formation of the BEC by affecting the Bosonic stimulation that occurs when the condensation takes place. The Bosonic stimulation is in fact a quantum process, being the reason why this chapter is called non-equilibrium quantum thermodynamics.

Chapter 5

Towards the realization of a single atom quantum engine

In this chapter, I describe the planned design to build our single-atom quantum engine. Some of the required concepts and the corresponding background are presented in section 2.2. Considering that this realization is still under development, I provide a description of the current state of the system and the challenges encountered, and the proposed solutions. In this case, we use the same experimental setup but with the addition of an optical tweezer that allows for the manipulation of a single atom, which is presented here.

5.1 Components of the single-atom quantum engine

To understand a quantum engine, one needs to establish the parallelism between the components of a classic and a quantum engine. Thus, the components are:

- The **working fluid**, which undergoes the different thermodynamic transformations. In our case, the working fluid is the single ^{41}K atom trapped in an optical tweezer,

see section 5.2, and cooled down via sympathetic cooling using the thermal bath.

- The **thermal bath** has to be large when compared with the working fluid so that the transfer of heat between it and the working fluid does not affect its temperature. This role is played by an ultracold cloud of ^{87}Rb that we are able to cool down by evaporative cooling to the quantum level, see section 4.1.

- The **piston** drives some of the thermodynamics transformations of the working fluid. The optical tweezer is the piston in our system. It is species selective, allowing for transformations of the working fluid without affecting the thermal bath, see section 5.2.

- **Tunable interactions between the working fluid and the thermal bath**, this allows for the implementation of other thermodynamic transformations. In our case, we use the hetero-nuclear Feshbach resonances between both atomic species, see section 2.2.3.

5.2 Developing a species-selective optical tweezer

To develop a species-selective optical tweezer, we require a laser wavelength that only affects one of the atomic species. We recall the expression from section 4.1.4,

$$U_d(\mathbf{r}) = \frac{\pi c^2 \Gamma}{2} \left(\frac{2}{\omega_2^3 \Delta_{2,F}} + \frac{1}{\omega_1^3 \Delta_{1,F}} \right) I(\mathbf{r}). \tag{5.1}$$

Using this expression, we calculate the dipole potential as a function of the wavelength. In figure 5.1 we report this calculation for both Rb (red) and K (blue). In this plot, for a wavelength of 789.820nm, marked by the dashed line, there is no dipole potential for the Rb but there is for the K. This allows for the manipulation of the K atoms without affecting the Rb.

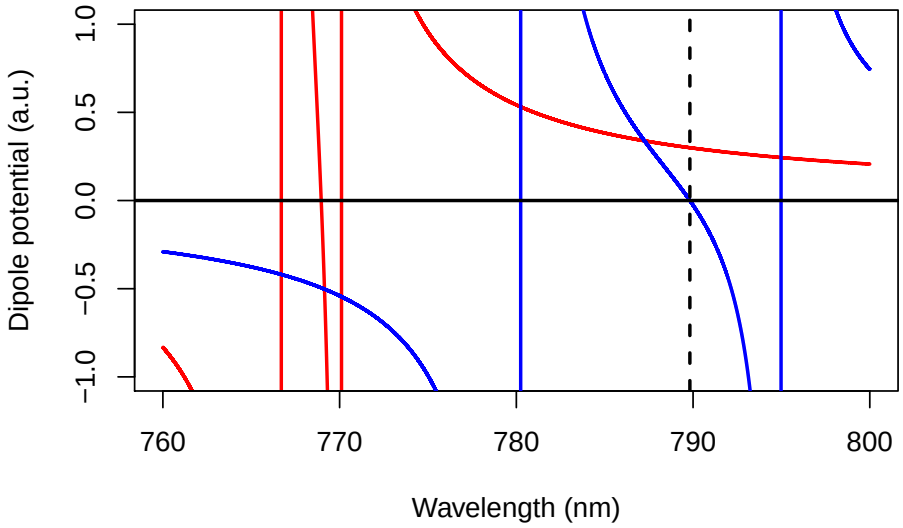


Figure 5.1: Dipole potential for both Rb (blue) and K (red) as a function of the dipole trap laser wavelength. The vertical dashed line is the magic wavelength for Rb (789.820nm).

For the cited wavelength, for a power of 25mW and a beam waist of w =2μm the calculated trapping frequencies are (f_x, f_y, f_Z)=(15.7,153,152) kHz. Where the x direction is the direction of the propagation of the tweezer trap light.

5.2.1 Heating rate

Despite the fact that the trapping potential for Rb is zero by design, the heating rate due to the dipole is not. Thus, we calculate it, using the equation extracted from [58], the heating rate, $\dot{T}$, in a harmonic dipole trap is,

$$\dot{T} = \frac{2}{3} T_{\mathrm{rec}} \bar{\Gamma}_{\mathrm{sc}} \tag{5.2}$$

where T_{rec} is the recoil temperature of the atom and $\bar{\Gamma}_{\mathrm{sc}}$ is the mean scattering photon

rate that we estimate as the scattering photon rate in the center of the trap, this is fact provides us with an upper limit of the heating rate as the scattering photon rate reaches its maximum in the centre of the trap,

$$\Gamma_{\rm sc} = \frac{\pi c^2 \Gamma^2}{2} \left(\frac{2}{\omega_2^3 \Delta_{2,F}^2} + \frac{1}{\omega_1^3 \Delta_{1,F}^2} \right) I(\mathbf{r}_0). \tag{5.3}$$

The resulting heating rates are 132 μK/s and 664 μK/s for the K and the Rb, respectively. The desired regime we want to reach is of the order of 1 μK and the time scale of part of the experiment in which the two species interact is of 10 ms. This means that the atoms will be heated up by 1 μK. However, the tweezer has to be ON when the K MOT is loaded, this takes around 100ms. This light is not affecting all the atoms as the beam waist is smaller than the atomic cloud and we do not know yet how this will work. In any case, if the heating effect is excessive, we could move the tweezer as it is loaded and then move it back using a piezo transducer in the microscope.

5.2.2 Collisional blockade

As explained, the tweezer is essentially a dipole trap. However, it is designed to trap a single atom. The physical mechanism that allows for the single atom loading is known as collisional blockade. This guarantees the existence of a loading regime of atoms into the tweezer in which it is only possible to load a single atom. This regime can be explained using the model of atom loading into a dipole trap found in reference [100]. In this model, the number of atoms into the trap is described as,

$$\frac{dN}{dt} = R - \gamma N - \underbrace{\frac{\beta}{V}}_{\beta'} N(N-1), \tag{5.4}$$

where R is the loading rate, $-\gamma N$ describes the one-body decay and $-\beta/VN(N-1)$ the two-body decay where β is independent of the volume, V. The volume is approximated as [101],

$$V = \pi w_0^2 z_R \ln \frac{1}{1-\eta} \sqrt{\frac{\eta}{1-\eta}}, \tag{5.5}$$

with w_0 the tweezer waist, z_R its Rayleigh length and $\eta = k_B T/|U_0|$, where U_0 is the potential depth. Thus, the volume depends on the waist which modifies the value of β allowing for different loading regimes of the trap. In reference [101], the authors report the loading of a single atom for a big range of possible the possible parameters in a tweezer with a waist of 0.9μm.

5.2.3 Tweezer loading

To load the atoms in the tweezer, we have to prepare the atomic sample by cooling it down and increasing its density. We start by loading the ^{41}K MOT for two seconds. We then do a dark MOT stage similar to the one for ^{39}K, explained in section 4.2.1, this allows for the cooling of the atoms from $\sim$1mK of the K MOT to the Doppler limit of K, 125μK. Then we compress the MOT by increasing the magnetic field gradient from 10G/cm to 20G/cm. We also, tune the set of compensation coils so that the center of the compress MOT overlaps with the focus of the tweezer beam. In this stage, we switch ON the tweezer light and it is overlapped with the compressed MOT for 50ms. This overlapping time is enough to load the tweezer. This is still being optimized.

5.2.4 Fluorescence imaging of a single atom

We perform fluorescence imaging to measure the single atom. In standard fluorescence imaging, like the one perform in the MOT, we set the cooling and repumper lights at resonance to maximize the scattering of light by the atoms. However, this heats up

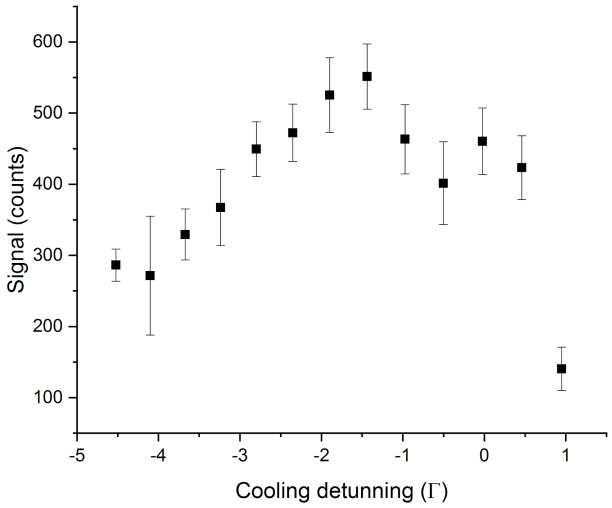


Figure 5.2: Signal from the atoms trap in the tweezer versus the detuning of the cooling in the fluorescence imaging stage. The error bars are the standard errors of the signal measured for 10 shots.

the atoms which escape from the trap. Thus, the detunings are red-detuned as in the molasses. This keeps the temperature low and prevents the atom from escaping the trap, allowing for a long interrogation time. Using this technique, we can collect atoms for ∼50 ms, which is long enough to obtain a signal strong enough. The scattered photons are collected by the same microscope objective used to focus the tweezer light and focus down in the camera, see section 3.3. We optimize the signal in the camera for different detunings of the cooling and repumper, the corresponding results are shown in figures 5.2 and 5.3, respectively. For the power used in the cooling and the repumper beams and their detunings we estimated that there were around 15 atoms in the tweezer during these measurements. In this case, we could not distinguish different peaks in the histogram of the signal counts. Normally for few atoms, less than 5, we should be able to distinguish different peaks. In this particular examples, the trap waist is $\sim 7\mu$m and we wait 320ms after we switch the K MOT lights before imaging so that the atoms from the K MOT can escape, imaging time is 50ms.

Another important point is that the presence of tweezer light shifts the energy levels, which is detrimental for the imaging especially considering the small frequency difference

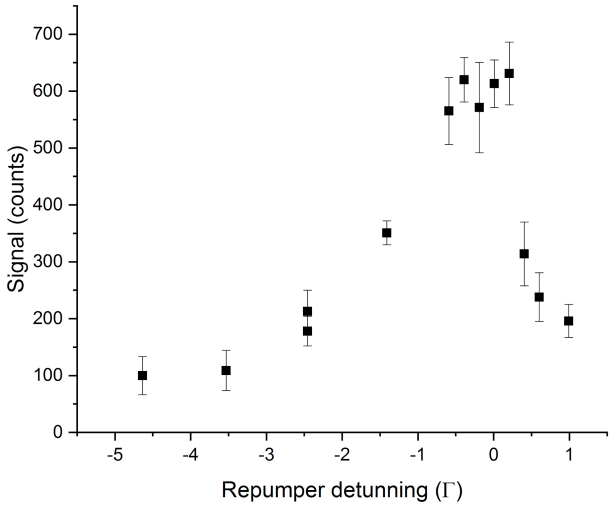


Figure 5.3: Signal from the atoms trap in the tweezer versus the detuning of the repumper in the fluorescence imaging stage. The error bars are the standard errors of the signal measured for 10 shots.

between the hyperfine energy levels in the excited manifold of ^{41}K (figure 3.5). This can cause dipole force heating, inhomogeneous detunings, and the inhibition of laser cooling that is required to perform the fluorescence imaging of the single atom. Inspired by the method developed in [102], we chop the fluorescence and tweezer lights. To do so, we switch on and off both lights alternatively so that when the fluorescence light is on, the tweezer is off, avoiding the undesired light shifts. The chopping frequency has to be much larger than the trapping frequency of the tweezer, which is in the order of tens of kHz. Thus, we set the chopping frequency at 700KHz for all the measurements presented here. In this case, the frequency is so fast that can be considered as an adiabatic process, which translates into the effective trap depth of the tweezer being half of the original one.

5.3 Future steps

Since the completion of this thesis, single-atom trapping has been achieved. The future step is to study the rethermalization of the single atom with the Rb bath, and the effect of the tunable interactions in this process. The current team is trying to avoid the heating

of the Rb bath by the tweezer light using a nanopiezo controller to move the tweezer light away when not required, avoiding unnecessary heating.

Chapter 6

Realizing the Frenkel-Kontorova model with Rydberg-dressed atoms

In this chapter, I present the work related to the proposal of an implementation of the FKM with cold Rydberg dressed atoms in an optical lattice. In this work, we show that by using Rydberg dressing and realistic experimental parameters, it is possible to realize at least two different variants of the FKM. As shown in section 6.1, we concentrate on a springlike interaction potential, similar to the original FKM, and a repulsive potential. In section 6.3, we calculate the phase diagrams of the system for both cases, which feature the characteristic incommensurate and commensurate configurations. We show how the equilibrium configurations take the form of different *devil's staircases* as the amplitude of the lattice potential is varied. In section 6.4, we focus on the system in the incommensurate configuration. We show that depending on the interaction potential, it is possible to observe either an Aubry-like transition or a crossover from an unpinned phase to a pinned one. Interestingly, the crossover is characterized by the excitation of a *soft mode*, resembling the phason mode typical of infinite systems.

Although its qualitative results are useful, the FKM uses a non-realistic infinite-

range spring interaction potential. It is therefore beneficial to develop a fully controlled system where the effect of realistic interaction potentials can be tested. Cold atoms systems are ideal candidates for this purpose due to their high degree of control and flexibility. The introduction of optical lattices allowed for the study of several models that explain different condensed matter phenomena such as the Superfluid-Mott insulator phase transition [103, 104], Anderson localization [105, 106] and the effects of quantum magnetism [107]. Furthermore, long-range interactions can be achieved using atomic species with high permanent dipolar moments [108], dipolar molecules [109] or Rydberg-dressed atoms [110]. In particular, Rydberg-dressed atoms have the advantage of enabling the control of the range and functional dependence of the interaction potentials, using various Rydberg states for the dressing. These dressed states are achieved by weakly admixing excited Rydberg states with the ground state, using near-resonant light [111].

This chapter contains a partial reproduction of my first author publication found in reference [43]. I made the simulations, collaborated in the data analysis and wrote the manuscript of the cited publication.

6.1 The system

The system studied is portrayed in figure 6.1. It consists of N atoms arranged in a 1D chain placed in a tunable optical lattice. In this case, tunable means that we can tune the lattice spacing and depth. A dressing field is used to produce the desired Rydberg dressed states. For the particular cases studied here, we checked explicitly that any n-body potential is a sum of 2-body potentials. To do so, we checked the effect of adding the n-body interactions in the cases were particles are the closest and we concluded that there was not observable effect. Thus, we only consider nearest neighbors' interactions in our calculations. Considering that the positions and momenta of the particles are x_i and P_i respectively, our system is described by:

$$E = \sum_{i=1}^{N} \frac{P_i^2}{2m} + \frac{1}{2} \sum_{i=1}^{N-1} c_1 V_{\text{int}}(x_{i+1} - x_i) + \sum_{i=1}^{N} \left[V_0 - V_0 \cos\left(2\pi x_i / b\right) \right], \tag{6.1}$$

In this equation, $V_{\text{int}}(x_{i+1} - x_i)$ is the normalized nearest neighbor interaction between the particles, V_0 is the depth of the lattice potential control by the lattice power, b is the lattice spacing, m is the mass of the atoms and c_1 is a coefficient that scales the strength of the interaction between particles. In this particular case, it is equivalently to say that c_1 accounts for the amount of Rydberg admixture in the dressed state that varies the interaction strength.

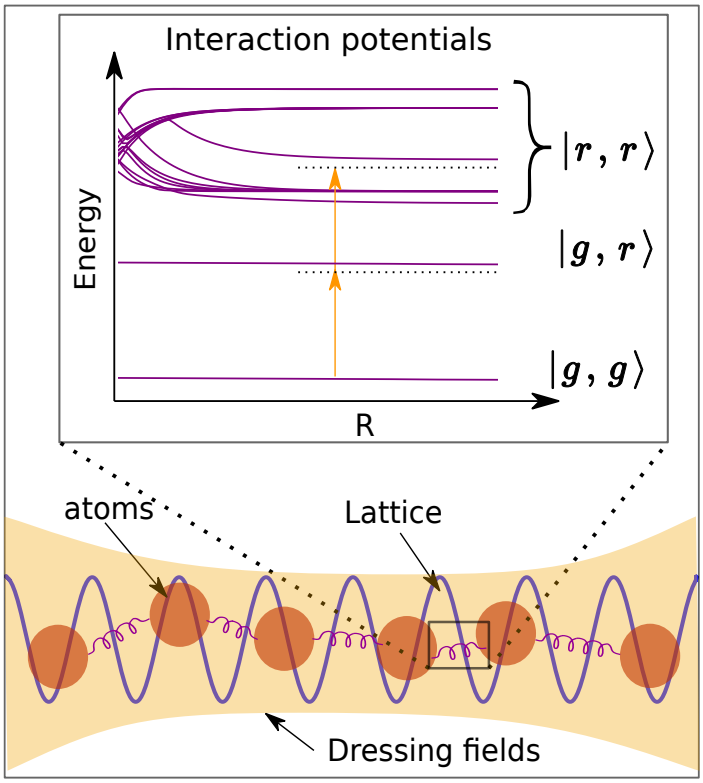


Figure 6.1: Depiction of the schematics of the model. The atoms are placed in a monodimensional optical lattice. The inset depicts the interactions between the atoms that are realized by dressing the atoms' ground state with Rydberg levels.

This model has been widely studied. Reference [112] contains a theoretical study of Rydberg atoms in optical lattices focusing on the quantum dynamics of the system. They show that this system can be experimentally realized, allowing for the experimental

study of a system with long-range interactions. Reference [113] is another theoretical study of this type of system. In this case, the authors discuss the effect of disorder and its band structure. Although they do not directly mention the FKM, they characterize their system by two length-scales. A similar system has been realized experimentally by placing a BEC in an optical lattice and exciting its atoms to the Rydberg level [114]. This last publication focuses on the effect of Rydberg interactions in the BEC and how it affects the coherence of the BEC.

In our calculations, we chose two different interactions potentials that can be realized experimentally. In what follows I will refer to them as the *springlike* and the *repulsive* potentials, which are depicted in figures 6.2 (a) and 6.2 (b), respectively. The way we calculated the interaction potentials from the chosen Rydberg dressed states is shown in section 6.2. The *springlike* potential is described by the following expression:

$$V_{\text{int}} = \frac{-1}{(1 + c_0(r - r_0)^2)} + \frac{e^{-c_2(r-r_0')}}{c_1}, \tag{6.2}$$

where r_0, c_0, c_1, c_2 and r_0' are parameters obtained by fitting last expression to the calculated interaction potential. In the case of the repulsive potential, the interaction potential can be described as:

$$V_{\text{int}} = \frac{1}{(1 + e^{c_0(r-r_0)})} + \frac{e^{-c_2(r-r_0')}}{c_1}, \tag{6.3}$$

and again r_0, c_0, c_1, c_2 and r_0' are parameters obtained by the fitting.

In our case, to provide a feasible experimental implementation we chose ^{87}Rb atoms. These are dressed with different Rydberg levels depending on whether we are interested in the springlike or in the repulsive potentials.

In the springlike case we use the Rydberg levels $60P_{1/2}$. In this case, the dressing can be achieved by single photon transition, $5S_{1/2} \rightarrow 60P_{1/2}$ which can be driven by an UV

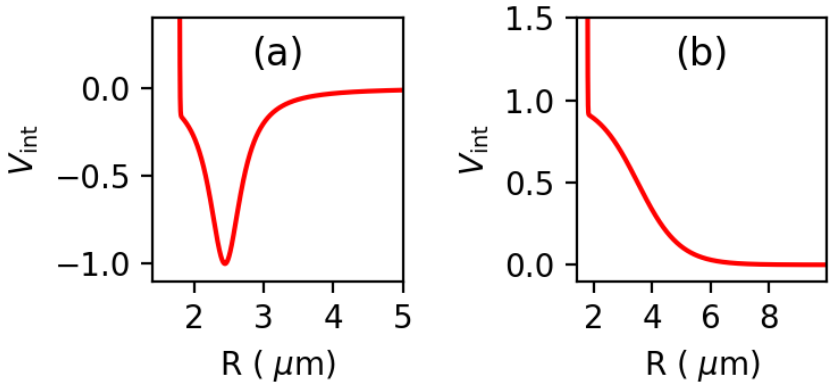


Figure 6.2: Normalized interatomic potentials obtained by dressing the atoms with Rydberg states, as explained in the text. (a) The springlike potential (b) The repulsive potential.

laser at 297.11nm. This results in the following values of the parameters of equation 6.2, $r_0 = 2.440$ μm, $c_0 = 12.951$ μm^{-1}, $c_1/k_B = 783.6$ nK, $c_2 = 263$ μm^{-1}, $r_0' = 1.8127$ μm.

The repulsive case requires the atom to be dressed with the Rydberg level $60S_{1/2}$. In this case, it is not sufficient with a single photon transition. It requires a two-photon transition to reach the desired Rydberg level. The first transition takes the atom from $5S_{1/2}$ to $6P_{1/2}$ using a 421.67 nm laser and the second transition is $6P_{1/2} \rightarrow 60S_{1/2}$, which requires a laser at 1013.76 nm. This results in the following value of the parameters of equation 6.3, $r_0 = 3.494$ μm, $c_0 = 1.382$ μm^{-1}, $c_1/k_B = 248.9$ nK, $c_2 = 145$ μm^{-1} and $r_0' = 1.811$ μm.

The already mentioned tunable optical lattice can be realized by interfering two lattice beams at a certain angle. The lattice spacing will vary then as the angle is changed. This technique allows for the required tunability to study our model, and it has already been experimentally realized, like the examples shown in references [115, 116]. In this work, the lattice spacing is varied in the range $1.9 - 4.5$ μm, which is experimentally feasible. Furthermore, Rydberg-dressed atoms can be used in conjunction with optical lattices as they have proven to be stables against losses when placed in them, reference [117] is an

example of such implementation.

6.2 Rydberg-dressed states

In this case, the criteria to choose the Rydberg-dressed states was that they present an interaction potential that interests us. Thus, we chose ^{87}Rb dressed with the Rydberg levels $60S_{1/2}$ and $60P_{1/2}$. Appendix C contains the basic theory to describe a system of two Rydberg-dressed atoms. As in that appendix, we define $\Delta_i = \omega_i - \omega_{\mathrm{L}}$ as the detuning of the laser used for the dressing with respect to the transition between $|g\rangle$ and $|r_i\rangle$, which are the ground and Rydberg states, respectively. We define r_{t} as the target Rydberg that we want to couple the laser light to. Assuming that the laser wavelength is large detuned respect to the transition, so that $\Delta_i >> \Delta_t$ for all $i \neq t$ we can neglect all levels $|g, r_{i\neq t}\rangle$ and $|r_{i\neq t}, g\rangle$. Thus, we only keep $|r_i, r_j\rangle$ as $D_{ijkl}(R)$ is of the same order of magnitude as Δ_t. Under these assumptions, we obtained that the Hamiltonian for this system is,

$$\begin{aligned} H_r =& \hbar \Bigg[\Delta_t(|g,r_t\rangle\langle g,r_t| + |r_t,g\rangle\langle r_t,g|) + \sum_{i,j}(\Delta_i+\Delta_j)(|r_j,r_i\rangle\langle r_j,r_i| + |r_i,r_j\rangle\langle r_i,r_j|) \\ &+ 2\Omega_i(|g,g\rangle\langle g,r_t| + |g,g\rangle\langle r_t,g|) + 2\Omega_i^*(|g,r_t\rangle\langle g,g| + |r_t,g\rangle\langle g,g|) \\ &+ \sum_i 2\Omega_i(|g,r_t\rangle\langle r_i,r_t| + |r_t,g\rangle\langle r_t,r_i|) + 2\Omega_i^*(|r_i,r_t\rangle\langle g,r_t| + |r_t,r_i\rangle\langle r_t,g|) \\ &+ \sum_{i,j,k,l} D_{ijkl}(R)\,|r_i,r_j\rangle\langle r_k,r_l| + D_{ijkl}^*(R)\,|r_k,r_l\rangle\langle r_i,r_j| \Bigg]. \end{aligned} \tag{6.4}$$

In order to obtain the interaction potential, we diagonalized the Hamiltonian from equation 6.4 to get the dressed eigenstate and extract the eigenvalue closest to the state $|g,g\rangle$. The results of this calculation are shown in figure 6.3. Figure 6.3(a) shows the

energy of the state dressed by $60S_{1/2}$ Rydberg level for ^{87}Rb atoms as a function of the interatomic distance. In this case, the Rabi frequency is $\Omega_t/2\pi = 8$ MHz and $\Delta_t/2\pi = 30$ MHz. In this calculation, 243 Rydberg states were used, and the Rydberg-Rydberg interaction included dipole-dipole, quadrupole-dipole and quadrupole-quadrupole terms.

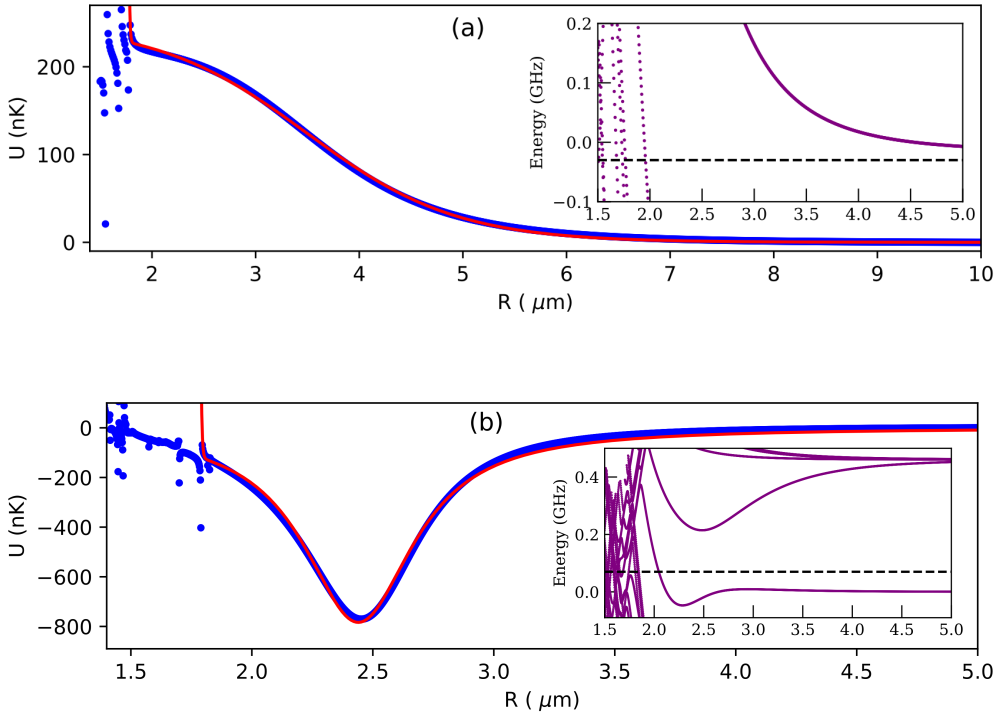


Figure 6.3: *Top panel, (a):* The energy of the state dressed by $60S_{1/2}$ Rydberg level for ^{87}Rb atoms as a function of interatomic distance. *Lower panel, (b):* The energy of the state dressed by $60P_{1/2}$ Rydberg level for ^{87}Rb atoms as a function of interatomic distance. Inset shows how the interaction between Rydberg atoms changes as a function of interatomic distance. The dressed line shows where the dressed laser is resonant.

Figure 6.3(b) shows the energy of the state dressed by $60P_{1/2}$ Rydberg level for ^{87}Rb atoms as a function of interatomic distance. In this case $\Omega_t/2\pi = 15$ MHz and $\Delta_t/2\pi = -70$ MHz. In this calculation we used 282 Rydberg states, and the Rydberg-Rydberg interaction included dipole-dipole, quadrupole-dipole and quadrupole-quadrupole terms. For the numerical diagonalization, we modified the Python library ARC [118] to include the dressing field. Considering these results, we named the two interacting potentials for $60S_{1/2}$ and $60P_{1/2}$ as *repulsive* and *springlike*, respectively. In both cases, we fit a function

to obtain an analytical expression for the potential. In these particular cases, we used following the equations to fit the calculated values of the interaction potentials,

$$U_{\text{repulsive}} = \frac{248.9}{1 + e^{1.382(x-3.494)}} + e^{-145(x-1.811)} \tag{6.5}$$

$$U_{\text{springlike}} = \frac{783.6}{1 + 12.95(x-2.44)^2} + e^{-263(x-1.813)} \tag{6.6}$$

6.3 The phase diagrams

This section is devoted to the calculated phase diagrams for the ground state configurations of the system for the springlike and the repulsive cases. As already mentioned, the FKM presents two length scales. In this case, the lattice spacing, b, is one of them. The other one is the distance that minimizes the interaction potential, denoted by a. As a result of the competition between these two length scales, we obtain a mean interatomic distance $\tilde{a}$ that results from the minimization of E in the case $V_0 \neq 0$. $\tilde{a}$ may present a complicated dependence with respect to the different parameters of the system.

The different values of $\tilde{a}$ characterize the two possible phases of the system, commen-

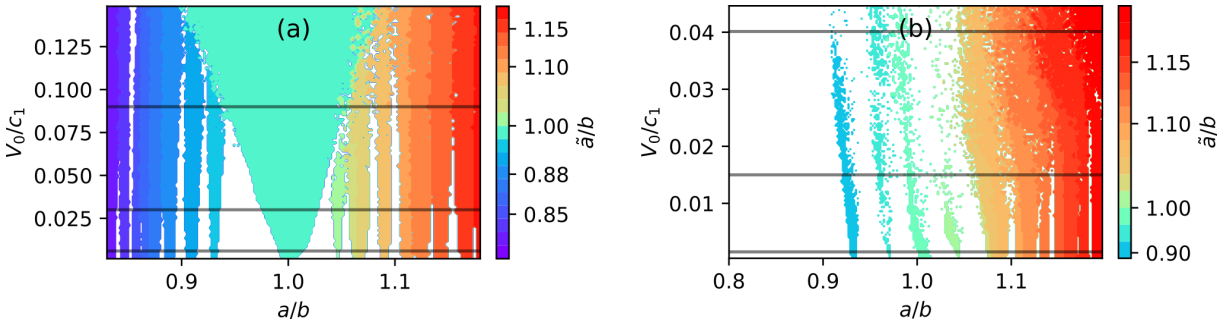


Figure 6.4: Phase diagram showing $\tilde{a}/b$ as a function of a/b and V_0/c_1 for (a) the springlike potential and (b) the repulsive potential. Each color represents a different lock-in region, characterized by a commensurate configuration where $\tilde{a}/b$ is rational.

surate and incommensurate. A configuration is commensurate if for two integers, Q and R, the positions of the atoms can be described by the following expression, $x_{Q+i} = x_i + R \cdot b$ where i is the index of the atom. Evidently, if this equation holds then the ratio $\tilde{a}/b$ is rational since $\tilde{a}/b = R/Q$. On the contrary, if $\tilde{a}/b$ is irrational the configuration is incommensurate.

The way we calculate the phase diagram was by calculating the different ground states. This problem is not trivial to solve numerically since the energy function has many variables, which are the particle positions. Consequently, there are many local minima, so a gradient descent algorithm will not work in this case. After some trial and error, during which we tried the particle swarm algorithm, the simplex method, and other minimization algorithms from the Fortran NAG library, we finally used the generalized simulated annealing algorithm described in reference [119]. To find the ground states we minimize equation 6.1, imposing $P_i = 0$ so that the particles are at rest. We then minimize the function for different values of V_0 and b, which are the parameters that can be tuned in a possible experimental realization of this model. The number of atoms in all the calculations we made was $N = 50$ since a smaller number of particles means border effects become too strong and a larger number is out of the order of magnitude of what it is experimentally achievable. In the case of the repulsive potential, we added hard walls to the system since otherwise the particles will separate indefinitely. In this case, the hard walls will fix a. We chose $a = 3.17\mu$m so that the particles sit where the interaction potential is approximately half of its maximum value. These hard walls could be implemented using the method described in reference [120]. However, this is not required in the case of the springlike interaction, since a is fixed by the position of the minimum of the interaction potential, in our case, this results in $a = 2.44\mu$m.

As a result of our calculation, we obtained the phase diagrams shown in figure 6.4. In these phase diagrams, we show $\tilde{a}/b$ as a function of both, a/b and V_0. The commensurate phase is indicated by the colored regions. These regions are the largest *lock-in regions* in

which $\tilde{a}/b$ is rational. On the other hand, the smaller lock-in regions and incommensurate configurations are represented by the white regions in the phase diagrams. It is important to note that considering that we have a finite system, $\tilde{a}/b$ will always be rational. That is why we consider the commensurate phase to be only the largest lock-in regions. In both cases, when $V_0 = 0$, the system is in the *floating phase* where a/b can take any value since there is no competition between both length scales. Commensurate configurations start to appear as we increase V_0 since they become more energetically favorable. This causes the phase diagram to break into lock-in regions, resulting in intervals with the same rational value for $\tilde{a}/b$ in the neighborhood of each rational value of a/b. As shown in the phase diagrams, the amplitude of these lock-in regions increases with V_0. In the limit when $V_0/c_1 \gg 1$, the particles are pinned to the minima of the lattice allowing only for commensurate configurations.

6.3.1 The springlike case

We can start analyzing the springlike case. This case is quite similar to the FKM in which the interactions between particles are modeled by springs. Figure 6.5 (a) shows $\tilde{a}/b$ as a function of a/b for three values of V_0/c_1, indicated as black horizontal lines in figure 6.4 (a). In figure 6.5 (a.1), for small but finite values of V_0/c_1 we can observe small intervals of zero slope start to appear in the curve $\tilde{a}/b$ versus a/b around $a/b \approx 1$, because $\tilde{a}/b \approx 1$ is very energetically favorable as in this point $a \approx b$, meaning that there is no competition between the lengthscales.

The zero slope intervals, which belong to the locking regions, are centered around commensurate values of a/b and correspond to $\tilde{a}/b$ taking the same rational value (horizontal dashed lines). This curve is a combination of zero and non-zero slope regions. This type of curves is called *incomplete devil's staircase* in contrast with the devil's staircase that looks similar, but its slope is zero in its whole domain. The transition from

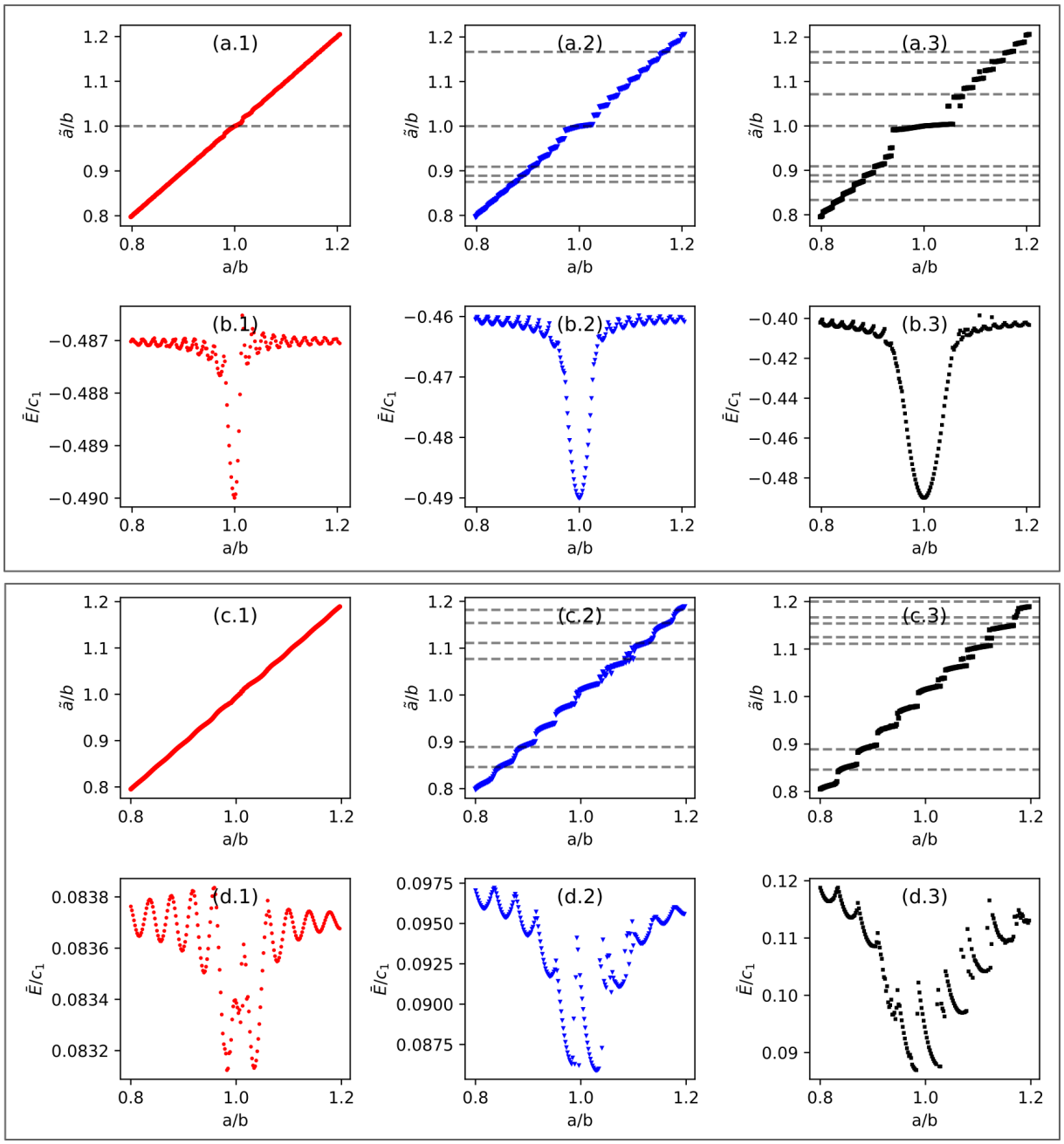


Figure 6.5: (a.1,2,3) and (c.1,2,3) show the mean interparticle distance with respect to the ratio a/b for springlike and repulsive potentials respectively. (b.1,2,3) and (d.1,2,3) show the energy per particle ($\bar{E}$) with respect to the ratio a/b. Here $V_0/c_1 = 0.006, 0.03, 0.09$ and $0.0015, 0.015, 0.04$ for springlike and repulsive potentials respectively. The horizontal dashed lines show the locations of a few rational values of $\tilde{a}/b$.

commensurate to incommensurate requires the creation of a *discommensuration* with its associated energy cost. The energy cost causes the formation of the different locking regions. This effect is clear in graph 6.5 (b.1), in which we report the energy per particle as a function of a/b. When we move away from $a/b = 1$, the energy per particle increases until we reach an energy value higher than the required to create a discommensuration when the transition to the incommensurate phase takes place. Figures 6.5 (a.2 and a.3) show that if we increase V_0/c_1 we can observe the emergence of more lock-in regions since the energetic cost of a discomensuration increases as shown in figures 6.5 (b.2 and b.3). In these figures and figure 6.5 (b.1), we can see how the energy cost of a discommensuration increases as the energy dip in $a/b = 1$ is deeper as we increase $V_0/c1$. The result is the widening of the lock-in regions and the consequent narrowing of the incommensurate regions. When V_0/c_1 reaches a high enough value, the curve $\tilde{a}/b$ vs. a/b becomes a *complete devil's staircase*, which is clear in figure 6.5 (a.3). This effect is interesting since this transition from an incomplete to a complete devil's staircase is of special interest for some condensed matter systems like, e.g., polymers. We can also observe how every locking region has a minimum of energy, the depth of which defines how much energy we need to create a discomensuration, which is why the larger lock-in region is at $a/b = 1$ where we can find the deeper energy dip.

6.3.2 The repulsive case

Moving into the repulsive case, we show in figures 6.5 (c) and 6.5 (d) results similar to the ones shown in figures 6.5 (a) and 6.5 (b) but for the repulsive case. The first thing we notice is that in this case, the lock-in regions do not present a zero slope but some curved shape instead, resulting in an *anomalous* incomplete devil's staircase. Thus, in every lock-in region, there is a mixture of commensurate and incommensurate configurations. This result is compatible with the corresponding phase diagram in figure 6.4 (b) in which a large portion of it is white since the commensurate configurations do not extend as much

in our range of parameters. These anomalous lock-in regions increase as their counterparts do in the springlike case when V_0/c_1 is increased. However, it does not matter how much V_0/c_1 is increased that the slope of the lock-in regions remains finite. Thus, in this case, the devil's staircase is always incomplete. As shown in figure 6.5 (d), the energy signature of the lock-in regions is similar to the springlike case with an energy dip in the center of each lock-in region, although in this case, the energy around the minimum is asymmetric, being compatible with the observation of the anomalous lock-in regions.

6.4 Incommensurate configurations

As previously mentioned, our system is incommensurate when the ratio a/b, or equivalently the ratio between the interatomic distance and the lattice spacing, is irrational. The effects of the incommensurations are more evident as we choose higher irrational numbers. A higher irrational number means that we need higher integer values (p,q) to approximate it by a fraction, p/q. It is important to recall that our system is finite and consequently, a rational value with high enough values of p and q, in the order of N, will exhibit an incommensurate behavior. This type of system shows a transition from an unpinned to a pinned configuration as V_0/c_1 is increased. In the pinned phase, the possible positions of the particles with respect to the lattice potential are limited to certain values given the compromise between the interactions and lattice strengths. This phase transition also affects the phonon spectrum of the configurations. When it takes place, a gap opens in the minimum value of the phonon spectrum [121]. The original Frenkel-Kontorova model presents a similar phase transition. In the case of infinite particles, this transition is known as the Aubry transition [122]. The signatures of the phase transition in our system and in the original FKM are almost identical. However, the type of system is not formally the same, as a finite chain can not be perfectly incommensurate. Thus, the phase transition in our system is named as Aubry-like transition. A clear Aubry-like transition

is only observed in the springlike case, which is more similar to the FKM. In the repulsive case, we observe a crossover regime rather than a phase transition. The signatures for each of the phases are similar in both cases.

6.4.1 Incommensurate ground states

As previously mentioned, as we cross to the pinned phase, the particle positions can only take certain values with respect to the lattice minima. Thus, we plotted x_i/b mod 1 for the different values of V_0/c_1 in figure 6.6. x_i/b mod 1 is the function modulus, and in this context, we use it to obtain the normalized distance between a particle and the closest lattice minima found before such particle. We chose $a/b = 0.873$ since we required an incommensurate configuration, and the results were clearer for this particular value.

Starting with the springlike case, which is reported in figure 6.6(a), the transition is clear and takes place at the critical value $V_0/c_1 = 0.19$. Below the critical value, the particles can take almost any position. Above the critical value, the particles are pinned to the regions near the lattice minima. The reason behind this is that the springlike potential is short range. Thus, when the lattice is deep enough so that it is energetically favorable for them to scape the potential dip of the interaction, the particles will roll to the bottom of the lattice potential.

In the repulsive case, shown in figure 6.6(b), although we indeed observe a transition between the two phases as V_0/c_1 is increased, the transition itself is not abrupt, and it is a rather smooth crossover region between the two phases between $V_0/c_1 = 0.03$ and $V_0/c_1 = 0.04$. The repulsive interaction is long-range, so the competition between the lattice and the interaction is more complicated to depict than for the springlike case. However, this opens the window of the study of systems whose features are intermediate between the pinned and unpinned phase.

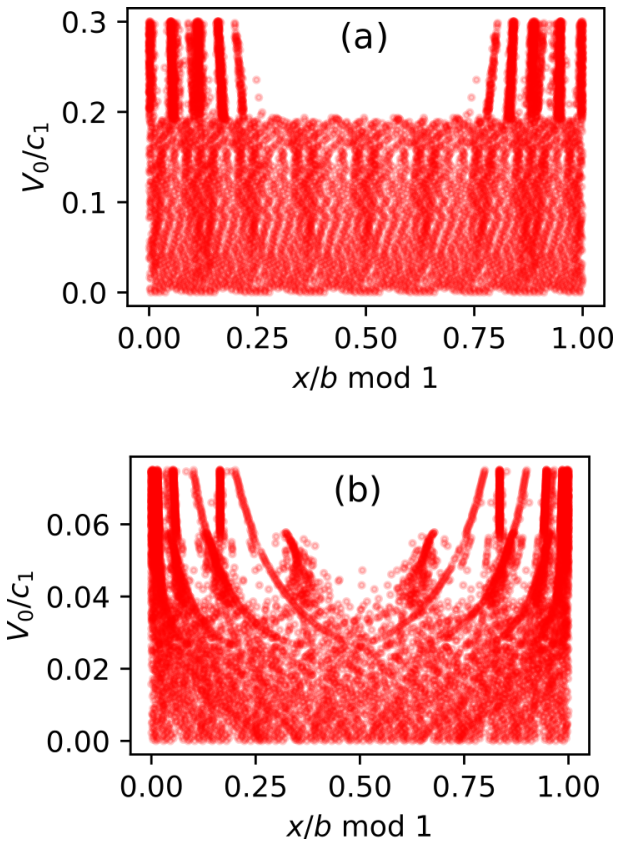


Figure 6.6: Particle position with respect to the lattice potential for each value of V_0/c_1 for (a) the springlike and (b) the repulsive case, respectively. Here the system is incommensurate with the ratio $a/b = 0.873$.

6.4.2 Phonon spectrum

Moving to the study of the phonon spectrum, we have already mentioned the gap opening for the minimum frequency. In the FKM, when considering an infinite incommensurate system, it can present a gapless Goldstone mode known as phason. This so-called phason corresponds to the zero-frequency mode. As this system goes from the unpinned to the pinned phase, undergoing the Aubry transition, this mode disappears. To understand why this happens, we need to take into consideration that phasons are associated with the invariance of the uniform relative translation of the phases of modes with relatively irrational periodicities. As the system undergoes the Aubry phase transition, the particles start to be pinned to certain positions relative to the lattice potential. Thus, particles

can not move following the dynamics of the zero-frequency mode. Thus, this mode disappears, and the minimum frequency in the phonon spectrum is non-zero, which causes the emergence of the mentioned gap.

Our system is not infinite, and thus we can not observe a perfect phason. However, we can observe an almost-zero frequency mode that disappears as we go across the Aubry-like transition or the cross-over region in the springlike or repulsive case, respectively. In particular, the cross-over region in the repulsive case is interesting since it allows for the observation of soft modes. A soft-mode is an excitation about the ground state that becomes a phason as $N \to \infty$ [123], limit in which the energy of such excitation vanishes.

In order to calculate the phonon spectrum, we assume that they correspond with small displacements respect the ground state configuration. Thus, we can write the following expression:

$$x_i = x_i^G + u_i, \tag{6.7}$$

where x_i is the position of a particle, x_i^G is the position of the same particles in the ground state and u_i is a small displacement. Then, the energy of the system can be expressed as a Taylor expansion,

$$E \approx E_0 + \sum_i \cancelto{0}{\frac{\partial E}{\partial x_i}\Big|_{\{x_i^G\}}} u_i + \frac{1}{2}\sum_{k,l} \frac{\partial^2 E}{\partial x_k \partial x_l}\Big|_{\{x_i^G\}} u_k u_l, \tag{6.8}$$

where E is the total energy, E_0 is the total energy of the groundstate and $\{x_i^G\}$ denotes the ground state configuration. The linear term vanishes as $E(\{x_i^G\})$ is a minimum. Thus we can write a change in energy due to small displacements as:

$$\Delta E \approx \frac{1}{2}\sum_{k,l} \frac{\partial^2 E}{\partial x_k \partial x_l}\Big|_{\{x_i^G\}} u_k u_l \tag{6.9}$$

We consider that for a small displacement every particle behaves like a harmonic

oscillator. We then recall the usual expression to calculate the harmonic oscillator energy,

$$E = \frac{1}{2}ku^2 = \frac{1}{2}m\omega^2 u^2, \tag{6.10}$$

where ω is the frequency, m is the mass of the particles and u the displacement. Thus, the total change in energy of the system, ΔE, for small displacements is:

$$\Delta E \approx \frac{1}{2}\sum_i m\omega_i^2 u_i^2, \tag{6.11}$$

where we have considered that the variation of energy respect the ground state for small displacements is simply the sum of the energy of each particle considered as if they were in a harmonic oscillator. Now we can replace ΔE by the expression given in equation 6.9:

$$\sum_{k,l} \frac{\partial^2 E}{\partial x_k \partial x_l}\Big|_{\{x_i^G\}} u_k u_l = m\sum_i \omega_i^2 u_i^2. \tag{6.12}$$

The last expression can be rewritten as,

$$\sum_l (D_{kl} - \omega_l^2 \delta_{kl}) u_l^2 = 0, \tag{6.13}$$

which is an eigenvalue problem where the matrix D_{kl} is called the dynamical matrix, defined as,

$$D_{kl} = \frac{\partial^2 E}{\partial x_k \partial x_l}\Big|_{\{x_i^G\}} \tag{6.14}$$

and the eigenvalues, λ_j, of such matrix are the squared frequencies of the possible phonons that can appear in the system, ω_j^2. In this case, for convenience, we introduce the adimensional phonon frequency, $\bar{\omega}_j$, as,

$$\bar{\omega}_j = \omega_j \sqrt{\frac{ma^2}{c_1}}. \tag{6.15}$$

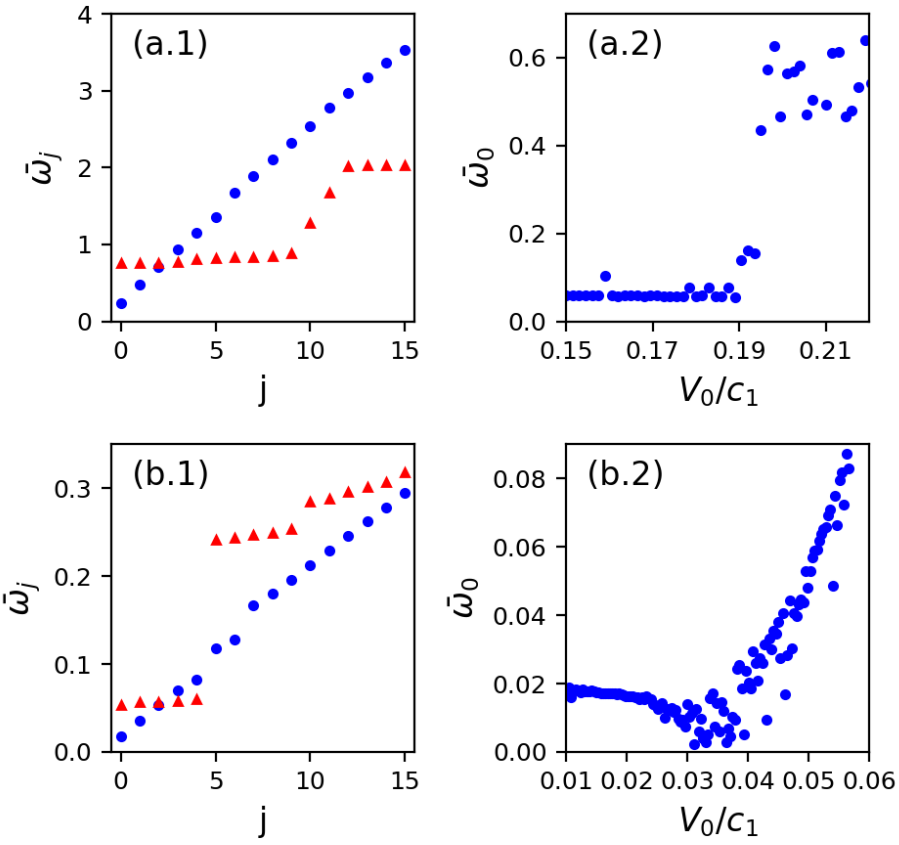


Figure 6.7: (a.1) Adimensional frequencies for the 15 lowest modes of the phonon spectrum for the springlike case for $V_0/c_1 = 0.180$ (blue dots) and $V_0/c_1 = 0.201$ (red triangles). (b.1) is the same for the repulsive case for $V_0/c_1 = 0.01275$ (blue dots) and $V_0/c_1 = 0.024$ (red triangles). (a.2) and (b.2) show the frequency of the lowest mode as a function of V_0/c_1. In all cases the system is incommensurate with the ratio $a/b = 0.873$.

Using the dynamical matrix, we calculated the phonon spectrum of our system. We chose $a/b = 0.873$ for the repulsive and springlike cases. In the springlike case, we report the frequency of the 15 lowest phonon modes in figure 6.7 (a.1) for $V_0/c1 = 0.180$ (blue dots) and $V_0/c_1 = 0.201$ (red triangles), which correspond to the unpinned and pinned phases, respectively. In this case, we can observe how the gap opens for the minimum frequency, which is almost zero in the unpinned phase. In figure 6.7 (a.2) we plotted the frequency of the lowest phonon mode, $\bar{\omega}_0$, as a function of $V_0/c1$. In this case, we can observe an abrupt transition for $V_0/c_1 \simeq 0.19$, as ω_0 increases abruptly. This is in agreement with the conclusions of section 6.4.1, as the transition is located in the same

value of $V_0/c1$ and we observed an Aubry-like transition.

We performed the same analysis in the repulsive case. In this case in figure 6.7 (b.1) we chose the values $V_0/c1 = 0.01275$ (blue dots) and $V_0/c_1 = 0.024$ (red triangles) for the unpinned and pinned phases respectively. We again observe how the gap opens for the frequency of the lowest phonon mode. However, in this case, we observe a different behavior in figure 6.7 (b.2) in which we again report $\bar{\omega}_0$ as a function of V_0/c_1. Firstly, in this case, we observe how $\bar{\omega}_0$ decreases as we increase V_0/c_1 until we reach $V_0/c_1 \simeq 0.32$, point in which it reaches almost zero and after which it increases again. This point is due to the already mentioned soft mode, which is similar to the one present in the infinite FKM. As V_0/c_1 is increased, the system crosses-over to the pinned phase. The cross-over behavior and smooth change of $\bar{\omega}_0$ is compatible with the observations made in section 6.4.1

In both cases, we observe how the frequencies of the phonon modes form a staircase in the pinned phase. This is compatible with the results of the original FKM, in which the phonon spectrum also forms a staircase in the incommensurate pinned phase [121]. The critical value of V_0/c_1 at which the phonon gap opens in both cases depends on a/b. The critical value decreases as we approach a rational value of a/b. When a rational value of a/b is reached, a commensurate phase is reached and thus, the pinned to unpinned transition is not observed.

6.5 Experimental implementation

While the required Rydberg-dressing can be implemented using the details from section 6.2. As for the experimental realization of the ground states, one can cool down the atoms in a lattice. The lattice depth will have to be set to the required value depending on which part of the phase diagram is of interest. Then, the Rydberg dressing fields will

be switched on, introducing the inter-atomic potentials. Some examples corresponding to experiments in which this is achieved can be found in references [111, 124]. In these experiments, many-body dynamics due to the Rydberg dressing has been observed.

Another problem is the temperature, as thermal noise may prevent from distinguishing the ground states. As for our case, temperatures ranging from a few nK to tens of nK should be sufficiently low to distinguish between the different locking regions. In figure 6.5, we show that the typical energy difference between the lock-in regions is in the order of the mentioned temperature requirement.

Concerning the observables of our proposal that can be measured directly in an experiment, one would be interested in the particles' position that would allow obtaining experimentally $\tilde{a}$ and x_i/b mod 1, which is the variable used in our phase diagrams. To achieve this, microscopic techniques for quantum gases as the ones used in the experiments found in references [111, 124] could be used.

The production of Rydberg dressed atoms with lifetimes long enough to observe the FKM physics is also a challenging task, mainly due to unwanted off-resonant scattering. Considering the parameters of our calculations, a realistic timescale for the dressing of each atom in an experimental implementation would be limited to ~ 10 ms. However, a stronger repumping to the Rydberg dressed state could extend the survival time of the Rydberg state, as it would allow for keeping the average number of Rydberg dressed atoms constant. Another option would be to increase the detuning, but this would require more power.

The possible problems do not end here, as phenomena such as ionization by blackbody radiation and avalanche ionization can be detrimental in the possible experimental implementation. However, the blackbody radiation can be strongly suppressed by different methods, such as using cryogenic systems [125, 126]. While the very low densities required should prevent the onset of avalanche mechanisms like the one discussed in [127].

Chapter 7

Conclusions and Further Remarks

In this thesis, I presented and discussed a new apparatus that I have built and how I used it to take pioneering steps in the study of NEQT. This apparatus is able to produce Bose-Einstein condensates of ^{87}Rb and cold samples of ^{41}K and ^{39}K. Exploiting the potential of this new machine, we have achieved the dissipative distillation of supercritical quantum gases. In order to achieve this, we immersed our ^{87}Rb BEC in a cold gas of ^{39}K atoms trapped in a MOT. This effectively realized a controlled open many-body quantum system, where the ^{87}Rb BEC could be manipulated by the external environment embodied by the ^{39}K atoms. Due to a temperature difference of four orders of magnitude between the ^{87}Rb BEC and the ^{39}K MOT, the ^{39}K MOT resulted in a dissipative environment for the ^{87}Rb BEC since the collisions between both atomic species resulted in the ^{87}Rb atoms being heated up out of the BEC regime. The combination of the dissipation with the evaporative cooling, used to cool down the ^{87}Rb to the quantum degeneracy, allowed for the realization of states out of reach for usual BEC experiments operating in equilibrium. This made it possible to create supercritical BECs, meaning that the condensed fraction is higher than in the equilibrium case and that they can exist above the critical temperature. Furthermore, we demonstrated that these supercritical states are long-lived and exhibit the quasistatic behavior typical of prethermalized states. Consequently, they can be used

to perform experiments with high condensed fractions at temperatures out of range for the usual BEC. I hope that the experiments presented in this thesis will attract the interest of the theory community since a microscopic description of out-of-equilibrium quantum gases is required to completely understand the physics of this system. Moreover, the high degree of control can be a useful tool for distilling environmentally resilient states and engineering quantum phases in an open quantum system.

I have also reported on a proposal to experimentally realize the FKM using a system of Rydberg dressed atoms placed in an optical lattice as a possible experimental realization for the study of the FKM. In this system, we can change the interaction between particles by changing the Rydberg level used to dress the atoms as well as the lattice spacing. In order to prove that it is possible to realize the FKM with this system, we calculated the ground states of the system and studied their properties. We did this for two different interaction potentials, springlike and repulsive. Although in both cases we observed a pinned and an unpinned phases, characteristic of the FKM, we observed differences in the transition between them. While in the springlike case we observed a sudden transition, in the repulsive case we observed a smooth crossover. This proved not only that the FKM model can be studied with the proposed system in the springlike case but that this system can be used to study other physical systems, such as those of soft matter physics in the repulsive case. Furthermore, if other interactions are used, which only requires changing the Rydberg levels used for the dressing, it may be possible to extend it to the study of other systems. Another possibility is to study the Frenkel-Kontorova-Tomlinson model, which will require the addition of an external force to the particles, opening the possibility of studies of tribology, as the unpinned phase should theoretically allow for the observation of superlubricity.

The next step is the experimental realization of the single-atom quantum engine. For now, our experiment is able to provide the thermal bath of ultracold ^{87}Rb. Moreover, we are able to trap few atoms in the optical tweezer that we are currently optimizing to

trap reliably a single ^{41}K atom that will act as our working fluid. Once this is done, we will need to characterize the interaction between both atomic species and set a Raman side-band spectroscopy setup to measure the energy level of the ^{41}K atom. Using all these ingredients we will be able to realize the three possible quantum engines: Carnot, Otto and Diesel. This realization will allow for the direct comparison between the performance of quantum engines and their classical counterparts.

Bibliography

[1] M. H. Anderson, J. R. Ensher, M. R. Matthews, C. E. Wieman, and E. A. Cornell. Observation of bose-einstein condensation in a dilute atomic vapor. *Science*, 269(5221):198–201, Jul 1995.

[2] D. Frese, B. Ueberholz, S. Kuhr, W. Alt, D. Schrader, V. Gomer, and D. Meschede. Single atoms in an optical dipole trap: Towards a deterministic source of cold atoms. *Physical Review Letters*, 85:3777–3780, Oct 2000.

[3] H. Quan, Y. Liu, C. Sun, and F. Nori. Quantum thermodynamic cycles and quantum heat engines. *Physical Review E*, 76(3):031105, Sep 2007.

[4] H.T. Quan. Quantum thermodynamic cycles and quantum heat engines. ii. *Physical Review E*, 79(4):041129, Apr 2009.

[5] S. Vinjanampathy and J. Anders. Quantum thermodynamics. *Contemporary Physics*, 57(4):545–579, Jul 2016.

[6] R. Kosloff and A. Levy. Quantum heat engines and refrigerators: Continuous devices. *Annual Review of Physical Chemistry*, 65:365–393, 2014.

[7] R. Uzdin, A. Levy, and R. Kosloff. Equivalence of quantum heat machines, and quantum-thermodynamic signatures. *Physical Review X*, 5(3):031044, Sep 2015.

[8] L. Del Rio, J. Åberg, R. Renner, O. Dahlsten, and V. Vedral. The thermodynamic meaning of negative entropy. *Nature*, 474(7349):61–63, Jun 2011.

[9] M. O Scully, M.S. Zubairy, G.S. Agarwal, and H. Walther. Extracting work from a single heat bath via vanishing quantum coherence. *Science*, 299(5608):862–864, Feb 2003.

[10] R. Dillenschneider and E. Lutz. Energetics of quantum correlations. *Europhysics Letters*, 88(5):50003, Dec 2009.

[11] J. Roßnagel, O. Abah, F. Schmidt-Kaler, K. Singer, and E. Lutz. Nanoscale heat engine beyond the carnot limit. *Physical Review Letters*, 112(3):030602, Jan 2014.

[12] A. Del Campo, J. Goold, and M. Paternostro. More bang for your buck: Super-adiabatic quantum engines. *Scientific reports*, 4(1):1–5, Aug 2014.

[13] J. Jaramillo, M. Beau, and A. del Campo. Quantum supremacy of many-particle thermal machines. *New Journal of Physics*, 18(7):075019, Jul 2016.

[14] J. Klatzow, J.N. Becker, P.M. Ledingham, C. Weinzetl, K.T. Kaczmarek, D.J. Saunders, J. Nunn, I.A. Walmsley, R. Uzdin, and E. Poem. Experimental demonstration of quantum effects in the operation of microscopic heat engines. *Physical Review Letters*, 122(11):110601, Mar 2019.

[15] J. Brantut, C. Grenier, J. Meineke, D. Stadler, S. Krinner, C. Kollath, T. Esslinger, and A. Georges. A thermoelectric heat engine with ultracold atoms. *Science*, 342(6159):713–715, Nov 2013.

[16] J. Roßnagel, S.T. Dawkins, K.N. Tolazzi, O. Abah, E. Lutz, F. Schmidt-Kaler, and K. Singer. A single-atom heat engine. *Science*, 352(6283):325–329, Apr 2016.

[17] G. Nicolis. Dissipative systems. *Reports on Progress in Physics*, 49(8):873, 1986.

[18] L.H. Dogra, J.A.P. Glidden, T.A. Hilker, C. Eigen, E.A. Cornell, R.P. Smith, and Z. Hadzibabic. Can three-body recombination purify a quantum gas? *Physical Review Letters*, 123:020405, Jul 2019.

[19] B. Buca and D. Jaksch. Dissipation induced non-stationarity in a quantum gas. *arXiv preprint arXiv:1905.12880*, Dec 2019.

[20] N. Dogra, M. Landini, K. Kroeger, L. Hruby, T. Donner, and T. Esslinger. Dissipation-induced structural instability and chiral dynamics in a quantum gas. *Science*, 366(6472):1496–1499, Dec 2019.

[21] J.T. Barreiro, M. Müller, P. Schindler, D. Nigg, T. Monz, M. Chwalla, M. Hennrich, C.F. Roos, P. Zoller, and R. Blatt. An open-system quantum simulator with trapped ions. *Nature*, 470(7335):486, Feb 2011.

[22] K.G.H. Vollbrecht, C.A. Muschik, and J.I. Cirac. Entanglement distillation by dissipation and continuous quantum repeaters. *Physical Review Letters*, 107:120502, Sep 2011.

[23] J.I. Cirac and P. Zoller. Quantum computations with cold trapped ions. *Physical Review Letters*, 74:4091–4094, May 1995.

[24] D.A. Lidar, I.L. Chuang, and K.B. Whaley. Decoherence-free subspaces for quantum computation. *Physical Review Letters*, 81:2594–2597, Sep 1998.

[25] A. Beige, D. Braun, B. Tregenna, and P.L. Knight. Quantum computing using dissipation to remain in a decoherence-free subspace. *Physical Review Letters*, 85:1762–1765, Aug 2000.

[26] G. Barontini, L. Hohmann, F. Haas, J. Estève, and J. Reichel. Deterministic generation of multiparticle entanglement by quantum zeno dynamics. *Science*, 349(6254):1317–1321, Sep 2015.

[27] A.L. Gaunt, R.J. Fletcher, R.P. Smith, and Z. Hadzibabic. A superheated Bose-condensed gas. *Nature Physics*, 9(5):271–274, May 2013.

[28] M.H. Szymańska, J. Keeling, and P.B. Littlewood. Non-equilibrium bose–einstein condensation in a dissipative environment. In *Quantum Gases: Finite Temperature and Non-equilibrium Dynamics*, pages 447–459. World Scientific, 2013.

[29] A. Polkovnikov, K. Sengupta, A. Silva, and M. Vengalattore. Colloquium: Nonequilibrium dynamics of closed interacting quantum systems. *Reviews of Modern Physics*, 83:863–883, Aug 2011.

[30] T. Langen, R. Geiger, and J. Schmiedmayer. Ultracold atoms out of equilibrium. *Annual Review of Condensed Matter Physics*, 6(1):201–217, Mar 2015.

[31] T Kinoshita, T Wenger, and D.S. Weiss. A quantum Newton's cradle. *Nature*, 440(7086):900–903, Apr 2006.

[32] S. Hofferberth, I. Lesanovsky, B. Fischer, T. Schumm, and J. Schmiedmayer. Non-equilibrium coherence dynamics in one-dimensional Bose gases. *Nature*, 449(7160):324–327, Sep 2007.

[33] S. Trotzky, Y.A. Chen, A. Flesch, I.P. McCulloch, U. Schollwöck, J. Eisert, and I. Bloch. Probing the relaxation towards equilibrium in an isolated strongly correlated one-dimensional Bose gas. *Nature Physics*, 8(4):325–330, Apr 2012.

[34] L.E. Sadler, J.M. Higbie, S.R. Leslie, M. Vengalattore, and D.M. Stamper-Kurn. Spontaneous symmetry breaking in a quenched ferromagnetic spinor Bose–Einstein condensate. *Nature*, 443(7109), Sep.

[35] R.P. Smith, S. Beattie, S. Moulder, R.L. D. Campbell, and Z. Hadzibabic. Condensation dynamics in a quantum-quenched bose gas. *Physical Review Letters*, 109:105301, Sep 2012.

[36] M. Gring, M. Kuhnert, T. Langen, T. Kitagawa, B. Rauer, M. Schreitl, I. Mazets, D. Adu Smith, E. Demler, and J. Schmiedmayer. Relaxation and Prethermalization in an Isolated Quantum System. *Science*, 337(6100):1318–1322, Sep 2012.

[37] J. Klaers, J. Schmitt, F. Vewinger, and M. Weitz. Bose–einstein condensation of photons in an optical microcavity. *Nature*, 468(7323):545–548, Nov 2010.

[38] T. Byrnes, N.Y. Kim, and Y. Yamamoto. Exciton–polariton condensates. *Nature Physics*, 10(11):803–813, Oct 2014.

[39] O.M. Braun and Y.S. Kivshar. *The Frenkel-Kontorova model: concepts, methods, and applications*. Springer Science & Business Media, 2013.

[40] Alexei Bylinskii, Dorian Gangloff, Ian Counts, and Vladan Vuletić. Observation of aubry-type transition in finite atom chains via friction. *Nature materials*, 15(7):717–721, 2016.

[41] N. Meyer, H. Proud, M. Perea-Ortiz, C. O'Neale, M. Baumert, M. Holynski, J. Kronjäger, G. Barontini, and K. Bongs. Observation of two-dimensional localized jones-roberts solitons in bose-einstein condensates. *Physical Review Letters*, 119(15):150403, 2017.

[42] J. Mellado Muñoz, X. Wang, T. Hewitt, A. U. Kowalczyk, R. Sawant, and G. Barontini. Dissipative distillation of supercritical quantum gases. *Physical Review Letters*, 125:020403, Jul 2020.

[43] J. Muñoz Mellado, R. Sawant, A. Maffei, X. Wang, and G. Barontini. Realizing the frenkel-kontorova model with rydberg-dressed atoms. *Physical Review A*, 102:043308, Oct 2020.

[44] C. J. Pethick and H. Smith. *Bose–Einstein Condensation in Dilute Gases*. Cambridge University Press, 2nd edition, 2008.

[45] F. Dalfovo, S. Giorgini, L. P. Pitaevskii, and S. Stringari. Theory of bose-einstein condensation in trapped gases. *Review of Modern Physics*, 71:463–512, Apr 1999.

[46] N. Tammuz, R.P. Smith, R.L. Campbell, S. Beattie, S. Moulder, J. Dalibard, and Z. Hadzibabic. Can a bose gas be saturated? *Physical Review Letters*, 106(23):230401, Jun 2011.

[47] R.P. Smith, R.L. Campbell, N. Tammuz, and Z. Hadzibabic. Effects of interactions on the critical temperature of a trapped bose gas. *Physical Review Letters*, 106(25):250403, Jun 2011.

[48] F. Gerbier, J.H. Thywissen, S. Richard, M. Hugbart, P. Bouyer, and A. Aspect. Critical temperature of a trapped, weakly interacting bose gas. *Physical Review Letters*, 92(3):030405, Jan 2004.

[49] C. J. Foot et al. *Atomic physics*, volume 7. Oxford University Press, 2005.

[50] S. Chu, L. Hollberg, J.E. Bjorkholm, A. Cable, and A. Ashkin. Three-dimensional viscous confinement and cooling of atoms by resonance radiation pressure. *Physical Review Letters*, 55(1):48, Jul 1985.

[51] D.W. Sesko, T.G. Walker, and C.E. Wieman. Behavior of neutral atoms in a spontaneous force trap. *Journal of the Optical Society of America B*, 8(5):946–958, Oct.

[52] J. Dalibard and C. Cohen-Tannoudji. Laser cooling below the doppler limit by polarization gradients: simple theoretical models. *Journal of the Optical Society of America B*, 6(11):2023–2045, Jun 1989.

[53] K.B. Davis, M.-O. Mewes, M.R. Andrews, N.J. van Druten, D.S. Durfee, D.M. Kurn, and W. Ketterle. Bose-einstein condensation in a gas of sodium atoms. *Physical Review Letters*, 75(22):3969, Nov 1995.

[54] S. Stellmer, B. Pasquiou, R. Grimm, and F. Schreck. Laser cooling to quantum degeneracy. *Physical Review Letters*, 110(26):263003, June 2013.

[55] W. Ketterle, N.J. Van Druten, et al. Evaporative cooling of trapped atoms. *Advances in Atomic, Molecular, and Optical Physics*, 37(0):181, 1996.

[56] P. Bouyer, V. Boyer, S.G. Murdoch, G. Delannoy, Y. Le Coq, A. Aspect, and M. Lécrivain. Rf-induced evaporative cooling and bec in a high magnetic field. volume Bose-Einstein Condensates and Atom Lasers, pages 165–186. Springer, 2002.

[57] M.D. Barrett, J.A. Sauer, and M.S. Chapman. All-optical formation of an atomic bose-einstein condensate. *Physical Review Letters*, 87(1):010404, Jun.

[58] R. Grimm, M. Weidemüller, and Y.B. Ovchinnikov. Optical dipole traps for neutral atoms. *arXiv preprint physics/9902072*, Feb 1999.

[59] Eric.A. Cornell, J.R. Ensher, and C.E. Wieman. Experiments in dilute atomic bose-einstein condensation. *arXiv preprint cond-mat/9903109*, Mar 1999.

[60] A. Simoni, M. Zaccanti, C. D'Errico, M. Fattori, G. Roati, M. Inguscio, and G. Modugno. Near-threshold model for ultracold krb dimers from interisotope feshbach spectroscopy. *Physical Review A*, 77(5):052705, May 2008.

[61] C.W. Gardiner and P. Zoller. Quantum kinetic theory: A quantum kinetic master equation for condensation of a weakly interacting bose gas without a trapping potential. *Physical Review A*, 55(4):2902, Apr 1997.

[62] D. Jaksch, C.W. Gardiner, and P. Zoller. Quantum kinetic theory. ii. simulation of the quantum boltzmann master equation. *Phys. Rev. A*, 56:575–586, Jul 1997.

[63] C.W. Gardiner, P. Zoller, R.J. Ballagh, and M.J. Davis. Kinetics of bose-einstein condensation in a trap. *Physical Review Letters*, 79(10):1793, Sep 1997.

[64] C. W. Gardiner, M. D. Lee, R. J. Ballagh, M. J. Davis, and P. Zoller. Quantum kinetic theory of condensate growth: Comparison of experiment and theory. *Physical Review Letters*, 81:5266–5269, Dec 1998.

[65] K. Zyczkowski and I. Bengtsson. Geometry of quantum states, 2006.

[66] C. Monroe, D.M. Meekhof, B.E. King, S.R. Jefferts, W.M. Itano, D.J. Wineland, and P. Gould. Resolved-sideband raman cooling of a bound atom to the 3d zero-point energy. *Physical Review Letters*, 75:4011–4014, Nov 1995.

[67] C. Chin, R. Grimm, P. Julienne, and E. Tiesinga. Feshbach resonances in ultracold gases. *Review of Modern Physics*, 82:1225–1286, Apr 2010.

[68] G. Barontini, C. Weber, F. Rabatti, J. Catani, G. Thalhammer, M. Inguscio, and F. Minardi. Observation of heteronuclear atomic efimov resonances. *Physical Review Letters*, 103:043201, Jul 2009.

[69] G. Barontini and M. Paternostro. Ultra-cold single-atom quantum heat engines. *New Journal of Physics*, 21(6):063019, Jun 2019.

[70] A. Mosk, S. Kraft, M. Mudrich, K. Singer, W. Wohlleben, R. Grimm, and M. Weidemüller. Mixture of ultracold lithium and cesium atoms in an optical dipole trap. *Applied Physics B*, 73(8):791–799, Mar 2001.

[71] D.W. Snoke and J.P. Wolfe. Population dynamics of a bose gas near saturation. *Physical Review B*, 39(7):4030, Mar 1989.

[72] S. Popescu, A.J. Short, and A. Winter. Entanglement and the foundations of statistical mechanics. *Nature Physics*, 2(11):754–758, Oct 2006.

[73] M. Weiss and F. Elmer. Dry friction in the Frenkel-Kontorova-Tomlinson model: Static properties. *Physical Review B*, 53(11):7539, Mar 1996.

[74] M. Weiss and F. Elmer. Dry friction in the frenkel-kontorova-tomlinson model: dynamical properties. *Zeitschrift für Physik B Condensed Matter*, 104(1):55–69, 1997.

[75] E.A. Fitzgerald. Dislocations in strained-layer epitaxy: theory, experiment, and applications. *Materials science reports*, 7(3):87–142, Mar 1991.

[76] O.M. Braun and V.K. Medvedev. Interaction between particles adsorbed on metal surfaces. *Soviet Physics Uspekhi*, 32(4):328, Apr 1989.

[77] R. Blinc and A.P. Levanyuk. *Incommensurate phases in dielectrics*, volume 1. North-Holland Amsterdam, Mar 1986.

[78] W. Xiao, P.A. Greaney, and D.C. Chrzan. Adatom transport on strained cu (001): Surface crowdions. *Physical Review Letters*, 90(15):156102, Apr 2003.

[79] R. A. Cowley, J. D. Axe, and M. Iizumi. Neutron scattering from the ferroelectric fluctuations and domain walls of lead germanate. *Physical Review Letters*, 36:806–809, Apr 1976.

[80] D.W. McLaughlin and A.C. Scott. Perturbation analysis of fluxon dynamics. *Physical Review A*, 18(4):1652, Oct 1978.

[81] A. Vanossi, N. Manini, M. Urbakh, S. Zapperi, and E. Tosatti. Colloquium: Modeling friction: From nanoscale to mesoscale. *Reviews of Modern Physics*, 85(2):529, Apr 2013.

[82] D. Benedicto-Orenes, A. Kowalczyk, K. Bongs, and G. Barontini. Endoscopic imaging of quantum gases through a fiber bundle. *Optics express*, 25(17):19701–19710, 2017.

[83] T. Tiecke. Properties of potassium. *University of Amsterdam, The Netherlands*, Thesis:12–14, 2010.

[84] D.W. Preston. Doppler-free saturated absorption: Laser spectroscopy. *American Journal of Physics*, 64(11):1432–1436, Nov 1996.

[85] G. Ritt, G. Cennini, C. Geckeler, and M. Weitz. Laser frequency offset locking using a side of filter technique. *Applied Physics B*, 79(3):363–365, Aug 2004.

[86] T.M. Brzozowski, M. Maczynska, M. Zawada, J. Zachorowski, and W. Gawlik. Time-of-flight measurement of the temperature of cold atoms for short trap-probe

beam distances. *Journal of Optics B: Quantum and Semiclassical Optics*, 4(1):62, Jan 2002.

[87] A. Keshet. *Cicero Word Generator Technical and User Manual*. 2008.

[88] D. Benedicto Orenes, A.U. Kowalczyk, E. Witkowska, and G. Barontini. Exploring the thermodynamics of spin-1 bose gases with synthetic magnetization. *New Journal of Physics*, 21(4):043024, Apr 2019.

[89] K. Dieckmann, R.J.C. Spreeuw, M. Weidemüller, and J.T.M. Walraven. Two-dimensional magneto-optical trap as a source of slow atoms. *Physical Review A*, 58(5):3891, Nov 1998.

[90] W. Ketterle, K.B. Davis, M.A. Joffe, A. Martin, and D.E. Pritchard. High densities of cold atoms in a dark spontaneous-force optical trap. *Physical Review Letters*, 70:2253–2256, Apr 1993.

[91] C.G. Townsend, N.H. Edwards, K.P. Zetie, C.J. Cooper, J. Rink, and C.J. Foot. High-density trapping of cesium atoms in a dark magneto-optical trap. *Physical Review A*, 53:1702–1714, Mar 1996.

[92] V. Makhalov, K. Martiyanov, T. Barmashova, and A. Turlapov. Precision measurement of a trapping potential for an ultracold gas. *Physics Letters A*, 379(4):327–332, Nov 2015.

[93] A. Burchianti, C. D'Errico, M. Prevedelli, L. Salasnich, F. Ancilotto, M. Modugno, F. Minardi, and C. Fort. A dual-species bose-einstein condensate with attractive interspecies interactions. *Condensed Matter*, 5(1):21, Mar 2020.

[94] M. Landini, S. Roy, L. Carcagní, D. Trypogeorgos, M. Fattori, M. Inguscio, and G. Modugno. Sub-doppler laser cooling of potassium atoms. *Physical Review A*, 84(4):043432, Oct 2011.

[95] G. Salomon, L. Fouché, P. Wang, A. Aspect, P. Bouyer, and T. Bourdel. Gray-molasses cooling of 39k to a high phase-space density. *Europhysics Letters*, 104(6):63002, Jan 2014.

[96] M. Landini. *A tunable Bose-Einstein condensate for quantum interferometry*. PhD thesis, University of Trento, 2012.

[97] G. Salomon, L. Fouché, S. Lepoutre, A. Aspect, and T. Bourdel. All-optical cooling of k 39 to bose-einstein condensation. *Physical Review A*, 90(3):033405, Sep 2014.

[98] K. Huang and C.N. Yang. Quantum-mechanical many-body problem with hard-sphere interaction. *Physical Review*, 105:767–775, Feb 1957.

[99] K. Huang, C.N. Yang, and J.M. Luttinger. Imperfect bose gas with hard-sphere interaction. *Physical Review*, 105:776–784, Feb 1957.

[100] S.J.M. Kuppens, K.L. Corwin, K.W. Miller, T.E. Chupp, and C.E. Wieman. Loading an optical dipole trap. *Physical review A*, 62(1):013406, Jun 2000.

[101] N. Schlosser, G. Reymond, and P. Grangier. Collisional blockade in microscopic optical dipole traps. *Physical review letters*, 89(2):023005, Jun 2002.

[102] N.R. Hutzler, L.R. Liu, Y. Yu, and K. Ni. Eliminating light shifts for single atom trapping. *New Journal of Physics*, 19(2):023007, Feb 2017.

[103] D. Jaksch, C. Bruder, J.I. Cirac, C. W Gardiner, and P. Zoller. Cold bosonic atoms in optical lattices. *Physical Review Letters*, 81(15):3108, Oct 1998.

[104] M. Greiner, O. Mandel, T. Esslinger, T.W. Hänsch, and I. Bloch. Quantum phase transition from a superfluid to a mott insulator in a gas of ultracold atoms. *Nature*, 415(6867):39–44, Jan 2002.

[105] G. Roati, C. D'Errico, L. Fallani, M. Fattori, C. Fort, M. Zaccanti, G. Modugno, M. Modugno, and M. Inguscio. Anderson localization of a non-interacting bose–einstein condensate. *Nature*, 453(7197):895–898, Jun 2008.

[106] J. Billy, V. Josse, Z. Zuo, A. Bernard, B. Hambrecht, P. Lugan, D. Clément, L. Sanchez-Palencia, P. Bouyer, and A. Aspect. Direct observation of anderson localization of matter waves in a controlled disorder. *Nature*, 453(7197):891–894, Jun 2008.

[107] D. Greif, T. Uehlinger, G. Jotzu, L. Tarruell, and T. Esslinger. Short-range quantum magnetism of ultracold fermions in an optical lattice. *Science*, Jun 2013.

[108] M. Lu, N.Q. Burdick, S.H. Youn, and B.L. Lev. Strongly dipolar bose-einstein condensate of dysprosium. *Physical Review Letters*, 107(19):190401, Oct 2011.

[109] J.A. Blackmore, L. Caldwell, P.D. Gregory, E.M. Bridge, R. Sawant, J. Aldegunde, J. Mur-Petit, D. Jaksch, J.M. Hutson, B.E. Sauer, et al. Ultracold molecules for quantum simulation: rotational coherences in caf and rbcs. *Quantum Science and Technology*, 4(1):014010, Dec 2018.

[110] G. Pupillo, A. Micheli, M. Boninsegni, I. Lesanovsky, and P. Zoller. Strongly correlated gases of rydberg-dressed atoms: quantum and classical dynamics. *Physical Review Letters*, 104(22):223002, Jun 2010.

[111] J. Zeiher, R. Van Bijnen, P. Schauß, S. Hild, J. Choi, T. Pohl, I. Bloch, and C. Gross. Many-body interferometry of a rydberg-dressed spin lattice. *Nature Physics*, 12(12):1095–1099, Aug 2016.

[112] T. Macrì and T. Pohl. Rydberg dressing of atoms in optical lattices. *Physical Review A*, 89:011402, Jan 2014.

[113] M. Ostmann, M. Marcuzzi, J. Minář, and I. Lesanovsky. Synthetic lattices, flat bands and localization in rydberg quantum simulators. *Quantum Science and Technology*, 4(2):02LT01, Jan 2019.

[114] M. Viteau, M. G. Bason, J. Radogostowicz, N. Malossi, D. Ciampini, O. Morsch, and E. Arimondo. Rydberg excitations in bose-einstein condensates in quasi-one-

dimensional potentials and optical lattices. *Physical Review Letters*, 107:060402, Aug 2011.

[115] T.C. Li, H. Kelkar, D. Medellin, and M.G. Raizen. Real-time control of the periodicity of a standing wave: an optical accordion. *Optics Express*, 16(8):5465–5470, Apr 2008.

[116] J.L. Ville, T. Bienaimé, R. Saint-Jalm, L. Corman, M. Aidelsburger, L. Chomaz, K. Kleinlein, D. Perconte, S. Nascimbène, J. Dalibard, and J. Beugnon. Loading and compression of a single two-dimensional bose gas in an optical accordion. *Physical Review A*, 95:013632, Jan 2017.

[117] T. Macrì and T. Pohl. Rydberg dressing of atoms in optical lattices. *Physical Review A*, 89:011402, Jan 2014.

[118] N. Šibalić, J. D. Pritchard, C. S. Adams, and K. J. Weatherill. Arc: An open-source library for calculating properties of alkali rydberg atoms. *Computer Physics Communications*, 220:319–331, November 2017.

[119] C. Tsallis and D.A. Stariolo. Generalized simulated annealing. *Physica A: Statistical Mechanics and its Applications*, 233(1):395 – 406, Apr 1996.

[120] A.L. Gaunt, T.F. Schmidutz, I. Gotlibovych, R.P. Smith, and Z. Hadzibabic. Bose-einstein condensation of atoms in a uniform potential. *Physical Review Letters*, 110(20):200406, May 2013.

[121] L.M. Floría and J.J. Mazo. Dissipative dynamics of the frenkel-kontorova model. *Advances in Physics*, 45(6):505–598, Feb 1996.

[122] S. Aubry. The twist map, the extended frenkel-kontorova model and the devil's staircase. *Physica D: Nonlinear Phenomena*, 7(1-3):240–258, May 1983.

[123] S.R. Sharma, B. Bergersen, and B. Joos. Aubry transition in a finite modulated chain. *Physical Review B*, 29(11):6335, Jun 1984.

[124] J. Zeiher, J. Choi, A. Rubio-Abadal, T. Pohl, R. van Bijnen, I. Bloch, and C. Gross. Coherent many-body spin dynamics in a long-range interacting ising chain. *Physical Review X*, 7:041063, Dec 2017.

[125] R. Celistrino Teixeira, C. Hermann-Avigliano, T. L. Nguyen, T. Cantat-Moltrecht, J. M. Raimond, S. Haroche, S. Gleyzes, and M. Brune. Microwaves probe dipole blockade and van der waals forces in a cold rydberg gas. *Physical Review Letters*, 115:013001, Jun 2015.

[126] C. Hermann-Avigliano, R. Celistrino Teixeira, T. L. Nguyen, T. Cantat-Moltrecht, G. Nogues, I. Dotsenko, S. Gleyzes, J. M. Raimond, S. Haroche, and M. Brune. Long coherence times for rydberg qubits on a superconducting atom chip. *Physical Reiew. A*, 90:040502(R), Oct 2014.

[127] E. A. Goldschmidt, T. Boulier, R. C. Brown, S. B. Koller, J. T. Young, A.V. Gorshkov, S.L. Rolston, and J.V. Porto. Anomalous broadening in driven dissipative rydberg systems. *Physical Review Letters*, 116:113001, Mar 2016.

[128] J. E. Johnson and S. L. Rolston. Interactions between rydberg-dressed atoms. *Physical Review A*, 82:033412, Sep 2010.

Appendices

Appendix A

Calibration of the trapping frequencies

During the evaporation, the trap depth is reduced slowly. This changes the trapping frequencies (we indicate with ω the geometric mean of the trapping frequencies) of the dipole trap and hence the critical temperature according to $k_B T_c = 0.94\hbar\omega N^{1/3}$.

In equilibrium, the BEC fraction is $F = 1 - \tau^3 - \eta\tau^2(1-\tau^3)^{2/5}$. We use this fact to estimate the trapping frequency at each time during the evaporation by equating experimentally observed BEC fraction to this formula and numerically solving for ω. The mean trapping frequency calculated using the data of no dissipation cases is shown in figure A.1. We verified that all the data without dissipation correspond to equilibrium configurations by waiting a variable amount of time after the evaporation is finished. Data with the same evaporation ramp but different waiting times share the same value of ω.

After having estimated ω we perform a linear fit to the frequency versus evaporation time data reported in figure A.1.

We also measured the trapping frequencies in a few points along the evaporation ramp. The blue triangles in figure A.1 show the geometric mean of the trapping frequencies measured using parametric heating of the thermal Rb cloud. The measured values are

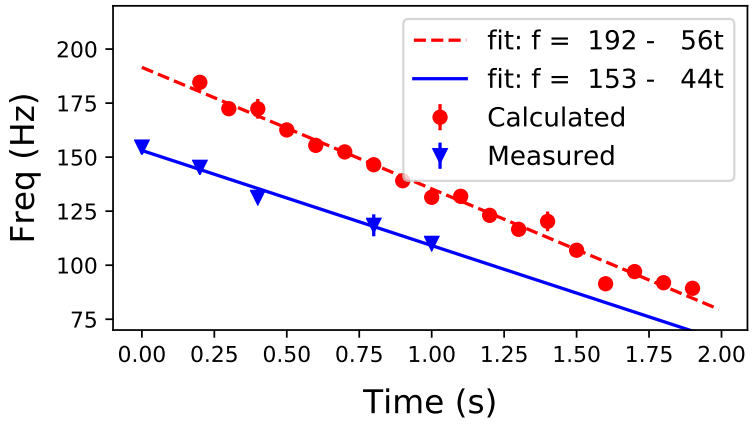


Figure A.1: The red dots are the mean trapping frequency $\omega/2\pi$ calculated using the method described in the text. The blue triangles are the mean trapping frequencies measured using parametric heating and centre of mass oscillations. The lines are linear fits to the data, the coefficients are reported in the legend.

consistent within $\sim$ 15% of the values used for calibration. This is expected as it is known that the frequency measurements using parametric heating lead to a systematic underestimation due to trap anharmonicities [92]. The calibration also accounts for effects of systematic errors in the data like, e.g., a systematic over- or under-estimation of the total number of atomss. The linear drop in frequency along the evaporation approximately matches the frequencies change we expect from the lowering of the power of the dipole trap lasers. The values we used in the calculation in chapter 4 are the measured ones, corresponding to the blue line in figure A.1.

The values for N_0 and T are obtained by fitting a combination of two-dimensional Thomas-Fermi and Gaussian distributions to the atomic density image obtained from time of flight absorption imaging. The value of N is obtained by integrating the atomic density obtained from the image.

This appendix contains a partial reproduction of my first author publication found in reference [42]. I built the experiment, took the data, collaborated in the data analysis and in the writing the manuscript of the cited publication.

Appendix B

Chemical potential calculation

To calculate the chemical potential of the thermal component μ, we used the semi-classical distribution as described in [44]:

$$N_{\text{th}} = g_3(z(0)) \left(\frac{k_B T}{\hbar \omega} \right)^3 . \tag{B.1}$$

Where T is the temperature, N_{th} is number of thermal atoms, ω is the geometric mean of the trapping frequencies and z is the fugacity defined as,

$$z(\mathbf{r}) = \mathbf{e}^{[\mu - \mathbf{V(r)}]/\mathbf{k_B T}}. \tag{B.2}$$

Combining B.1 and B.2 and considering that $V(0) = 0$ we are able to obtain μ from our experimental data.

This appendix contains a partial reproduction of my first author publication found in reference [42]. I built the experiment, took the data, collaborated in the data analysis and in the writing the manuscript of the cited publication.

Appendix C

Rydberg-dressed atoms

Rydberg-dressed atoms have the advantage of enabling the control of the range and functional dependence of the interaction potentials, using various Rydberg states for the dressing. These dressed states are achieved by weakly admixing excited Rydberg states with the ground state, using near-resonant light [111]. Here we show the theory we used in the Rydberg dressed states calculations and their corresponding interaction potentials. These interactions between Rydberg dressed atoms has been previously calculated under the assumption of a simple dipole-dipole interaction between atoms excited to the Rydberg levels, this calculation can be found in reference [128]. However, in the cited reference, they only consider a single Rydberg level. This results in an inter-atomic potential which scales as $1/R^3$ of resonant dipole-dipole interaction, where R is the inter-atomic distance. The problem of this is that it is not realistic, as in reality the Rydberg levels are so close spaced that we have to take into account the levels close to the targeted one. In our case we calculate the interaction potential taking this into account. Our starting point is the Hamiltonian for a system consisting of two atoms which interact with a light field nearly resonant with a Rydberg level,

$$
\begin{aligned}
H(t) =& \hbar \Bigg[\sum_i \omega_i (|g, r_i\rangle \langle g, r_i| + |r_i, g\rangle \langle r_i, g|) + \sum_{i,j} (\omega_i + \omega_j)(|r_j, r_i\rangle \langle r_j, r_i| + |r_i, r_j\rangle \langle r_i, r_j|) \\
&+ \sum_i 2\Omega_i e^{-i\omega_{\mathrm{L}} t}(|g, g\rangle \langle g, r_i| + |g, g\rangle \langle r_i, g|) + 2\Omega_i^* e^{i\omega_{\mathrm{L}} t}(|g, r_i\rangle \langle g, g| + |r_i, g\rangle \langle g, g|) \\
&+ \sum_{i,j} 2\Omega_i e^{-i\omega_{\mathrm{L}} t}(|g, r_j\rangle \langle r_i, r_j| + |r_j, g\rangle \langle r_j, r_i|) + 2\Omega_i^* e^{i\omega_{\mathrm{L}} t}(|r_i, r_j\rangle \langle g, r_i| + |r_j, r_i\rangle \langle r_i, g|) \\
&+ \sum_{i,j,k,l} D_{ijkl}(R) |r_i, r_j\rangle \langle r_k, r_l| + D_{ijkl}^*(R) |r_k, r_l\rangle \langle r_i, r_j| \Bigg].
\end{aligned}
\tag{C.1}
$$

Here the state, $|g, r_i\rangle$ denotes that the first atom is its ground state ($|g\rangle$) and the second atom is in the i^{th} Rydberg state ($|r_i\rangle$). $\hbar\omega_i$ is the energy of the i^{th} Rydberg state with respect to the ground state, $\omega_L/(2\pi)$ is the frequency of the dressing laser, $\Omega_i/(2\pi)$ is the Rabi frequency induced by the dressing laser for the transition $|g\rangle \rightarrow |r_i\rangle$, and $D_{ijkl}(R)$ is the interaction between Rydberg level pairs (r_i, r_j) and (r_k, r_l) as a function of interatomic distance R.

For convenience we use the following unitary transformation to change to the rotating frame,

$$
\begin{aligned}
U(t) = |g, g\rangle \langle g, g| &+ \sum_i e^{-i\omega_{\mathrm{L}} t}(|g, r_i\rangle \langle g, r_i| + |r_i, g\rangle \langle r_i, g|) \\
&+ \sum_{ij} e^{-2i\omega_{\mathrm{L}} t}(|r_i, r_j\rangle \langle r_i, r_j| + |r_j, r_i\rangle \langle r_j, r_i|).
\end{aligned}
\tag{C.2}
$$

The Hamiltonian in the rotating frame is given by,

$$
H_r = U(t) H(t) U^\dagger(t) + i\hbar U(t)\, dU^\dagger(t)/dt, \tag{C.3}
$$

and using it together with equation C.2 yields,

$$
\begin{aligned}
H_r =& \hbar \Bigg[\sum_i \Delta_i (|g, r_i\rangle \langle g, r_i| + |r_i, g\rangle \langle r_i, g|) + \sum_{i,j} (\Delta_i + \Delta_j)(|r_j, r_i\rangle \langle r_j, r_i| + |r_i, r_j\rangle \langle r_i, r_j|) \\
&+ \sum_i 2\Omega_i (|g, g\rangle \langle g, r_i| + |g, g\rangle \langle r_i, g|) + 2\Omega_i^* (|g, r_i\rangle \langle g, g| + |r_i, g\rangle \langle g, g|) \\
&+ \sum_{i,j} 2\Omega_i (|g, r_j\rangle \langle r_i, r_j| + |r_j, g\rangle \langle r_j, r_i|) + 2\Omega_i^* (|r_i, r_j\rangle \langle g, r_i| + |r_j, r_i\rangle \langle r_i, g|) \\
&+ \sum_{i,j,k,l} D_{ijkl}(R) |r_i, r_j\rangle \langle r_k, r_l| + D_{ijkl}^*(R) |r_k, r_l\rangle \langle r_i, r_j| \Bigg],
\end{aligned}
\tag{C.4}
$$

where $\Delta_i = \omega_i - \omega_{\mathrm{L}}$ is the detuning of the laser used for the dressing respect to the transition between $|g\rangle$ and $|r_i\rangle$. We define r_{t} as the target Rydberg that we want couple the laser light to. In order to do this we choose a laser which wavelength is large detuned respect to the transition, so that $\Delta_i >> \Delta_t$ for all $i \neq t$. Due to the large detuning we can neglect all levels $|g, r_{i\neq t}\rangle$ and $|r_{i\neq t}, g\rangle$. We only need to keep the levels $|r_i, r_j\rangle$ as $D_{ijkl}(R)$ is of the same order of magnitude as Δ_t. This will provide us with the R dependence. Considering these approximations, the Hamiltonian reduces to,

$$
\begin{aligned}
H_r =& \hbar \Bigg[\Delta_t (|g, r_t\rangle \langle g, r_t| + |r_t, g\rangle \langle r_t, g|) + \sum_{i,j} (\Delta_i + \Delta_j)(|r_j, r_i\rangle \langle r_j, r_i| + |r_i, r_j\rangle \langle r_i, r_j|) \\
&+ 2\Omega_i (|g, g\rangle \langle g, r_t| + |g, g\rangle \langle r_t, g|) + 2\Omega_i^* (|g, r_t\rangle \langle g, g| + |r_t, g\rangle \langle g, g|) \\
&+ \sum_i 2\Omega_i (|g, r_t\rangle \langle r_i, r_t| + |r_t, g\rangle \langle r_t, r_i|) + 2\Omega_i^* (|r_i, r_t\rangle \langle g, r_t| + |r_t, r_i\rangle \langle r_t, g|) \\
&+ \sum_{i,j,k,l} D_{ijkl}(R) |r_i, r_j\rangle \langle r_k, r_l| + D_{ijkl}^*(R) |r_k, r_l\rangle \langle r_i, r_j| \Bigg].
\end{aligned}
\tag{C.5}
$$

This appendix contains a partial reproduction of my first author publication found

in reference [43]. I made the simulations, collaborated in the data analysis and wrote the manuscript of the cited publication.